Structural characteristics of fat-associated lymphoid tissues and their role in the peritoneal propagation of B-cell lymphoma

Xinkai Jia

PhD student; research assistant

Supervisor: **Dr. Péter Balogh**

University of Pécs, Medical School

Department of Immunology and Biotechnology
Doctoral School of Basic Medical Sciences

Pécs, 2022

Contents

List of abbreviations

ABCs - age-associated B cells

BAFF - B-cell activating factor

Bc.DLFL1 - spontaneous mouse high-grade B cell lymphoma

BCMA - B-cell maturation antigen

BSA - bovine serum albumin

CCL - chemokine CC motif Ligand

CD - cluster of differentiation

cDNA - complementary deoxyribonucleic acid

CFSE - carboxyfluorescein succinimidyl ester

CTFR - CellTrace Far Red

CXCL - chemokine (C-X-C motif) ligand

DCs - dendritic cells

FALCs - fat-associated lymphoid clusters

FDCs - follicular dendritic cells

FITC - fluorescein isothiocyanate

FLAg - foliate lymphoid aggregates

FRC - fibroblastic reticular cells

FSC - forward scatter

GFP - green fluorescent protein

HEV - high endothelial venule

ICAM - intercellular adhesion molecule-1

IGFBP-1 - insulin-like growth factor binding protein-1

IgVh - immunoglobulin heavy chain variable region

ILC2 - innate lymphoid cells Type 2

LYVE-1 - lymphatic vessel endothelial hyaluronan receptor 1

MACS - magnetic cell sorting

MHC - major histocompatibility complex

mLNs - mesenteric lymph nodes

MMP - matrix metalloproteinase

MSs - milky spots

NIR - near-infrared

PBS - phosphate buffered saline

PCR - polymerase chain reaction

PDGF - platelet-derived growth factor

PFA - paraformaldehyde

PNAd - peripheral lymph node addressin

RNA - ribonucleic acid

RPMI - Roswell Park Memorial Institute

SEM - standard error of mean

sn - supernatant

SSC - side scatter

TACI - transmembrane activator and CAML interactor

Introduction

Following the entry of pathogens through skin or mucosal surfaces as first line of defense, during their propagation the pathogens are transported by various immune cells to the nearby secondary lymphoid organs, such as lymph nodes or Peyer's patches (1). Here, the lymphoid architecture allows for the efficient communication and cooperation between various leukocytes, despite their compartmentalization into different domains, including follicles (B-cell zones) and neighboring T-cell dominated regions. The recognition of antigens elicits different types of immune reactions, often resulting in the transformation of resting follicles into secondary follicles harboring germinal centers (2).

Generally, secondary lymphoid organs, such as spleen, lymph nodes and programmed intestinal lymphoid tissues, including Peyer's patches and mesenteric lymph nodes, start to develop before birth (3); however, there is another branch of the lymphoid structure that plays role in the local immunological challenges under the mucosa, such as cryptopatches (CPs) and isolated lymphoid follicles (ILFs). Their development is initiated after birth (4), allowing the expanded immunological surveillance of the mucosal surface of the intestines, continuously exposed to alimentary and microbial antigens. In contrast to these well-studied lymphoid tissues, the role of serosa in the immune system has not been fully investigated. Although substantially lesser surface compared to the mucosal area, the serosa nevertheless represents a considerably large surface shared by various abdominal organs, often in a close arrangement with adipose tissue, and harboring a unique immunological compartment including a large number of B-1 B cells (5).

Adipose tissue is usually considered as a vital energy storage. However, recent studies have unveiled the immunological potentials of adipose-associated lymphoid structures, which play essential roles in the local immune response (6–8), where they typically appear in diffuse forms and are embedded into the adipose components (9). Adipose tissue contains various lymphoid territories which participate in the local immunological challenge (6, 7). Visceral fat contains numerous leukocytes, which form adipose-associated lymphoid organoids. Here the focal accumulation of leukocytes is promoted by chemokines CXCL1 and CXCL13 (8).

Typically they appear in diffuse forms and are embedded into the adipose (9). As prototypic adipose tissue containing lymphoid congregates, the omentum has been considered the main guardian in the abdominal cavity for a long time (10). The milky spots (MSs) on the surface of the omentum contain various leukocytes with an extensive capillary meshwork (11–13), where B-1 cells are the major source of natural antibodies (14). Even though there is no evidence of germinal centers or follicular dendritic cells (FDCs), T-dependent humoral immune responses can also occur in the MSs (15, 16). More recently, fat-associated lymphoid clusters (FALCs) were discovered in the mesenteric fat and at other visceral locations (17–19). They contain B cells, T cells, macrophages, and other innate lymphoid cells including ILC2, which promote B-1 cell proliferation (17, 18). (Fig. 1).

B cells are essential elements of adaptive immunity in the body. Eventually, they will secret antibodies and differentiate into plasma cells or long-lived memory B cells (20–23). Besides that, B cells are also able to regulate immune functions through cytokine production (24, 25). Following extensive research on their developmental and differentiation characteristics, B cells are now divided into several subsets according to the cell surface markers, transcription factor specifications and immunological functions. B-1 lymphocytes promote innate-like immune response typically with natural antibodies production, and B-2 cells with regulatory activities or antigen presentation, in addition to antigen recognition (26, 27). During these processes, various activation status-related and position-related (resting or activated; in follicles mantle zone or germinal center-located, or within germinal center, light zone or dark zone located, respectively) subsets can be distinguished. As two main products, either memory B cells or plasma cells may form. Importantly, the various lymphoid tissue locations confer distinct microenvironmental cues for B-cell subset survival and commitment, thus affecting the differentiation and specialization, including Ig isotype switch, short-term or long-term plasmablast differentiation.

In addition to the exposure to antigens, aging also influences humoral immune reactions, including the capacity to mount memory responses and B-cell composition. For instance, age-associated alterations lead to diminished T-dependent recall responses, and the appearance

of age-associated B cells (ABCs) and their expansion (26–30). More recent studies on mouse ABC subset have demonstrated that they are antigen-experienced/memory type B cells without expressing mature B cell marker CD21 or CD23. However, they display CD11b and CD11c together with the production of T -bet transcription factor (30). ABCs play a crucial role in autoantibody secretion in SLE-prone mice (31). In contrast to the bulk of naïve B cells, CD11c positive/ T-bet[high] ABCs can be found in the border area between the T/B compartment in the wild-type mice spleen (32, 33). Therefore, the complexity of B cells – beyond their B-1/B-2 lineage affiliation, activation status and differentiation preference for memory or plasma cells – also includes their age-associated homeostatic shift. Importantly, these stage-specific differences are also reflected in the diverse spectrum of B-cell malignancies of different phenotypic variants, genotypic characteristics and clinical courses (32, 33). Therefore studying the various differentiation stages of B cells following their antigen exposure, including their surface characteristics and in vivo distribution, may assist in a more thorough understanding of B-cell malignancies.

In addition to various leukocyte congregates, several cancers, including colonic gastric and ovarian tumors, can also be found accumulating in the omental MSs and mesenteric fat after intraperitoneal injection of the cancer cells or during metastasis (34–36). Furthermore, in vitro culture of ovary cancer can be promoted by omental adipose-derived mesenchymal stem cells, which further confirming that support for these tumors may originate from the local serosal stroma elements (37). Additionally, neutrophil extracellular traps were also found in the premetastatic stage of ovarian cancer patients in FALC regions, thus indicating a complex interplay between serosal stroma, leukocytes during the local expansion of tumor cells. The NET formation is a result of soluble products such as IL-8, MCP-1,GROα, GROβ and G-CSF from cancer cells which can be blocked by antibody treatment against the Ly6G antigen on leukocytes (38). Moreover, EL4 T-cell lymphoma and A20 follicular diffuse large B-cell lymphoma can both bind to MSs and FALCs, (15) resulting in poor prognosis (39, 40).

In our previous work, we found a spontaneous mouse high-grade B cell lymphoma (Bc.DLFL1) with restricted in vivo propagation in mesenteric lymph nodes and spleen. In my

study, I continued the investigation of the possible binding sites for Bc.DLFL1 and normal B cells on the serosal surface and cytokine profile alteration of the visceral adipose upon the stress of lymphoma bearing. In addition, I also studied the origin of Bc.DLFL1 cells. In my thesis, I summarize our findings, and offer further possible studies for a better understanding of the serosal lymphocyte homeostasis and its implications in cancer metastasis.
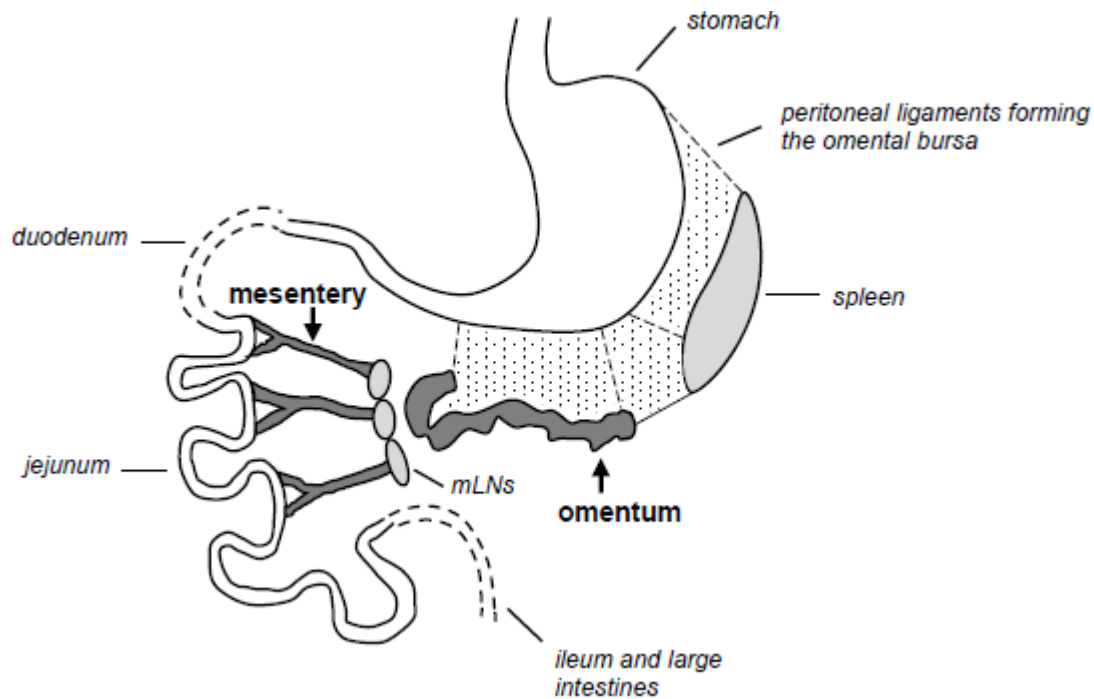
Figure 1.Schematic diagram of the location of abdominal adipose tissues containing lymphoid organoids in the mouse.
The mesentery and its branchings also harbor mesenteric vessels and lymphatic capillaries (not depicted), latter draining towards the mesenteric lymph nodes (mLNs).

Aims

Our goals are:

- To investigate the adipose-associated lymphoid structures and development;

- To study Bc.DLFL1 and normal B cells homing process in the peritoneal cavity;

- To investigate Bc.DLFL1 cell characteristics and define its origin;

- To study the microenvironment of fat-associated lymphoid structures following infiltration of Bc.DLFL1 lymphoma.

Materials and Methods

Mice

8-10 weeks old BALB/c mice and BALB/c^{eGFP} Tg mice (41) were maintained at the specific pathogen-free animal facility of the Department of Immunology and Biotechnology. Prox1-GFP BAC lymphatic reporter–transgenic mice (42) were kindly provided by Zoltán Jakus (Semmelweis University, Budapest) and were used for breeding (Prox1-GFP C57BL/6J crossed with BALB/c) F1 mice as recipients for short-term homing. KikGR mice (43) on C57BL/6J background were obtained from The Jackson Laboratory and were backcrossed through 10 generations onto BALB/c background. The Bc.DLFL1 lymphoma cells were propagated by serial intraperitoneal passages of suspension prepared from lymphoma-infiltrated mesenteric lymph nodes (mLNs) as described earlier (44). All procedures involving live animals were carried out in accordance with the guidelines set out by the Ethics Committee on Animal Experimentation (University of Pécs, Hungary) under license number BA02/2000-16/2015, with approval for the use of genetically modified organisms under license number SF/27-1/2014 issued by the Ministry of Rural Development, Hungary.

Abs and reagents

Monoclonal antibodies and other immunoreagents used in this work are listed in Table I.

Abs and reagents	Vendors
CD3 (KT-3) purified Ig A647 or FITC conjugate, CD5 (YTS121.5) sn, CD19 (1D3) sn, MHC classII (IBL-5/22) sn/ purified Ig FITC conjugate, CD21 (7G6) sn, CD23 (B3B4) sn, LFA-1/CD11a/CD18 (M17.7 and IBL-6/2) sn, MAC-1CD11b/CD18 (M1/70) sn, CD45 (IBL-3/16) sn, B220/CD45R (RA3-6B2) sn / purified Ig A647 or FITC conjugate, IgM(B7.6) sn, Thy-1/CD90 (IBL-1) sn , ICAM-1/CD54 (YN1/1) sn, VCAM-1/CD106 (M/K-2.7) sn , L-selectin/CD62L (MEL-14) sn	Self-supplied
Rat anti mouse CD138 (281-2), Rat PE- anti-mouse CXCR5 (2G8), Rat PE-anti-mouse CCR7 (4B12), Rat PE-anti-mouse CXCR-4 (2B11), Streptavidin-PE, Streptavidin–PE/Cy5	BD Biosciences (Diagon, Budapest)

Biotinylated anti-CCR7 mAb (4B12), PE-anti-BAFF-receptor (7H22-E16), PE-anti-TACI (8F10), PE- anti-mouse gp38/podoplanin mAb (8.1.1.), rat anti-mouse Ki-67 (11F6)	BioLegend (Biomedica Hungaria, Budapest)
Rat anti-LYVE-1 (223322) Ag, goat polyclonal anti-mouse CCL21, goat polyclonal anti-mouse and CXCL13, PE-anti-mouse-mouse CXCR7(73411), FITC anti-BCMA mAb (161616)	BioTechne (R&D Systems, Diagon, Budapest)
FITC-conjugated donkey anti-goat Abs and HRP-conjugated sheep anti-FITC Abs	SouthernBiotech (Bio-Kasztel, Budapest)
ImmPRESS goat anti-rat IgG-HRP polymeric conjugate	Vector Laboratories, BioMarker, Gödöllő
Rabbit anti-Fn and tetramethylrhodamine-labeled goat anti-rabbit polyclonal Abs	Abcam (Bio-Kasztel, Budapest)
Biotinylated hamster anti-mouse CD11c (N418)	eBioscience (ThermoFisher Scientific, Budapest
Chemicals for buffers and histochemical substrates	Sigma-Aldrich

Flow cytometry and sorting

Bc.DLFL1 cells and A20 cells were incubated with fluorochrome-labeled antibodies on ice for 30 minutes, then fixed in 1% PBS-buffered formaldehyde. For intracellular staining samples were first labeled for cell surface markers, followed by fixation in 1% PFA in PBS, followed by washing in PBS containing 0.1% saponin and 1% BSA, and then incubated with mAbs against T-bet and Blimp-1 at room temperature. The samples were analyzed using BD FACSCalibur and the CellQuest Pro software, collecting at least 10000 events gated on forward scatter/side scatter characteristics and B220 expression or KikGR expression combined with CD45 expression.

For IgV$_H$ sequencing Bc.DLFL1 lymphoma cells were purified by Bio-Rad S3e sorter and ProSort software v1.6 using FSC/SSC area/width gating combined with B220 labeling of lymphoblasts, followed by mRNA isolation from 10^5 lymphoma cells

Bc.DLFL1 Ig V$_H$ sequence analysis

Total mRNA from sorted Bc.DLFL1 cells was isolated using NucleoSpin RNA XS kit (Macherey-Nagel, Izinta Biotech, Budapest Hungary cDNA synthesis was performed using

High-Capacity cDNA Reverse Transcription Kit (Thermo Fisher Scientific). Endpoint PCR was carried out on Applied Biosystems 2720 Thermal Cycler using DreamTaq^{TM} Green PCR Master Mix (Thermo Scientific) with described primers (45). The PCR products were sequenced by a BigDye Terminator Cycle Sequencing Ready Reaction kit v1.1 on an AB 3500 Genetic Analyzer (Applied Biosystems, Forster City, USA) and the results were analyzed by the IMGT/HighV-QUEST platform (46).

Whole-mount and tissue section immunohistology and immunofluorescence

For whole-mount immunohistology, the entire gut complex was fixed in 4% buffered paraformaldehyde. After a short hematoxylin staining the desired regions were isolated under stereomicroscopic dissection. For immunohistochemistry, the tissue samples were incubated in 2 mg/ml phenylhydrazine hydrochloride in PBS containing 0.1% saponin and were blocked with a 1:1 mixture of 20% normal goat serum and 5% BSA for 1 h, followed by the addition of rat mAbs in the presence of 5% DMSO. The samples were incubated with various mAbs overnight, followed by extensive washing in PBS containing 0.1% saponin and 0.1% BSA. Confocal fluorescence images were taken using an Olympus FluoView FV1000 laser scanning confocal imaging system (Olympus Europa SE & Co., Hamburg, Germany). For immunohistochemistry after adding HRP-conjugated goat anti-rat Ig and development with H_2O_2-DAB, the mounted sections were viewed under an Olympus BX61 microscope. The acquisition of digital pictures with a charge-coupled device camera was performed using the ZEN software; the pictures were processed using Adobe Photoshop 6.0 with adjustments for brightness contrast and color balance applied for the entire images.

For immunohistochemistry of mLN of Bc.DLFL1 bearing mice, frozen sections at 8μm thickness prepared with a Leica CM1850 cryostat were fixed in cold acetone. For immunohistochemistry with anti-B220 and anti-Ki-67 rat mAbs, the sections were incubated in 1 mg/ml phenyl-hydrazine in PBS for 20 minutes, followed by washing in PBS. Next, the sections were saturated with 5% BSA for 20 minutes, followed by the addition of primary

antibodies, and were incubated for 45 minutes at room temperature in a humid chamber. After washing the sections were incubated with HRP-conjugated anti-rat IgG and developed using diaminobenzidine/H_2O_2 and counterstained with Mayer's hematoxylin. Dual immunofluorescence for B220 and CD11c was performed by incubating acetone-fixed and BSA-blocked cryostat sections using a cocktail of FITC anti-B220 and biotinylated anti-CD11c, followed by extensive washing and visualization of biotinylated mAb with PE-streptavidin conjugate.

For combined immunofluorescence of GFP and gp38/podoplanin, the mesentery from lymphoma-injected BALB/c^{eGFP} recipients was fixed in 4% PBS-buffered paraformaldehyde for two hours, followed by 30% sucrose equilibration overnight. Following embedding in Killik cryoprotective compound, the samples were frozen and 20 µm thick cryostat sections were cut, and placed on silan-coated microscopy slides. Following drying, the sections were rehydrated and blocked in 5% BSA for 20 minutes, followed by incubation with PE-conjugated anti-gp38 mAb in PBS. After washing the sections were mounted with 50% PBS-glycerol containing Hoechst-33342 nuclear counterstain. Confocal fluorescence images were taken using an Olympus Fluoview FV-1000 laser scanning confocal imaging system (Olympus Europa SE & Co. KG, Hamburg, Germany).

Transmission electron microscopy

Dissected mouse intestines and harvested FLAgs were fixed overnight at 4°C with 4% buffered paraformaldehyde, washed in PBS, and postfixed with 2% glutaraldehyde, followed by dehydration in graded ethanol. Tissue samples were treated with 1% osmium tetroxide (Polysciences, Warrington, PA) for 2 h and embedded in a Polybed/Araldite 6500 mixture (Polysciences). The 1µm-thick semithin sections were stained with toluidine blue. The ultrathin sections were contrasted with uranyl acetate and lead citrate and studied with a Hitachi Electron microscope type H-7600.

Cell labeling and transfer

A20 cells and Bc.DLFL1 cells (44) were either labeled with 5 mM CFSE (Thermo Fisher Scientific, Life Technologies, Budapest, Hungary), or with 10 mM CellTrace Far Red (CTFR) (47). Normal peritoneal B cells were purified from BALB/c mice using FITC-labeled anti-B220 and anti-FITC beads, followed by separation on VarioMACS (Miltenyi Biotec). For near-infrared (NIR) fluorescence bioimaging of MACS-purified B cells or lymphoma cells, we used lipophilic XenoLight DiR dye (PerkinElmer) as recommended by the vendor. After labeling, the cells were washed in RPMI 1640 basal medium and were injected i.p. at 2×10^6 cells per recipient dosage.

NIR fluorescence imaging

MACS-purified B cells or lymphoma cells (A20 or Bc.DLFL1) were labeled with XenoLight DiR dye, followed by i.p. injection. The fluorescence in the excised gut samples was measured using the IVIS Lumina III (PerkinElmer, Waltham MA) in vivo imaging system. The tissue binding of Bc.DLFL1 lymphoma cells was quantified by NIR analysis of microdissected serous lymphoid organoids placed in Greiner Bio-One CELLSTAR plate after the hematoxylin staining of 4% paraformaldehyde–fixed omentum and mesentery of mice previously injected i.p. with XenoLight DiR–labeled lymphoma cells. The data were processed and analyzed using Living Image software (PerkinElmer) by displaying the fluorescence intensity using the total radiant efficiency ([photons per second per square centimeter per steradian]/ [microwatt per square centimeter]) as a pseudocolor overlay image.

KikGR photoconversion and competitive homing

KikGR lymph nodes were photoconverted by exposure to a custom-made illumination device (Optics Engineering, Budapest, Hungary) through 6mm-diameter fiber optics using indium gallium nitride– based 410-nm chip light-emitting diode (no. APGC1 410, 125 mW) for

14

2 × 5 min from two sides at room temperature. After the mechanical release of lymphocytes, photoconverted red KikR cells were placed on ice, whereas lymphocytes from unconverted green (KikG) lymph nodes were incubated with 10 µg/ml anti–L-selectin/CD62L mAb MEL-14 (48). After incubation, the lymphocytes were washed and resuspended at 1:1 KikG/KikR ratio (with the final donor cell mixture verified by flow cytometry) and were injected in the tail vein in BALB/c recipients at 5 × 10^7 total cells per recipient in 250µl volume. The degree of inhibition was determined by the KikG/KiR ratio following anti-CD45 labeling, corrected with the KikG/KikR ratio of donor cell mixture.

BAFF-receptor blockade in lymphoma-bearing mice

BALB/c mice (*n*=10) received 5x10^6 Bc.DLFL1 cells intraperitoneally, followed by intravenous treatment of 100 µg mBR3-Fc fusion protein (generously supplied by Genentech) three times a week, for a total of four injections. Control mice (*n*=10) received a similar dose of mouse IgG1 isotype anti-fluorescein mAb F4/1 (49). The experiment was terminated on the 18th day after the lymphoma inoculation, followed by autopsy and macroscopic inspection of the mice. The effect of BAFF-receptor blockade on the composition of peripheral lymph nodes was assessed by the flow cytometric analysis of axillary lymph nodes for T:B cell ratio using FITC-conjugated anti-CD3 and Alexa Fluor 647-labeled anti-B220 mAbs.

In vitro culture of Bc.DLFL1 cells and lentiviral transduction with ZsGreen1 fluoroprotein

Bc.DLFL1 cells were seeded onto 6-well plates (Greiner Bio-One Hungary Kft, Mosonmagyarovar, Hungary) containing adherent peritoneal exudate cells obtained by the peritoneal lavage of BALB/c mice with RPMI-1640 and 10% FBS containing 2 mM GlutaMAX (ThermoFisher Scientific, Budapest, Hungary) and 5x10^{-5} M β-mercaptoethanol.

VSV-G-pseudotyped lentiviral vectors encoding ZsGreen1 green fluorescent protein driven by EF1α promoter (Vectalys, Genomix Explorea, Budapest) at 20 MOI were incubated

with the lymphoma cells overnight. After incubation, the lymphoma cells were washed and cultured in RPMI-1640 supplemented as above. Following the visual detection of green fluorescence using ZOE fluorescent cell imager (Bio-Rad) in the lymphoma colonies, the lymphoma cells were collected and following staining with anti-B220 AlexaFluor 647 mAb conjugate, the lymphoma cells with the highest 10% expression of green fluorescence (Bc.DLFL1^{ZsGreen1}) were sorted using Bio-Rad S3e sorter and subsequently propagated in vitro.

Homing of blood-borne Bc.DLFL1^{ZsGreen1} lymphoma cells

Bc.DLFL1^{ZsGreen1} cells were injected intravenously at 2×10^6 cells/recipient dose i.v. 12 hours later the spleens from the recipients were processed for immunofluorescence detection using Alexa Fluor 647-labeled anti-B220 and anti-MARCO (#IBL-12, (50)) antibodies on cryostat sections at 8µm thickness from 4% paraformaldehyde-fixed tissues after overnight equilibration in 20% sucrose. After mounting the sections were viewed under an Olympus Fluoview FV-1000 laser scanning confocal microscope; the pictures were edited using Adobe Photoshop 6.0 with corrections for brightness-contrast and color balance applied for the entire images.

R&D cytokine array of lymphoma tissue extract and quantification

Omentum, jejunal mesentery and mLNs were collected either from the end-stage lymphoma bearing mice or from untreated BALB/c mice. Tissues were lysed with T-PER^{tm} Tissue Protein Extraction Reagent (Thermo Scientific) mixed with protease inhibitor cocktail (Sigma Aldrich Ltd, Budapest, Hungary) according to the manufacturer's protocol, and dissociated mechanically by Potter homogenizer at room temperature. The lysate was applied onto the membranes in Proteome profiler^{TM} Array Mouse XL Cytokine Array Kit (R&D Systems) and processed according to the manufacturer's protocol. The membranes were

imaged by using LAS 4000 image reader and software using chemoluminescence measurements at 180 sec exposure time and analysis using ImageJ (NIH). Each relative density parameters (X_{lymph} or X_{ctr}) were corrected by subtracting the negative reference values (N_{lymph} or N_{ctr}), and the ratio to the positive reference values (Ref_{lymph} or Ref_{ctr}) was calculated according to the calculation below:

$$X = \frac{Xlymph - Nlymph}{Reflymph - Nlymph} : \frac{Xctr - Nctr}{Refctr - Nctr}$$

Heatmap was created with the pheatmap (51) package within R (52). Raw data were normalized to *z* scores. Complete clustering method with Euclidean distance was applied to the normalized data set, which was visualized with the pheatmap function from pheatmap package.

Quantitative RT-PCR

Total mRNA from inguinal lymph node, omentum, and mesentery homogenates was isolated using NucleoSpin RNA (Macherey-Nagel). Purity and concentration of RNA was analyzed by NanoDrop. cDNA was synthetized using High-Capacity cDNA Reverse Transcription Kit (Life Technologies). RT-PCR was run on an Applied Biosystems PRISM 7500 machine in duplicates using previously described SYBR Green primers for PNAd core proteins and glycosylation enzymes, creating the MECA-79 epitope (53). Results are shown as fold change of target gene relative to the β-actin housekeeping gene mRNA level, defining the relative value of pLN as 1.

Statistical analysis

Data analysis was performed using SPSS 22.0 (IBM). Normality of data distribution was assessed by Shapiro–Wilks test. A *t*-test or Mann–Whitney U test was employed to

compare two groups with normally distributed and non-normally distributed data, respectively. Data are represented as mean ± SEM. A *p* value < 0.05 was considered statistically significant. Statistical analysis of BAFF-R treatment effect on T/B distribution was performed by student's T-test using GraphPad Prism 5, where significance was considered with p value <0.001. Error bar represents SEM. Kaplan-Meier survival curve was generated by using GraphPad Prism 5 (p<0.01).

Results

FLAgs as novel forms of serosal lymphoid organoids connected to the mesenteric lymphoid drainage

The high-grade B-cell lymphoma cells Bc.DLFL1 preferentially colonize the mesenteric lymph nodes; however, the entry route was uncharted, prompting its analysis.

As we earlier observed, this lymphoma following its intraperitoneal injection in BALB/c mice displays restricted expansion in mesenteric lymph nodes and spleen (44). However, the early homing process of this lymphoma has not been clarified. Therefore, we i.p injected 10^5 the same number of tumor cells which were labeled by XenoLight DiR dye, and followed their adherence by NIR fluorescence detection at 4-hour post administration. The image from injected mice suggested three compartments of positive regions, corresponding to the mesenteric lymph nodes, spleen and the injection site, respectively. However, after exploring the abdominal cavity we found that the majority of the fluorescence signal is emitted from the omentum, together with a series of small foci along the edge of the mesenteric fat, whereas the mesenteric lymph nodes and spleen were free of fluorescence signal [Fig. 2A-F]. Quantitative analysis of fluorescent signal emission from the omentum and mesenteric fat indicates that there is no significant difference between two sets of signals, even though the intensity of individual foci on the mesenteric fat is relatively weak [Fig. 2I]. We also performed a similar experiment with CFSE-labeled lymphoma cells followed by anti-FITC whole-mount immunohistochemistry. We observed the distribution of CFSE-labeled lymphoma was comparable with NIR imaging [Fig. 2G-H].

Next, we studied if the normal B cells also home selectively upon i.p administration. Purified B cells labeled with XenoLight DiR dye displayed a similar pattern as Bc.DLFL1 cells 4 hours after the injection [Fig. 3A]. The total radiation from the foci of the mesenteric fat is significantly higher than from the omentum [Fig. 3B].
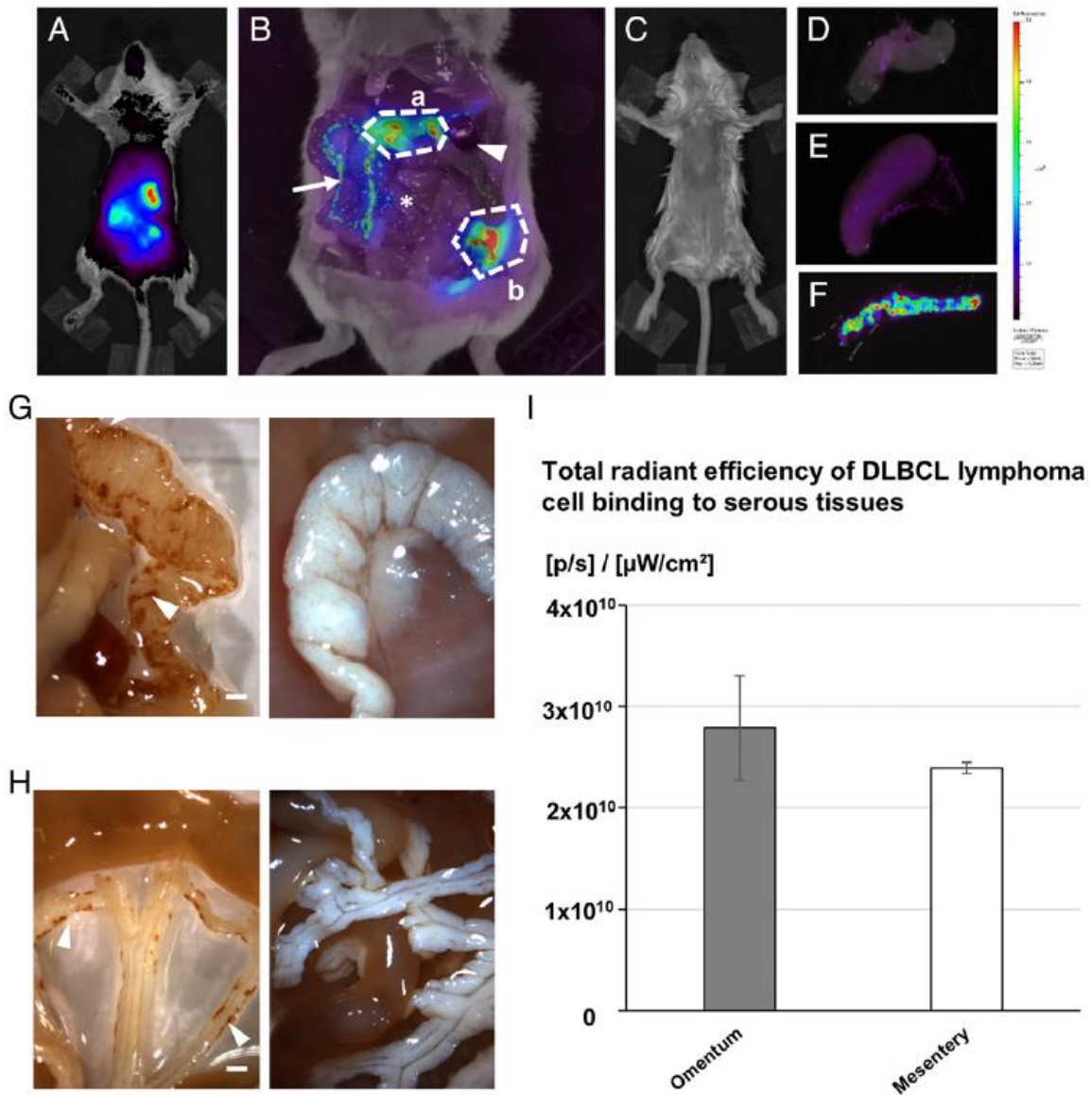
FIGURE 2. In vivo bioimaging of early lymphoma adherence to the peritoneum. (A) Transabdominal imaging with three diffusely labeled areas 4 h after injection of XenoLight DiR–labeled Bc.DLFL1 cells; (B) several gut-associated bead-like accumulations of lymphoma cells are distinguishable along the mesentery (arrow) and in the omentum (indicated with polygon "a"). Polygon "b" indicates the injection site at the left abdominal region. Note the absence of fluorescence signal in the mLNs (labeled with "*") and spleen (labeled with arrowhead). (C) Uninjected sample for imaging setting. (D) Ex vivo separated mLN or spleen (E) are devoid of detectable signal, while omentum (F) shows robust signal emission (representative of three mice). (G) Wholemount immunohistochemical detection of omental clustering of CFSE-labeled Bc.DLFL1 lymphoma cells using anti-FITC–PO detection resulting in brown precipitate (left) 4 h after injection (arrowheads) compared with uninjected control (right). (H) Mesenteric adipose tissue stained with anti-FITC–PO resulting in brown precipitate for CFSE-labeled Bc.DLFL1 lymphoma cells (arrowheads) arranged in a chain (left) compared with uninjected sample (right) after anti-FITC immunohistochemistry. Scale bars, 1 mm. (I) Quantitation of XenoLight DiR–labeled Bc.DLFL1 lymphoma binding to omentum and mesentery by total radiant efficiency (n = 6 mice per group).
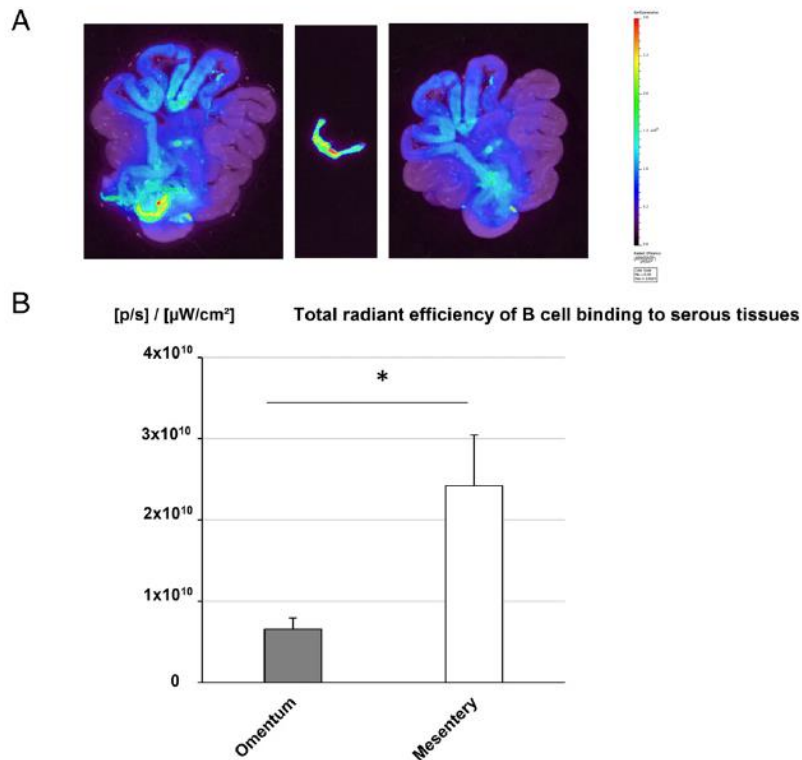
20

FIGURE 3. Serous accumulation of B cells after i.p. injection. (A) Accumulation of Xeno-Light DiR–labeled and MACS-purified B cells 4 h after injection, detected NIR fluorescence imaging in the whole gut–spleen–omentum (Om) complex (left); isolated Om (middle) and residual gut-spleen complex (right) compared with the intensity range (colored bar reference). Representative sample (n = 5 mice per group) repeated twice. (B) Quantitation of the binding of XenoLight DiR–labeled B cells to Om and mesentery (Mes) by total radiant efficiency (n = 6 mice per group). *p< 0.05.
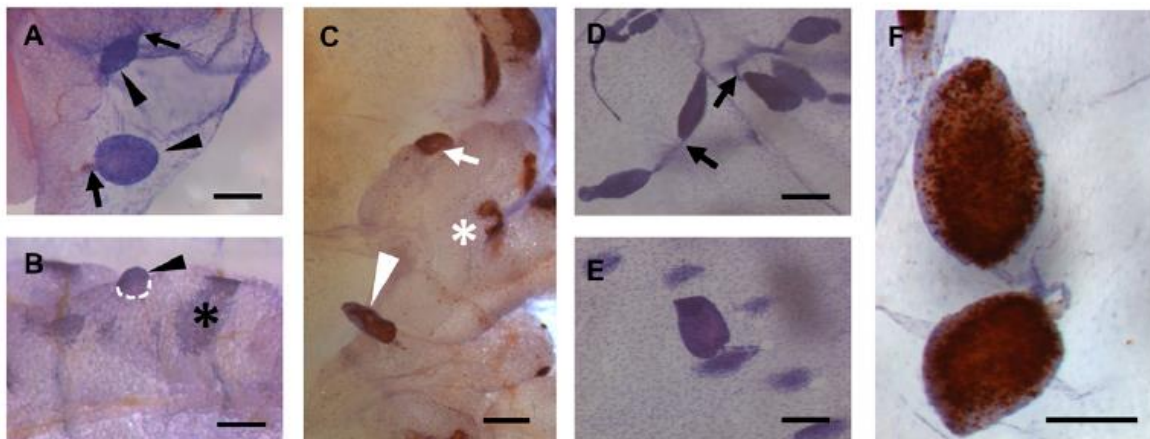

FIGURE 4. Appearance of lymphoma-binding serous lymphoid organoids. (A) Hematoxylin-stained single FLAgs (arrowhead) connected to mesenteric fat via slender stalks (labeled with arrows). (B) Omental lymphoid formations also include crescent-shaped protrusion (labeled with arrowhead) and diffuse MS (labeled with "*"; hematoxylin stain). Note the extended perimeter of the base (dotted line) of a typical protrusion connecting to the adipose tissue and the absence of stalk. (C) CFSE-labeled Bc.DLFL1 cells attach to mesenteric FLAgs (arrowhead), FALCs (*) and protrusion (arrow), visualized by brown anti-FITC–PO staining. (D) In the bursal membrane, the FLAgs typically occur in paired arrangement attached to the two sides of the peritoneum through slender stalks (indicated with arrows). (E) A solitary FLAg attached to the bursal peritoneum. (F) Bursal FLAgs efficiently bind CFSE-labeled Bc.DLFL1 cells 4 h after i.p. injection (anti-FITC–PO staining, brown). Scale bars, 200 μm.

Following the visualization of intraperitoneally injected Bc.DLFL1 cells we found leaf-like formations, which are either connected to the mesenteric fat directly or through a stalk [Fig. 4A,B], both types showing robust uptake of Bc.DLFL1 cells [Fig. 4C]. Moreover, such formations were also observed on the omental bursa membrane mostly with paired

21

appearance [Fig. 4D-F]. Owing to these morphological characteristics, we named these structures as foliate lymphoid aggregates (FLAgs). To exclude that these structures are only present in the normal BALB/c mice, we also analyzed C57BL/6J mice. We could identify the same structures in 8 to 10 weeks old C57BL/6J mice.

The appearance of FLAgs is quite distinct from the diffuse forms of serous leukocyte clusters, such as milky spots (MSs) or fat-associated lymphoid clusters (FALCs). We further investigated their lymphoid composition by whole-mount immunohistochemistry. We found intense CD45 expression throughout the whole FLAg and less intense labeling of FALC [Fig. 5A]. Anti-Thy1/CD90 staining reveals a compressed T-cell region in the center of the FLAg body [Fig 5B], whereas B-cell staining appears more even [Fig. 5C]. LYVE-1 positive macrophages accumulate at the edge of the FLAg [Fig. 5D].

With dual immunofluorescence for Thy-1 and IgM we confirmed the T-cell accumulation in the center, while B cells congregate at the peripheral regions [Fig. 5E]. The T/B cell segregation suggested distinct chemokine guidance, which was verified by labeling for Thy-1 and B220 together with either CCL21 or CXCL13. The CCL21 production was more concentrated at the center where T cells resided and CXCL13 spread more widely [Fig. 5F,G]. All these data indicate the presence of various domains within FLAgs, recruiting different lymphocytes through homeostatic chemokine production.
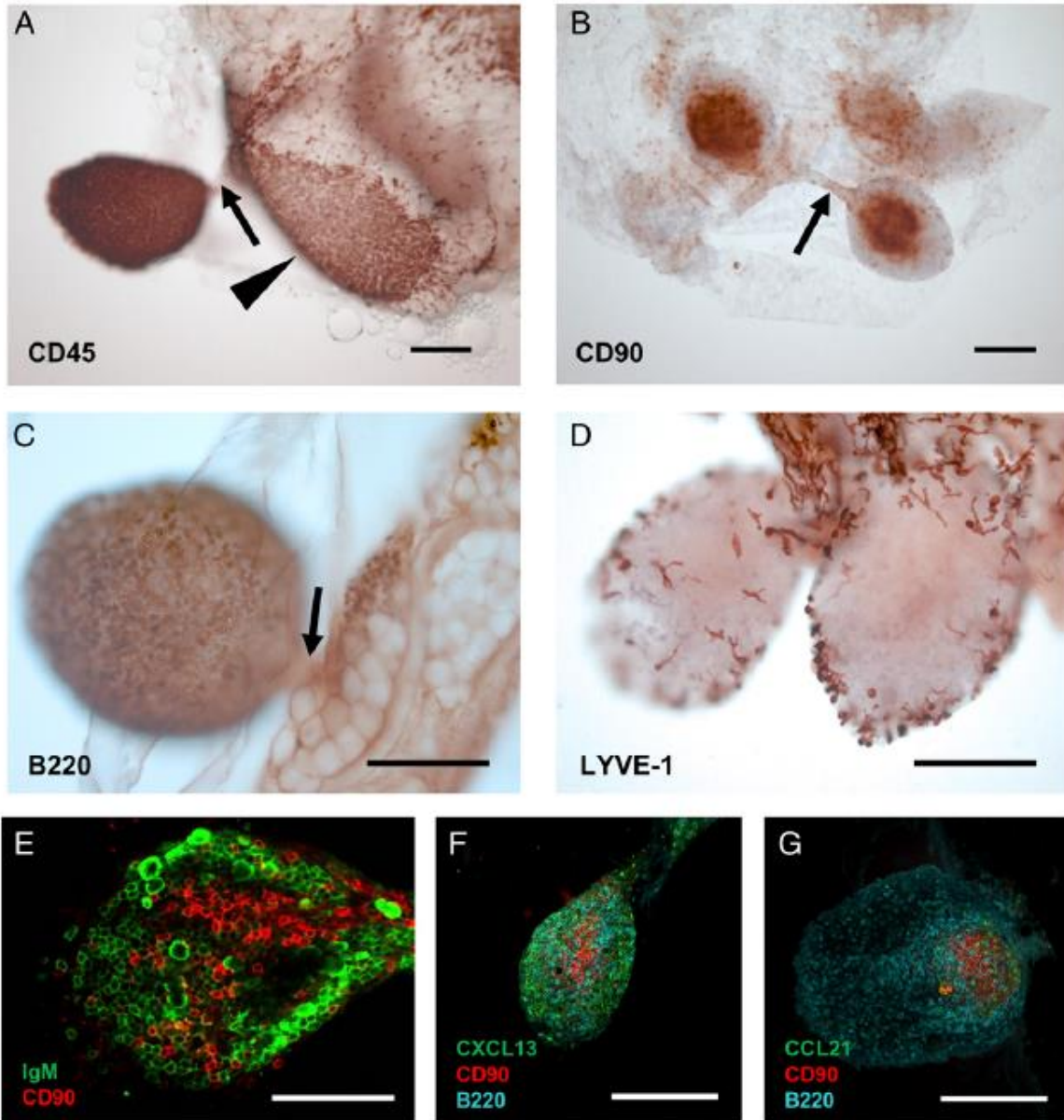
FIGURE 5. Lymphoid organization and homeostatic chemokine domains of FLAgs. Omental (A), membrane-bound (B), and mesentery-associated variants (C and D) were labeled for the markers as indicated using indirect immunohistochemistry and DAB reaction (brown) of whole-mount samples. Arrows in (A)–(C) mark stalk, arrowhead in (A) points to a FALC/MS. (E) Partial T/B compartmentalization revealed with anti-IgM (green) and anti-CD90/ Thy-1 (red) dual immunofluorescence by confocal microscopy (2.5-mm optical section thickness). (F) B cell chemoattractant CXCL13 (green) is expanded in the peripheral segment enriched for B cells (turquoise) with a relative paucity in the region with T cell clustering (red). (G) Focal accumulation of CCL21 (green) adjacent to T cell clustering (red) and its absence in the B cell populated region in membrane-associated FLAg. Scale bars, 200 μm (representative figure, n = 5 mice per group, repeated twice).

Subsequent electron microscopic inspection gave us a better resolution of FLAg structure, demonstrating that the FLAgs are covered with a single mesothelial layer. A capillary-rich region underneath this thin cover is tightly packed with lymphocytes [Fig. 6A-C], including plasma cells. In the deeper region plasma cells with extended endoplasmic reticulum also appear among the reticular cells, usually as single cells or doublets as evidenced by anti-CD138 whole-mount immunohistochemistry [Fig. 6D-F].
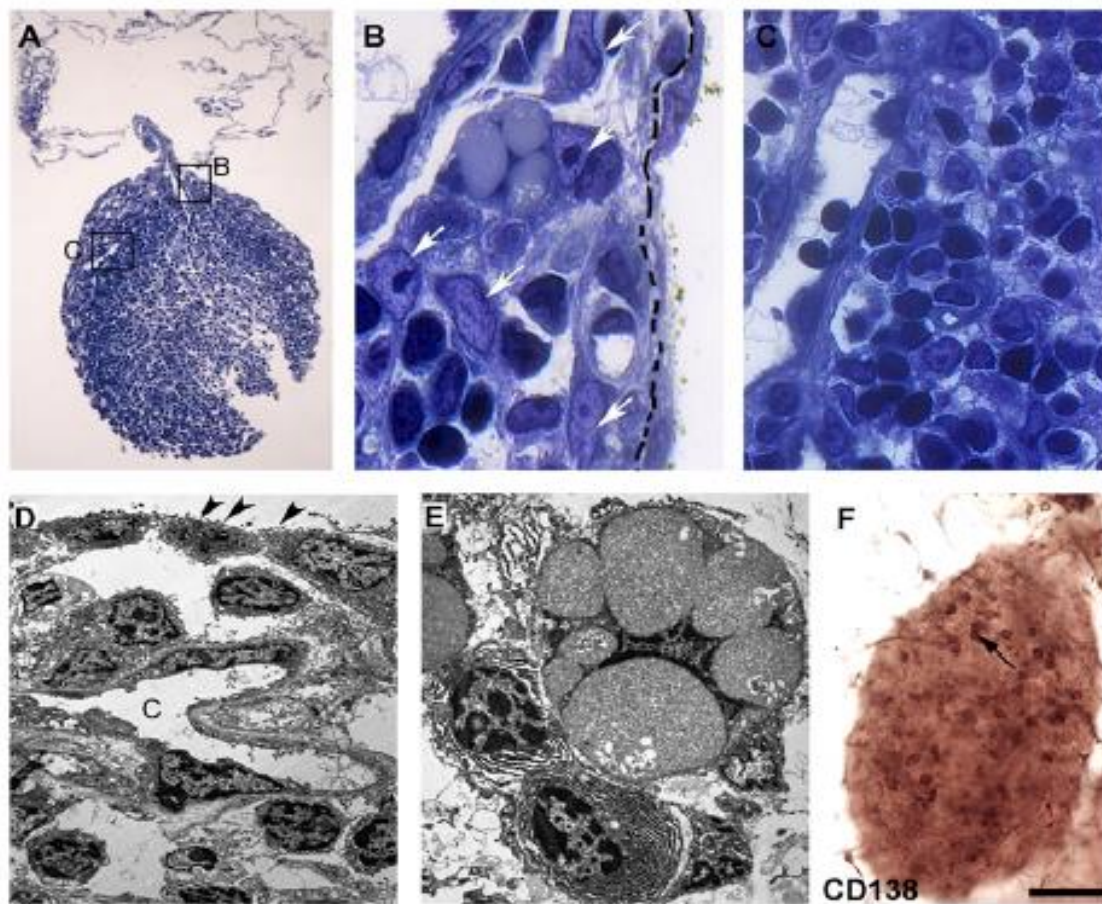

FIGURE 6 Ultrastructure of FLAgs. (A) One micron thin longitudinal section of a FLAg with the stalk attachment to the peritoneal membrane, stained with toluidine blue. (B and C) High-power magnification views of the boxes marked in figure (A). (B) The surface of the FLAg is covered by mesothelial cells (dashed line). Reticular cells [arrows in (B)] and lymphocytes [in (C)] fill the FLAg body. (D) Electronmicrograph of the FLAg's central part showing mesothelial cells with microvilli (arrowheads), one capillary (C), and the extravascular region populated by lymphocytes. (E) High-power magnification electron micrograph showing two adjacent plasma cells containing extensive endoplasmic reticulum. (F) Representative image of anti-CD138 whole-mount immunohistochemistry of FLAgs shows single or paired (arrow) plasma cells (n = 6). Scale bar, 100 μm.

The capillaries and reticular cells in FLAgs suggested the stable organization of FLAgs. We found an extensive network of fibronectin (Fn) meshwork throughout the FLAgs and along the stalk. By labeling with anti-VCAM-1 antibody, we found a strong capillary staining along

the stalk, with some reticular cells in the FLAgs [Fig. 7A, B]. Anti-CD31 staining revealed a rich meshwork of blood capillaries. Furthermore, PNAd-positive segments, indicating putative high endothelial venules, could also be detected [Fig. 7C].

Since FLAgs harbor lymphocytes, we next studied the presence of lymphatic vasculature in the FLAgs. In Prox-1 GFP reporter mice, we found there were only few GFP+ cells scattered in FLAgs [Fig. 7D]. In contrast, LYVE-1 staining showed a discontinuous pattern of macrophages at the edge of the FLAgs, similar to MSs and FALCs (17). These results suggest that the lymphatics are absent in such structures [Fig. 7E,F].
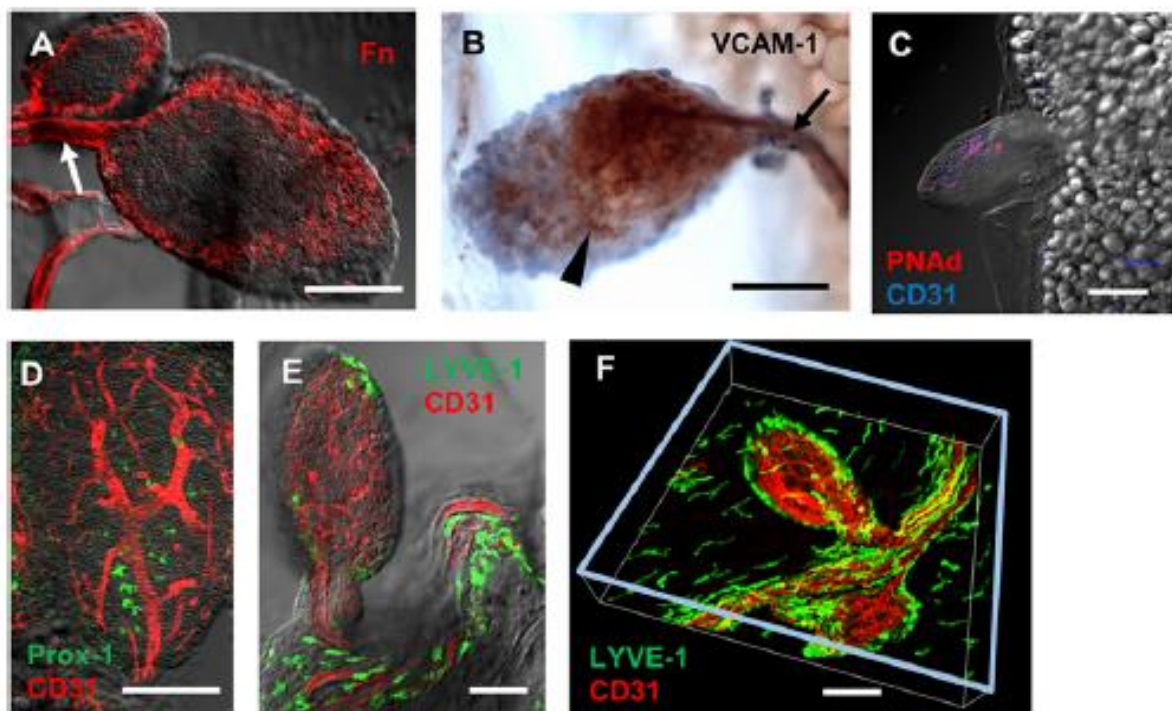

FIGURE 7. Stromal organization and patterning of FLAgs. (A) Peritoneal membrane-bound FLAg labeled for Fn reveals a dense Fn meshwork throughout the FLAg body, extending into the FLAg stalk (indicated with an arrow) with differential interference contrast (DIC) image background.(B) Anti–VCAM-1 immunohistochemistry (brown/DAB staining) of a mesentery-associated FLAg shows one capillary within the stalk (arrow) and several reticular cells with branched appearance in the FLAg body (arrowhead). (C) Within the extensive capillary meshwork in mesentery-associated FLAgs stained for CD31 (blue), short PNAd-positive segments (purple) are present. (D) Dispersed cells with Prox-1/GFP (green) expression correlated with CD31 (red) endothelial staining indicates the absence of defined lymphatic capillaries. (E) LYVE-1 staining (green) in combination with CD31 (red) labeling also demonstrates the lack of LECs, with strongly LYVE-1–positive cells displaying macrophage features. (F) Three-dimensional (3D) reconstitution of Z-stacks containing rich CD31-positive (red) capillary meshwork, with LYVE-1–positive macrophages (green) enriched at the edge of FLAgs, also present as individually dispersed cells in the peritoneal membrane. Scale bars 50 μm. (representative figures, n = 6 mice per group, repeated twice).

Normal lymphocyte homing to serosal lymphoid tissues is partly PNAd dependent

The presence of PNAd+ segments in the FLAgs suggested that the leukocytes' extravasation may be mediated by PNAd ligand L-selectin, similarly to the homing to pLNs. To test if blocking L-selectin alters the extravasation of lymphocytes from blood circulation, we performed a competitive assay by injecting isolated lymphocytes from KikumeGR mice (43). The KikG cells were pre-treated by anti-L-selectin mAb MEL-14 and mixed with red photoconverted KikR cells, followed by i.v. injection into recipients. 1 hour later, the cells were collected from different organs of the recipients, and were analyzed by flow cytometry. We found there was a dramatic blockade of KikG+ donor cell entry in the pLNs; however, the spleen was unaffected as we expected. Compared to the pLN, nearly 50% reduction of homing inhibition upon MEL-14 treatment occurred in the mesenteric fat [Fig. 8A,B]. The Kik cells in the omentum were hardly detectable in this period of time.

To test for mRNA features of core proteins and glycosylation enzymes for MECA-79 epitope of PNAd critical for HEV binding, we performed quantitative PCR, revealing that Cd34, Emcn and Podxl core protein mRNA and Cgnt2 enzyme mRNA levels were significantly increased, whereas mRNA of Glycam1 core protein, Icam, Cgnt1 B3gnt3 and Fut7 showed variable expression. [Fig. 8C] All these data indicate that the blood-borne lymphocytes migrate to serous lymphoid tissues involving the interaction between L-selectin and MECA-79 positive local HEVs that produce several core proteins and modifying enzymes.
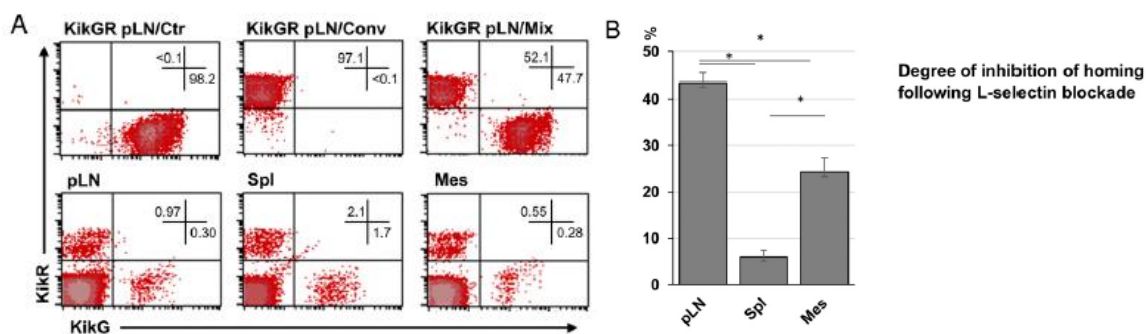
C Differential expression of mRNA for the production of MECA-79 core proteins and glycoepitope modifying enzymes
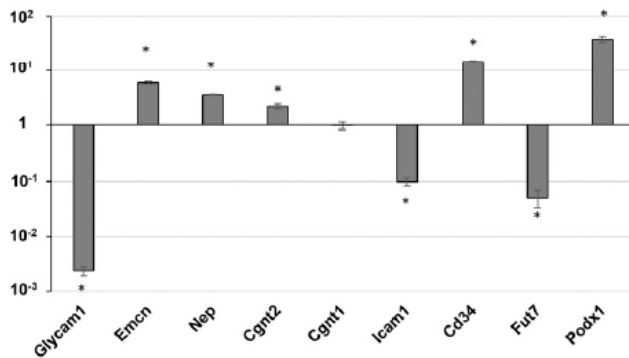
FIGURE 8. Partial L-selectin dependence of serous homing and mRNA profile of omental PNAd production. (A) Flow cytometric identification of lymphocytes from unconverted KikG (top left) and converted KikR (top middle) lymph nodes and their mixture (top right) gated on FSC/SSC/CD45, with the frequency of cells in the corresponding quadrants indicated in the upper-right quadrant of the density plots, with the KikG/KikR parameters indicated at the horizontal and vertical axes. In the bottom row, the KikG/KikR distribution is shown in pLNs, spleen (Spl), and mesentery (Mes) from mice injected with a mixture of anti–L-selectin, mAb-treated KikG and untreated KikR lymphocytes (representative figures from a group of three mice). (B) Quantitation of the degree of inhibition of tissue homing of KikG lymphocytes by MEL- 14 mAb 2 h after the injection of KikG/KikR lymphocyte mixture (n = 3 mice per group). (C) Comparison of core protein and glycosylation enzyme mRNA involved in the production of MECA-79 in the omentum and lymph nodes by quantitative PCR (qPCR). The ratios of target gene/β-actin mRNA ratio are depicted, in which the pLN value is indicated as 1 (average 6 SEM,n = 3 mice/group). *p< 0.05.

Selective homing of Bc.DLFL1 on serosa in the peritoneal cavity through lymphatics

As the tumor progression will eventually reach mesenteric lymph nodes, we further tracked the lymphoma cells within the mesenteric lymphatic capillaries using CFSE-labeled Bc.DLFL1 cells and anti-FITC whole-mount immunohistochemistry. We found the congregation of CFSE-labeled lymphoma cells within mesenteric lymphatic vessels. To confirm the migration of the tumor cells into the capillaries, we also injected CTFR-labeled Bc.DLFL1 cells into Prox1-GFP BALB/c mice whose lymphatic endothelial cells (LECs) are GFP-positive. We found that as early as 4 hours after i.p injection, lymphoma cells have already entered the lymphatic capillaries in the mesentery [Fig. 9A-C].
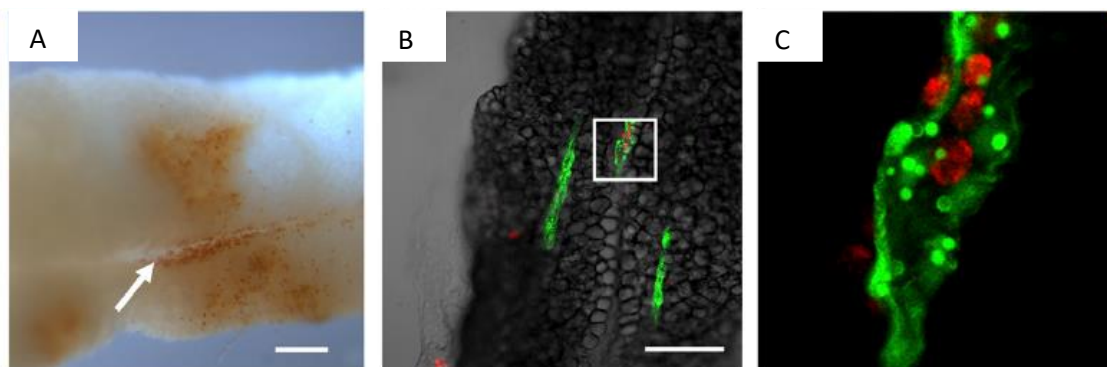
FIGURE 9. DLBCL binding to LYVE-1–positive macrophages and entry into Prox1-positive lymphatic vessels. Congregation of CFSE-labeled lymphoma cells (A) (detected with anti-FITC–HRP, brown) around and within a thin-walled mesenteric lymphatic vessel (arrow). Scale bar, 1 mm. (B) Using dual fluorescence CTFR-labeled cells (red) are positioned within or adjacent to these structures expressing Prox1GFP. Scale bars, 200 μm. (C) A higher magnification of the region outlined with a rectangle in (H) is demonstrated. Representative image from a cohort of three mice.

Intracellular and cell surface markers of tumor cells indicate the connection between Bc.DLFL1 and ABCs

Earlier analysis of Bc.DLFL1 cells established their CD19, B220, MHC Class II antigen and MAC-1 expression, indicating mature B cell origin, without expressing CD21 and CD23 [Fig. 10]. In comparison with A20 (a traditionally used high-grade B-cell lymphoma) expressing CXCR5 on the cell surface, Bc.DLFL1 cells show CCR7 chemokine receptor expression and the lack of CXCR5. Those data suggest Bc.DLFL1 is from extrafollicular and non-B-1a cell origin [Fig. 10].
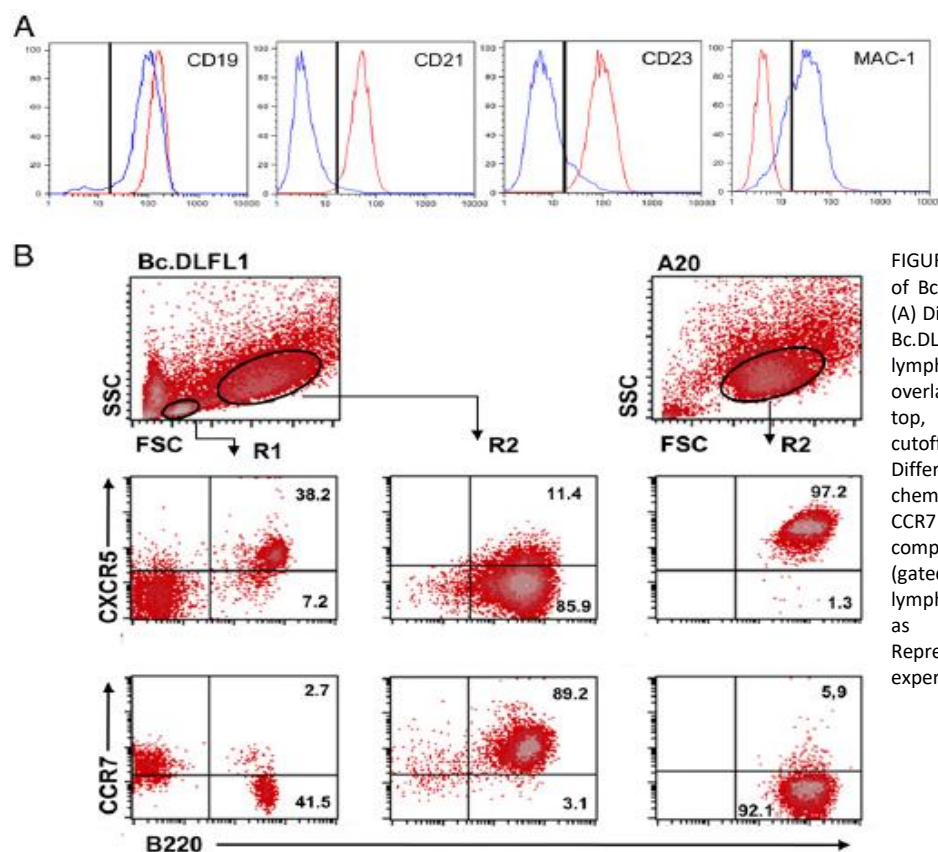
FIGURE 10. Surface characteristics of Bc.DLFL1 and A20 DLBCL cells. (A) Different surface phenotype of Bc.DLFL1 (blue) and A20 (red) lymphoma cells in histogram overlays (markers indicated at the top, vertical line indicates the cutoff for control labeling). (B) Differential expression of chemokine receptors CXCR5 and CCR7 in Bc.DLFL1 and A20 cells in comparison with normal B cells (gated on live B220- positive lymphocytes [R1] or blast [R2] cells as defined by FSC/SSC). Representative sample of an experiment repeated twice.

Furthermore, we tested CXCR4 expression together with CXCR7/ACKR3 which is also a receptor for CXCL12 (54, 55). We found that the majority of the Bc.DLFL1 cells are CXCR4 positive, but lack CXCR7 [Fig. 11].

CXCR4 expression has been reported for a minor CD11c-positive age-associated B cells (ABC) located at extrafollicular sites of the spleen (30). Therefore, we next investigated whether Bc.DLDL1 cells display CD11c. We found a high-level expression of CD11c. In addition, we also identified a CD19-, B220- CD11c+, MHC Class II^{hi} population as dendritic cells (Fig. 11B) occurring in the lymphoma (56). In order to study CD11c+ DCs distribution, we stained the spleen sections from the metastatic spleen of Bc.DLFL1 for B220 and CD11c. The staining results show that the CD11+ DCs were detectable among the B220^{dim} Bc.DLFL1 cells [Fig. 11C].

The CD11c-positive ABC subset also typically expresses T-bet transcription factor (30, 31, 57). By flow cytometry, we could detect the presence of T-bet in Bc.DLFL1 cells, whereas the normal residual B cells remained negative. In addition, Blimp-1, which plays a role in the plasmacellular differentiation of activated B cells, was also expressed by Bc.DLFL1 cells. [Fig.11D,E]. However, CD138, a typical marker for differentiated plasma cells, was not expressed (not shown). Moreover, Bc.DLFL1 cells share the similar high-level expression of CD80 and CD86 activation markers with normal murine ABC pool (26, 32). These results suggest the relationship of Bc.DLFL1 cells with ABCs, committed towards plasmacellular differentiation without reaching full maturation.

T-bet positive ABCs often exhibit the qualities of memory B cells (26, 30), so we further studied whether the V_H-region of Bc.DLFL1 lymphoma cells contains some point mutations. The variable region was amplified from cDNA and the consensus sequence was aligned with germ-line mouse IgV$_H$-region (GenBank accession no. MW191849). The result indicated that the V_H region of lymphoma contains 11 non-silent mutations and 1 silent mutation. In addition, staining Bc.DLFL1 cells for antibody production revealed intense cytoplasmic staining using anti-mouse IgG2a isotype-specific detection, indicating heavy chain isotype switch, in addition to variable region somatic mutation.

Overall, those data suggest that Bc.DLFL1 lymphoma is of ABC origin displaying Blimp-1 and IgG2a positive plasmablastic features; however, lacking the expression of CD138.
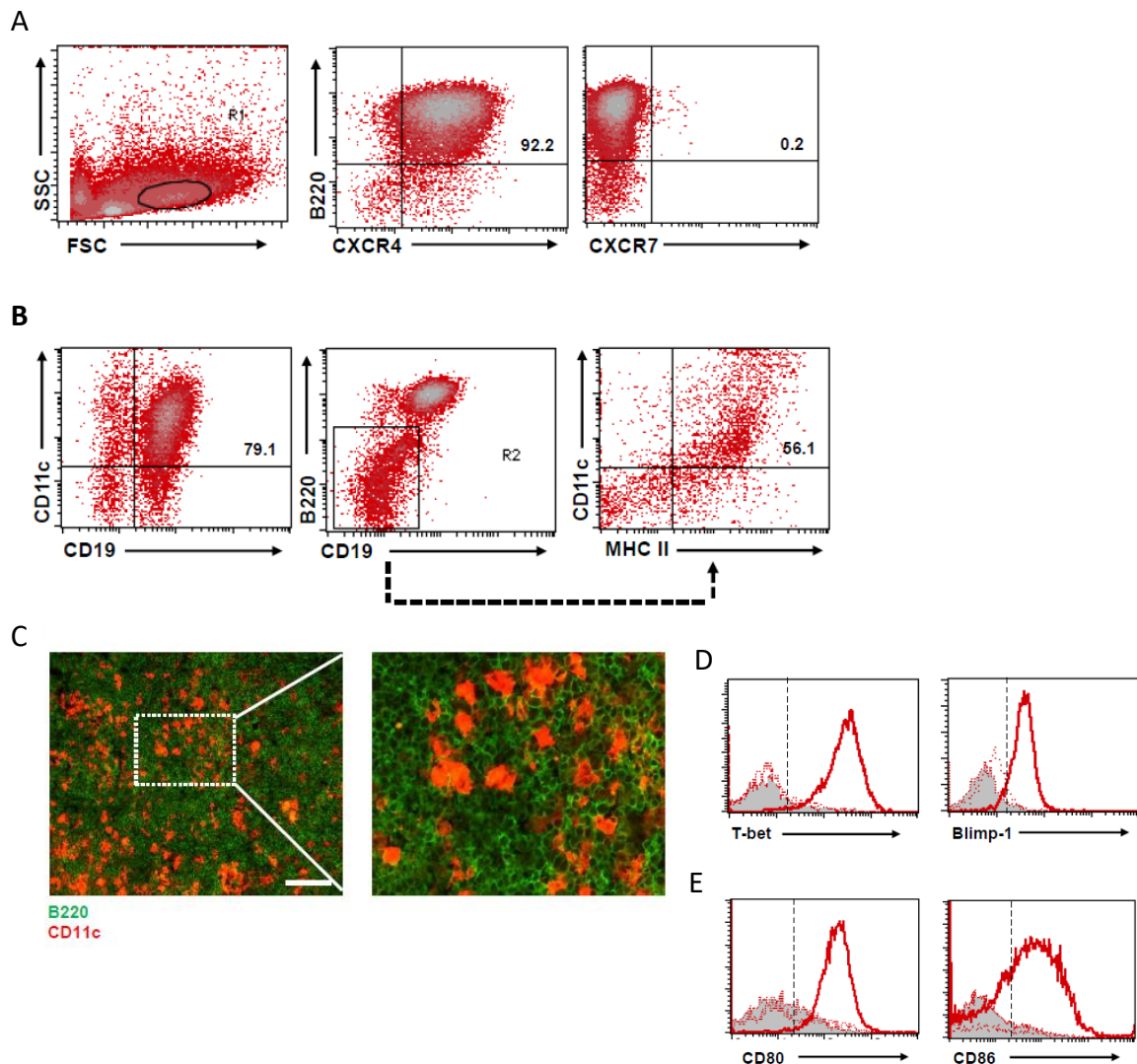

FIGURE 11. Bc.DLFL1 cells express CXCR4 chemokine receptor and CD11c, and intermingle with CD11c+ dendritic cells. (A) Flow cytometric analysis illustrates lymphoma cells from mLNs gated on R1 according to size (FSC) and granularity (SSC, left), stained for B220 and CXCR4 (middle) or its decoy analogue, CXCR7 (right). The numbers in upper right quadrants correspond to the frequency of R1-gated double positive cells, indicating the production of CXCR4 and the absence of CXCR7 on the lymphoma cells. Representative images from a cohort of n=3 mice. (B) Lymphoma samples from mLN were labeled with CD19 and CD11c by flow cytometry, revealing CD11c expression by the lymphoma cells (left; the number indicates the frequency of FSC/SSC-gated [R1] lymphoma cells). Further gating on B220/CD19 double-negative non-B cells (R2, middle) stained for MHC II and CD11c demonstrates the presence of MHC II^{hi} CD11c+ dendritic cells (right). Representative images from a cohort of n=3 mice. (C) Staining of mLN sections from lymphoma-bearing mice (10 days after injection of Bc.DLFL1 cells) for B220 and CD11c demonstrates diffuse distribution of dendritic cells in the lymphoma tissue (representative images from a cohort of n=4. Scale bars correspond to 100μm). Central region outlined with dotted rectangle at a higher magnification is shown on the right. (D) Bc.DLFL1 lymphoma (indicated by thick red line) produces T-bet (left) and Blimp-1 (right) transcription factors suggesting ABC-derived plasmablastic origin. Lymphoma cells (thick red line in the histogram overlays) were compared to residual normal B cells (dashed red line) and non-B cells (grey filling with red line). Vertical dashed lines in the histogram overlays correspond to the isotype-matched control with less than 1% of positive cell frequency. Representative data from a cohort of n=3 mice. (E) Staining for CD80 and CD86 reveals increased expression on lymphoma cells (thick red line in the histogram overlays) compared to residual normal B cells (dashed red line) and non-B cells (grey filling with red line). Vertical dashed lines correspond to the isotype-matched control with less than 1% of positive cell frequency. Representative images from a cohort of n=3 mice

Bc.DLFL1 cells concentrate in the exrafollicular region of the spleen

Chemokines critically define cell migration, and our previous findings for chemokine receptor expression suggested extrafollicular preference of Bc.DLFL1 cells. Therefore we next investigated whether the distribution in the spleen after i.v. injection of lymphoma cells shows any similarities as ABCs (32). To be able to trace the lymphoma cells, we transfected Bc.DLFL1 cells with lentiviral particles encoding ZsGreen1 fluoroprotein followed by FACS sorting of ZsGreen1+ cells [Fig. 12A,B].12 hours after the iv. injection of Bc.DLFL1 ZsGreen1 cells, we found that most of the cells congregated at the extrafollicular parts of the white pulp in spleen, including marginal zone (MZ) and red pulp, defined by MARCO labeling of MZ macrophages [Fig. 12C].
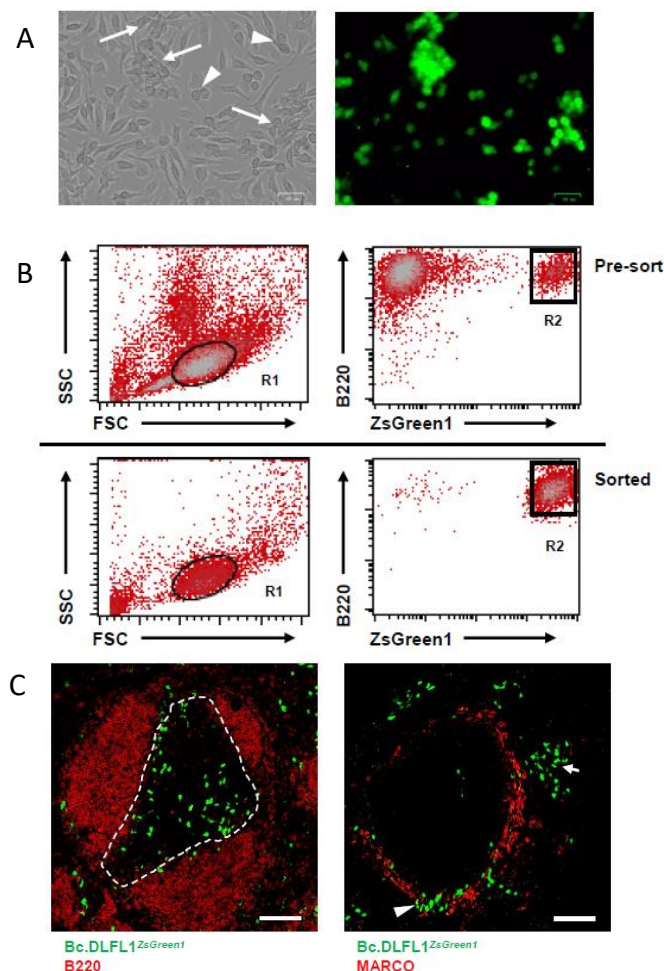

FIGURE 12. Production and isolation of Bc.DLFL1^{ZsGreen1} lymphoma cells. (A) Bc.DLFL1 cells were transduced with ZsGreen1-encoding lentiviral particles and were cultured on peritoneal exudate cells (PEC), viewed under ZOE imager using brightfield illumination (left) and 488 excitation filter (right). Note the lack of green fluorescence in elongated adherent PEC feeder cells and intense green fluorescence in the lymphoma colonies (arrows) or doublets (arrowheads). Scale bar: 33 μm. (B) Transduced lymphoma cells were labeled with anti-B220 AF647 conjugate and sorted. B220-positive Bc.DLFL1 cells (ellipse region R1) producing ZsGreen1 (rectangle region R2) were sorted over 98% purity. (C) Following intravenous injection of ZsGreen1-expressing Bc.DLFL1 cells (green), 12 hours later the lymphoma cells within spleen are located in the T-cell zone (outlined with dashed line) within the white pulp, excluded from the follicles (delineated by anti-B220 staining, red, left), and also accumulate in the red pulp (arrow) and in the marginal zone (arrowhead, identified by anti-MARCO (red) labeling, right). Representative confocal microscopic images from a cohort of n=4. Scale bars correspond to 100μm.

31

BAFF-R blockade prolongs the survival of lymphoma bearing mice

The survival of mature B cells in peripheral lymphoid tissues critically depends on BAFF, therefore we tested the expression level of BAFF-receptor (BAFF-R) and its analogues BCMA and TACI. Our results showed that Bc.DLFL1 cells display high level of BAFF-R and TACI, whereas BCMA staining did not show higher expression compared to normal B cells. [Fig.13A]. To further study the function of BAFF-R in the disease progression, we intravenously injected mBR3-Fc as soluble BAFF-R decoy receptor (58) or control mouse IgG1 on days 1,4,6,8 after i.p. lymphoma administration. The mice in the control group started dying by day 13 with a rapidly increasing death rate during the next 4 days. In contrast, there was only one mouse deceased in the treated group by day 18, whereas only three mice survived in the control group [Fig 13B]. These data suggest the mBR-3Fc treatment will efficiently prolong the survival of the mice under the tumor burden.
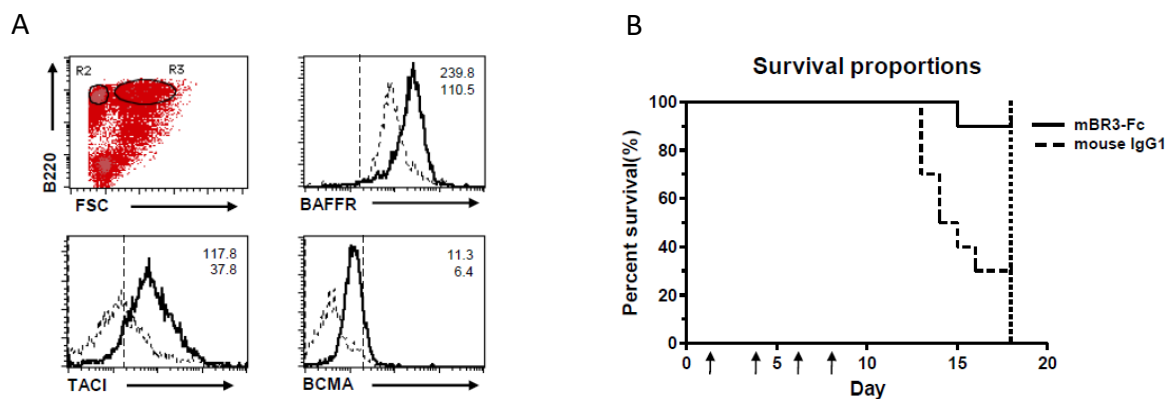

FIGURE 13. Expression of BAFF receptors by Bc.DLFL1 cells and the effect of BAFF-R antagonization by mBR3-Fc on the survival of lymphoma-injected mice. (A) mLN cells from lymphoma-injected resolved into residual B cells (R2) and larger lymphoma cells (R3) were analyzed for the various analogues of BAFF receptor by flow cytometry. Histogram overlays represent the expression of various receptors as indicated, with Bc.DLFL1 cells (thick lines) compared to residual B cells (dashed lines). Numbers indicate the mean fluorescence intensity (MFI) values for the markers by Bc.DLFL1 cells (upper values) or normal B cells (lower values). Vertical dashed lines correspond to the isotype-matched control with less than 1% of positive cell frequency. Representative images from a cohort of n=3 mice. (B) Kaplan-Meier curve of the survival following BAFF-R antagonization showing the percentage of surviving animals (*y* axis). Using a cohort of n=10 mice, the mice received iv. injections of 100μg/mouse mBR3-Fc decoy receptor (continuous line) or mouse control IgG1 (dashed line) on four different days (D1, D4, D6, D8, *x* axis) after the ip injection of Bc.DLFL1 lymphoma on D0, indicated by arrows. The vertical dotted line represents the termination of experiment on D18.

Alterations of stroma elements and tissue-specific cytokine landscape

In mice with advanced stage of tumor we also noticed that the mesenteric and omental fat had become thickened and fragile when we harvested the lymphoma from mesenteric fat, indicating the lymphoma infiltration of the adipose tissue [Fig. 14A, B]. We further investigated the alterations in the adipose tissue caused by lymphoma proliferation. The lymphomatous replacement of the tissue was confirmed by anti-B220 and also Ki-67 immunohistochemistry [Fig. 14C, D].

As the lymphoma cells tend to accumulate and expand at extrafollicular locations where gp38/podoplanin positive fibroblastic reticular cells (FRCs) are located (59), we next examined whether any FRCs-like cells are present in the lymphoma-infiltrated adipose compartment. To ensure the stromal elements are of host origin, we used cytoplasmic eGFP transgenic mice as recipients for this experiment, and performed whole-mount immunofluorescence (44). At advanced stage of lymphoma, we found a network of gp38+/eGFP+ FRCs [Fig. 15 A-D] at the edge of the bulk of tumor labeled by anti-B220 antibody in the mesentery. In control mesentery from normal BALB/c^{eGFP} mice, the gp38-positive fibroblastic cells only appear at perivascular area, or randomly scattered amongst the eGFP+/gp38- negative adipocytes [Fig. 15E]. This finding indicates that the progression of lymphoma in the adipose tissue is coupled with the expansion of the microenvironment containing gp-38/podoplanin-positive FRCs of host origin.
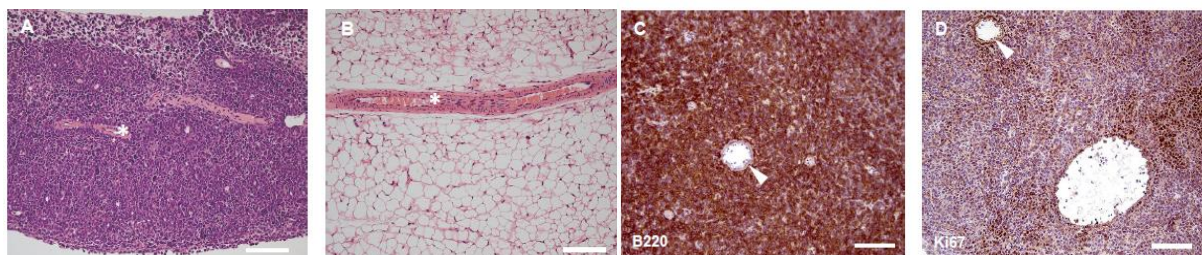

FIGURE 14. Extranodal growth of Bc.DLFL1 lymphoma cells in the mesentery. (A) HE staining of mesentery section from dissected mesentery shows large lymphoma infiltrate around the perivascular region (mesenteric artery indicated with *; representative image from a cohort of n=4 mice. Scale bar=200µm). (B) In normal mesentery from uninjected control the perivascular adipose tissue is devoid of leukocytes (mesenteric artery indicated with *; representative image from a cohort of n=4. Scale bar=100µm). (C) Anti-B220 staining of cryostate section of mesentery from lymphoma-injected mouse demonstrates perivascular accumulation of B220-positive Bc.DLFL1 cells (brown precipitate, with hematoxylin (blue) counterstain). Arrowhead points at mesenteric artery cross-section, scale bar=100µm. (D) Expression of Ki-67 proliferation-associated antigen (brown nuclear reactivity) demonstrates extranodal division of Bc.DLFL1 lymphoma cells both at perivascular (arrow points at the mesenteric artery) and more distant regions within the mesentery. Representative image from a cohort of n=4 mice. Scale bar=100µm.
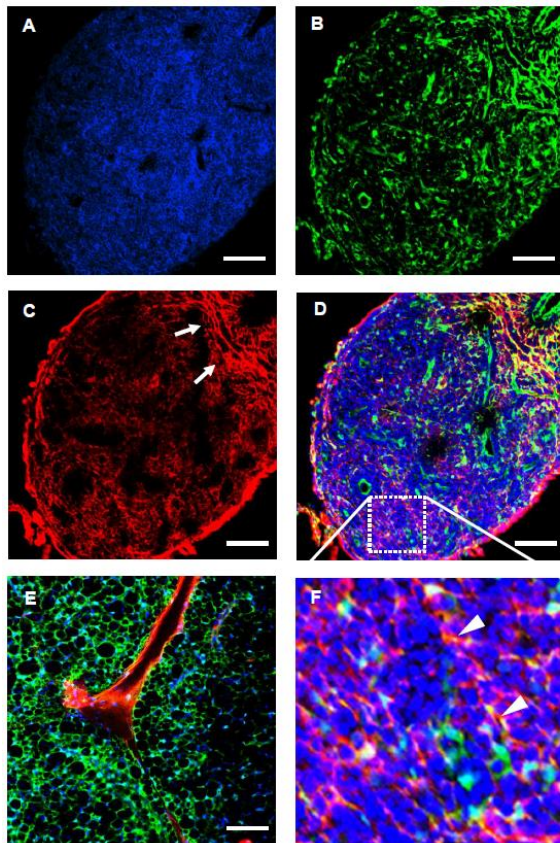
FIGURE 15. Expansion of gp38+ fibroblastic cells associated with the extranodal metastasis of Bc.DLFL1 lymphoma in the mesentery. (A) Lymphoma cells (stained with anti-B220, blue) form large clusters in the mesentery at advanced stage of lymphoma following ip injection. (B) In eGFP Tg BALB/c host mice the residual non-hematopoietic cells with fibroblastic appearance (green) extend throughout the lymphoma infiltrate in the mesentery at similar intensity of eGFP expression. (C) Staining of sections with PE-conjugated anti-gp38 (red) reveals extensive fibroblastic reticular cell (FRC) labeling with various intensities, with a more pronounced labeling at the periphery of the infiltrate (arrows). (D) Merged image of the Hoechst33342 labeled lymphoma cells, eGFP-expressing host non-hematopoietic cells and gp38-stained FRCs. The rectangular field outlined with dotted line is shown in F, demonstrating partial overlap between eGFP/gp38 as yellow color (arrowheads). (E) Whole-mount labeling for gp38 of normal mesentery from BALB/c^{eGFP} demonstrates only perivascular clustering of gp38-positive FRCs surrounded by adipocytes. Note the distinctive confluent lattice-like appearance of adipocyte-associated green fluorescence compared to FRC-related meshwork pattern of eGFP signal (B), with Hoechst33342 nuclear counterstaining (blue). Scale bars represent 100μm, representative images from a cohort of n=4 mice.

The lymphoma expansion in the adipose tissues may also alter the local cytokine microenvironment to support tumor growth associated with the presence of gp38 positive FRCs, in addition to BAFF receptor and ligand binding dependence. Therefore, we next studied the local cytokine profile of mesenteric lymph nodes, omentum and mesenteric fat from both groups of mice [Fig. 16A]. By comparing the results to tumor-free samples we found that the factors which are significantly increased in the mLN sample are commonly associated with endothelial activation and neoangiogenesis, such as E-selection and angiopoietins, mesenchymal proliferation (PDGF) and matrix metalloproteses (MMP2,3,9), and several chemokines (CXCL9, CXCL10, CXCL11 and CCL12). In omenta, we found a significant increase of plasminogen activator inhibitor-1 (PAI-1/Serpin E1) and lipocalin-2. Moreover, some chemokines (CXCL9, CXCL10 and 11) increased at moderate levels. In the mesenteric samples, we found that IL-28, ICAM-1/CD54 and insulin-like growth factor binding protein-1(IGFBP-1) show the highest increase [Fig. 16B]. Furthermore, the comparison of the cytokine alteration with all three types of samples revealed that the omentum and mesenteric fat show

the highest degree of similarity of the cytokine profile, followed by a lesser overlapping between mLN and omenta, and with the least similarity between mLN and mesentery [Fig. 16C]. These results suggest that the cytokine alteration in the progression of lymphoma is tissue-specific where mLN showed the most distinguishable variance, and the alterations were more similar in the two types of adipose tissue.
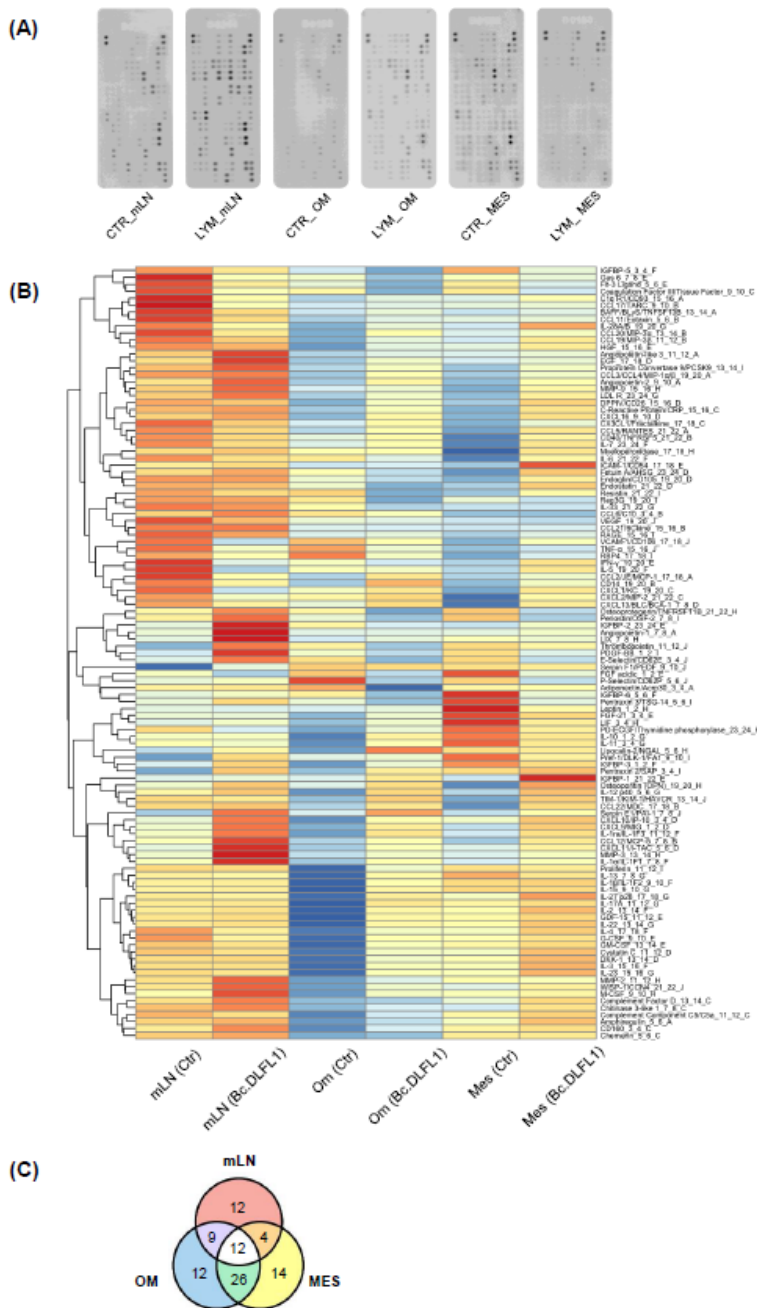
FIGURE 16. Alterations of cytokine profile associated with nodal and extranodal lymphoma expansion (A) Multiplex cytokine array reveals distinct patterns of alteration between lymphoma-infiltrated (LYM) mLN, omentum (OM) and mesentery (MES) in a pairwise comparison to normal (CTR) tissue samples. (B) The quantitative densitometric analysis summarizes the relative expression levels of various cytokine clusters. (C) The Venn-diagram summarizes the degree of overlap of (at least twofold) of extractable cytokines and soluble factors between nodal and extranodal sites. Numbers correspond to the number of factors either shared or restricted to one indicated source of sample.

Discussion

The peritoneal cavity represents a large internal surface area of the body, where the organization and homeostasis of its immunological components are largely unknown. Adipose tissues harboring lymphoid foci play an essential role in the local immune response. Recent results have indicated that, in addition to milky spots (MS), the mesentery and other visceral adipose tissues may harbor various lymphoid congregates that can engage in adaptive immune responses (7). Of these, first the MS on the omentum was reported containing macrophages, T cells and B cells with a diffuse appearance on the omental surface (60). Later FALCs were also found on the adipose tissue of various body cavities, which is also important for maintaining the local microenvironment (18). Both structures are similar in the cellular composition, and develop after birth (15,17) presumably related to normal intestinal flora and local immune response (17). This similarity has raised the view to consider both MS and mesenteric diffuse congregates as omental and mesenteric FALCs (7). Importantly, although these structures may engage in local immune responses, their role in the distribution of lymphocytes and collection of eventual intraabdominal tumor cells have not been fully revealed. As our findings demonstrate, the peritoneal lining also contains hitherto undescribed lymphoid tissue variations that we have identified during our investigations of the peritoneal dissemination of a spontaneous high-grade B-cell lymphoma cell line. The variant denoted as FLAg (foliate lymphoid aggregate) further extends the range of serosal lymphoid tissues (61).

In FLAgs, we could see more distinct cell compartmentalization where T cells are positioned in the center of the body, surrounded by B cells corresponding to CXCL13 and CCL21 chemokine production by the stroma elements, respectively. This segregation also determines the location of B-cell lymphoma variants, as CXCR5+/CCR7- A20 cells accumulated in the periphery, whereas CXCR5-/CCR7+ Bc.DLFL1 cells migrated into the central region of the FLAg body. Macrophages appear at the edge of the FLAgs or on the top of them, and their removal prevents both normal B-cell and B-cell lymphoma serosal binding, indicating their involvement in initial cellular adhesion. The FLAg also share some similarities

of the vascular arrangement with MS and FALC, where there is a rich meshwork of blood capillaries lined by CD31 positive blood endothelium. In FLAgs a short PNAd segments is also detectable, suggesting that blood borne lymphocytes may also enter FLAgs through these segments as entrance route. It appears therefore that there are two ways of cell migration to the serosal lymphoid formations: one is the surface passage for homing from the peritoneal cavity through LYVE-1-positive macrophages for MSs, FALCs and FLAgs, in a clodronate-sensitive mechanism, while the other one is through L-selectin mediated homing from blood circulation, latter for FLAgs. Their partial L-selectin dependence should be further scrutinized to explore other possible leukocyte ligands for HEV PNAd. In addition, the exit route of lymphocytes from FALCs and FLAgs may also include (a) reverse surface egress into the peritoneal cavity, or (b) vascular departure via blood capillaries present in FLAgs, or (c) their interstitial crawling towards the mesenteric lymphatic capillaries.

While the non-hematopoietic components also include VCAM-1-positive reticular cells and fibronectin-containing extracellular matrix, their identity remains undetermined. Moreover, further phenotypic analysis for putative stromal components will reveal possible stromal specification of FLAgs, even though the options are limited, due to the shortage of stromal subset-specific reagents. Bulk mRNA or scRNA-Seq from microdissected serosal organoids and comparison with other secondary lymphoid tissues should provide important clues concerning FALC/FLAg-specific stromal differentiation. Our current working hypothesis of the appearance of FLAgs is that MSs and FALCs represent the immature form of FLAgs, which will evolve as a result of local immune response. Furthermore, the details of FLAg development still remain uninvestigated.

Several lines of evidence suggest that the serosal lymphoid organoids in mice are responsible for the production of natural antibodies, and upon T-independent antigen stimulation mesenteric and omental FALCs/MSs can expand, in complex processes linking B-1 cells and ILC2 cells. The presence of CD138+ plasma cells in the FLAg body regions also indicate the occurrence of plasmacellular immune reaction. However, the cellular requirements for the formation and specific immunological functions of FLAgs (if any) require

further investigation, including their spectrum of tumor cell binding preferences beyond B-cell lymphoma adhesion, including ovarian and colorectal tumors (34, 38).

The selective binding characteristics of Bc.DLFL1 cells also necessitated a deeper analysis of these spontaneous B-cell lymphoma cells as models for diffuse large B-cell lymphoma (DLBCL). Our findings indicate that, despite its aggressive propagation within mesenteric lymph nodes and subsequently in spleen, its growth is largely restricted to these organs. Our extended phenotypic analysis revealing CD11c+ and CXCR4 co-expression and lack of CD21 and CD23, respectively, raised the possibility of their age-associated B-cell (ABC) origin (26–30). Owing to their possible role in immune aging and autoimmunity, this subset has recently been scrutinized in more details but, interestingly, its relevance to B-cell malignancies has not been addressed (62). The T-bet and Blimp-1 expression data, cell surface phenotypic as well as Ig genotypic findings demonstrating IgG2a isotype switch and CDR mutations, together with their in vivo distribution preferences strongly suggest that Bc.DLFL1 lymphoma cells may be a useable model for studying their physiological counterparts' features in more details. In addition, their extended genotypic analysis by whole exome sequencing for possible mutations that may be responsible for malignant transformation, may also offer clues relevant to human hematopathology.

Another aspect of the Bc.DLFL1 cell expansion, in addition to its autonomous growth features, is their relationship with their environment. The increased level of BAFF receptor and TACI clearly reveal some dependence for BAFF; however, the exact source producing this cytokine has not been determined yet. The presence of CD11c+ dendritic cells in the infiltrated lymph nodes suggests their support role; however, as the transient in vivo blockade of BAFF-R signaling via soluble decoy receptor mBR3-Ig could only postpone the mortality, other supportive factors also need to be considered. With the lineage-specific deletion of DCs using diphtheria-toxin induction the role(s) of DCs can specifically be addressed (63). Furthermore, the tissue-specific alterations of cytokine landscape and their overlaps between the omental, mesenteric and nodal tissue samples demonstrate that the extranodal expansion of DLBCL elicits differential effects, indicating parallel adaptation possibilities for lymphoma growth. This

tissue-specific difference may also have far-reaching consequences for the complex (tumor and environment simultaneously) treatment of human DLBCL as well. Further studies are likely to benefit from our studies on the serosal tissues as lymphoma harboring tissues.

.

New findings of my PhD research

1. We have identified murine FLAgs (foliate lymphoid aggregates) as novel forms of serosa-associated lymphoid organs with partly compartmentalized lymphoid structure, composed of a FLAg body and stalk connecting to the bursal peritoneum or the omental and mesenteric adipose tissue;

2. We have demonstrated that the entry of B cells and Bc.DLFL1 high-grade B-cell lymphoma cells from the peritoneal cavity to FLAgs involves LYVE-1-positive macrophages, whereas the homing of blood-borne lymphocytes is partly L-selectin dependent;

3. We have established that various B-cell lymphoma cells compartmentalize within FLAgs according to their chemokine receptor expression pattern, with CCR7 guiding Bc.DLFL1 lymphoma cells in the central region producing CCL21, and CXCR5 guiding A20 lymphoma cells to the peripheral rim of FLAg body containing CXCL13, respectively;

4. We have established that the FLAg body is arranged around VCAM-1–positive fibroblastic cells, and it contains an extensive CD31-positive vasculature;

5. We have identified mesenteric lymphatics as exit routes for the intraperitoneally injected B lymphocytes;

6. We have defined Bc.DLFL1 lymphoma cells as age-associated B-cell (ABC) derived lymphoma, expressing T-bet, CD11c and CXCR4 which, together with CCR7, directs their positioning to the splenic T-cell zone, marginal zone and red pulp, respectively;

7. We have established that the inhibition of BAFF-R ligand binding significantly promotes the survival of lymphoma-bearing recipient mice;

8. We have demonstrated that the adipose expansion of Bc.DLFL1 lymphoma cells alters the cytokine landscape in a tissue-specific manner, and causes expansion of gp38-positive fibroblastic reticular cells.

List of publications

My doctoral thesis is based on the following publications:

Jia X, Gábris F, Jacobsen Ó, Bedics G, Botz B, Helyes Z, Kellermayer Z, Vojkovics D, Berta G, Nagy N, Jakus Z, Balogh P. Foliate Lymphoid Aggregates as Novel Forms of Serous Lymphocyte Entry Sites of Peritoneal B Cells and High-Grade B Cell Lymphomas. J Immunol. 2020 204:23-36.* (IF: 5,422)

Jia X, Berta G, Gábris F, Kellermayer Z, Balogh P. Role of adipose-associated lymphoid tissues in the immunological homeostasis of the serosal surface. Immunol Lett. 2020 228:135-141. (IF: 3,685)

Jia, X., Bene, J., Balázs, N., Szabó, K., Berta, G., Herczeg, R., Gyenesei, A., & Balogh, P. (2022). Age-Associated B Cell Features of the Murine High-Grade B Cell Lymphoma Bc.DLFL1 and Its Extranodal Expansion in Abdominal Adipose Tissues. Journal of immunology (Baltimore, Md.: 1950), 208(12), 2866–2876. https://doi.org/10.4049/jimmunol.2100956 **(IF: 5,422)

Other publications related to this work:

Ritter Z, Zámbó K, Jia X, Szöllősi D, Dezső D, Alizadeh H, Horváth I, Hegedűs N, Tuch D, Vyas K, Balogh P, Máthé D, Schmidt E. Intraperitoneal Glucose Transport to Micrometastasis: A Multimodal In Vivo Imaging Investigation in a Mouse Lymphoma Model. Int J Mol Sci. 2021 22:4431. (IF: 5,923)

Ritter Z, Zámbó K, Balogh P, Szöllősi D, Jia X, Balázs Á, Taba G, Dezső D, Horváth I, Alizadeh H, Tuch D, Vyas K, Hegedűs N, Kovács T, Szigeti K, Máthé D, Schmidt E. In situ lymphoma imaging in a spontaneous mouse model using the Cerenkov Luminescence of F-18 and Ga-67 isotopes. Sci Rep. 2021 11:24002. (IF: 4,379)

Other Publication(s)

Khanfar E, Olasz K, Gajdócsi E, et al. Splenectomy modulates the immune response but does not prevent joint inflammation in a mouse model of RA [published online ahead of print, 2022 May 16]. Clin Exp Immunol. 2022;uxac052. doi:10.1093/cei/uxac052. (IF 5.732)

*Included in Top Reads (https://www.jimmunol.org/content/204/1/1)
**The cover of the June 15, 2022 issue of The JI (https://www.jimmunol.org/content/208/12.cover-expansion)

References

1. Cornes, J. S. 1965. Number, size, and distribution of Peyer's patches in the human small intestine: Part I The development of Peyer's patches. *Gut* 6: 225–229.

2. Liu, X., Y. Zhao, and H. Qi. 2022. T-independent antigen induces humoral memory through germinal centers. *J. Exp. Med.* 219.

3. Randall, T. D., D. M. Carragher, and J. Rangel-Moreno. 2008. Development of secondary lymphoid organs. *Annu. Rev. Immunol.* 26: 627.

4. McDonald, K. G., J. S. McDonough, B. K. Dieckgraefe, and R. D. Newberry. 2010. Dendritic Cells Produce CXCL13 and Participate in the Development of Murine Small Intestine Lymphoid Tissues. *Am. J. Pathol.* 176: 2367–2377.

5. Ansel, K. M., R. B. S. Harris, and J. G. Cyster. 2002. CXCL13 Is Required for B1 Cell Homing, Natural Antibody Production, and Body Cavity Immunity. *Immunity* 16: 67–76.

6. Meza-Perez, S., and T. D. Randall. 2017. Immunological Functions of the Omentum. *Trends Immunol.* 38: 526–536.

7. Cruz-Migoni, S., and J. Caamaño. 2016. Fat-associated lymphoid clusters in inflammation and immunity. *Front. Immunol.* 7.

8. Jackson-Jones, L. H., P. Smith, J. R. Portman, M. S. Magalhaes, K. J. Mylonas, M. M. Vermeren, M. Nixon, B. E. P. Henderson, R. Dobie, S. Vermeren, L. Denby, N. C. Henderson, D. J. Mole, and C. Bénézech. 2020. Stromal Cells Covering Omental Fat-Associated Lymphoid Clusters Trigger Formation of Neutrophil Aggregates to Capture Peritoneal Contaminants. *Immunity* 52: 700-715.e6.

9. Bénézech, C., E. Mader, G. Desanti, M. Khan, K. Nakamura, A. White, C. F. Ware, G. Anderson, and J. H. Caamaño. 2012. Lymphotoxin-β Receptor Signaling through NF-κB2-RelB Pathway Reprograms Adipocyte Precursors as Lymph Node Stromal Cells. *Immunity* 37: 721–734.

10. Hall, J. C., K. A. Heel, J. M. Papadimitriou, and C. Platell. 1998. The pathobiology of peritonitis. *Gastroenterology* 114: 185–196.

11. Fedorko, M. E., and J. G. Hirsch. 1971. Studies on transport of macromolecules and small particles across mesothelial cells of the mouse omentum: I. Morphologic aspects. *Exp. Cell Res.* 69: 113–127.

12. Gerber, S. A., V. Y. Rybalko, C. E. Bigelow, A. A. Lugade, T. H. Foster, J. G. Frelinger, and E. M. Lord. 2006. Preferential attachment of peritoneal tumor metastases to omental immune aggregates and possible role of a unique vascular microenvironment in metastatic survival and growth. *Am. J. Pathol.* 169: 1739–1752.

13. Hodel, C. 1970. Ultrastructural studies on the absorption of protein markers by the greater omentum. *Eur. Surg. Res.* 2: 435–449.

14. Avrameas, S., and T. Ternynck. 1995. Natural autoantibodies: The other side of the immune system. *Res. Immunol.* 146: 235–248.

15. Rangel-Moreno, J., J. E. Moyron-Quiroz, D. M. Carragher, K. Kusser, L. Hartson, A. Moquin, and T. D. Randall. 2009. Omental Milky Spots Develop in the Absence of Lymphoid Tissue-Inducer Cells and Support B and T Cell Responses to Peritoneal Antigens. *Immunity* 30: 731–743.

16. Weinstein, J. S., D. C. Nacionales, P. Y. Lee, K. M. Kelly-Scumpia, X.-J. Yan, P. O. Scumpia, D. S. Vale-Cruz, E. Sobel, M. Satoh, N. Chiorazzi, and W. H. Reeves. 2008. Colocalization of Antigen-Specific B and T Cells within Ectopic Lymphoid Tissue following Immunization with Exogenous Antigen. *J. Immunol.* 181: 3259–3267.

17. Bénézech, C., N. T. Luu, J. A. Walker, A. A. Kruglov, Y. Loo, K. Nakamura, Y. Zhang, S. Nayar, L. H. Jones, A. Flores-Langarica, A. McIntosh, J. Marshall, F. Barone, G. Besra, K. Miles, J. E. Allen, M. Gray, G. Kollias, A. F. Cunningham, D. R. Withers, K. M. Toellner, N. D. Jones, M. Veldhoen, S. A. Nedospasov, A. N. J. McKenzie, and J. H. Caamaño. 2015. Inflammation-induced formation of fat-associated lymphoid clusters. *Nat. Immunol.* 16: 819–828.

18. Moro, K., T. Yamada, M. Tanabe, T. Takeuchi, T. Ikawa, H. Kawamoto, J. I. Furusawa, M. Ohtani, H. Fujii, and S. Koyasu. 2010. Innate production of TH 2 cytokines by adipose tissue-associated c-Kit+ Sca-1+ lymphoid cells. *Nature* 463: 540–544.

19. Elewa, Y. H. osn. A., O. Ichii, S. Otsuka, Y. Hashimoto, and Y. Kon. 2014. Characterization of mouse mediastinal fat-associated lymphoid clusters. *Cell Tissue Res.* 357: 731–741.

20. Shi, W., Y. Liao, S. N. Willis, N. Taubenheim, M. Inouye, D. M. Tarlinton, G. K. Smyth, P. D. Hodgkin, S. L. Nutt, and L. M. Corcoran. 2015. Transcriptional profiling of mouse B cell terminal differentiation defines a signature for antibody-secreting plasma cells. *Nat. Immunol.* 16: 663–673.

21. Cyster, J. G., and C. D. C. Allen. 2019. B Cell Responses: Cell Interaction Dynamics and Decisions. *Cell* 177: 524–540.

22. Silva-Cayetano, A., and M. A. Linterman. 2020. Stromal cell control of conventional and ectopic germinal centre reactions. *Curr. Opin. Immunol.* 64: 26–33.

23. Shlomchik, M. J., W. Luo, and F. Weisel. 2019. Linking signaling and selection in the germinal center. *Immunol. Rev.* 288: 49–63.

24. Chaplin, D. D., and Y. X. Fu. 1998. Cytokine regulation of secondary lymphoid organ development. *Curr. Opin. Immunol.* 10: 289–297.

25. Endres, R., M. B. Alimzhanov, T. Plitz, A. Fütterer, M. H. Kosco-Vilbois, S. A. Nedospasov, K. Rajewsky, and K. Pfeffer. 1999. Mature follicular dendritic cell networks depend on expression of lymphotoxin β receptor by radioresistant stromal cells and of lymphotoxin β and tumor necrosis factor by B cells. *J. Exp. Med.* 189: 159–167.

26. Kugler-Umana, O., P. Devarajan, and S. L. Swain. 2020. Understanding the heterogeneous population of age-associated B cells and their contributions to autoimmunity and immune response to pathogens. *Crit. Rev. Immunol.* 40: 297–309.

27. Baba, Y., Y. Saito, and Y. Kotetsu. 2019. Heterogeneous subsets of B-lineage regulatory cells (Breg cells). *Int. Immunol.* 32: 155–162.

28. Hao, Y., P. O'Neill, M. S. Naradikian, J. L. Scholz, and M. P. Cancro. 2011. A B-cell subset uniquely responsive to innate stimuli accumulates in aged mice. *Blood* 118: 1294–1304.

29. Rubtsov, A. V., K. Rubtsova, A. Fischer, R. T. Meehan, J. Z. Gillis, J. W. Kappler, and P. Marrack. 2011. Toll-like receptor 7 (TLR7)-driven accumulation of a novel CD11c^{+} B-cell population is important for the development of autoimmunity. *Blood* 118: 1305–1315.

30. Cancro, M. P. 2020. Age-Associated B Cells. *Annu. Rev. Immunol.* 38: 315–340.

31. Rubtsova, K., A. V. Rubtsov, J. M. Thurman, J. M. Mennona, J. W. Kappler, and P. Marrack. 2017. B cells expressing the transcription factor T-bet drive lupus-like autoimmunity. *J. Clin. Invest.* 127: 1392–1404.

32. Rubtsov, A. V., K. Rubtsova, J. W. Kappler, J. Jacobelli, R. S. Friedman, and P. Marrack. 2015. CD11c-Expressing B Cells Are Located at the T Cell/B Cell Border in Spleen and Are Potent APCs. *J. Immunol.* 195: 71–79.

33. Johnson, J. L., R. L. Rosenthal, J. J. Knox, A. Myles, M. S. Naradikian, J. Madej, M. Kostiv, A. M. Rosenfeld, W. Meng, S. R. Christensen, S. E. Hensley, J. Yewdell, D. H. Canaday, J. Zhu, A. B. McDermott, Y. Dori, M. Itkin, E. J. Wherry, N. Pardi, D. Weissman, A. Naji, E. T. L. Prak, M. R. Betts, and M. P. Cancro. 2020. The Transcription Factor T-bet Resolves Memory B Cell Subsets with Distinct Tissue Distributions and Antibody Specificities in Mice and Humans. *Immunity* 52: 842-855.e6.

34. Clark, R., V. Krishnan, M. Schoof, I. Rodriguez, B. Theriault, M. Chekmareva, and C. Rinker-Schaeffer. 2013. Milky spots promote ovarian cancer metastatic colonization of peritoneal adipose in experimental models. *Am. J. Pathol.* 183: 576–591.

35. Liu, J., X. Geng, and Y. Li. 2016. Milky spots: omental functional units and hotbeds for peritoneal cancer metastasis. *Tumor Biol.* 37: 5715–5726.

36. Kasagi, Y., Y. Harada, Y. Morodomi, T. Iwai, S. Saito, K. Yoshida, E. Oki, H. Saeki, K. Ohgaki, M. Sugiyama, M. Onimaru, Y. Maehara, and Y. Yonemitsu. 2016. Peritoneal dissemination requires an Sp1-dependent CXCR4/CXCL12 signaling axis and extracellular matrix-directed spheroid formation. *Cancer Res.* 76: 347–357.

37. Nowicka, A., F. C. Marini, T. N. Solley, P. B. Elizondo, Y. Zhang, H. J. Sharp, R. Broaddus, M. Kolonin, S. C. Mok, M. S. Thompson, W. A. Woodward, K. Lu, B. Salimian, D. Nagrath, and A. H. Klopp. 2013. Human omental-derived adipose stem cells increase ovarian cancer proliferation, migration, and chemoresistance. *PLoS One* 8.

38. Lee, W. J., S. Y. Ko, M. S. Mohamed, H. A. Kenny, E. Lengyel, and H. Naora. 2019. Neutrophils facilitate ovarian cancer premetastatic niche formation in the omentum. *J. Exp. Med.* 216: 176–194.

39. Karaosmanoglu, D., M. Karcaaltincaba, B. Oguz, D. Akata, M. Özmen, and O. Akhan. 2009. CT findings of lymphoma with peritoneal, omental and mesenteric involvement: Peritoneal lymphomatosis. *Eur. J. Radiol.* 71: 313–317.

40. Cabral, F. C., K. M. Krajewski, K. W. Kim, N. H. Ramaiya, and J. P. Jagannathan. 2013. Peritoneal lymphomatosis: CT and PET/CT findings and how to differentiate between carcinomatosis and sarcomatosis. *Cancer Imaging* 13: 162–170.

41. Kvell, K., T. Czömpöly, L. Hiripi, P. Balogh, J. Kóbor, L. Bodrogi, J. E. Pongrácz, W. A. Ritchie, and Z. Bősze. 2010. Characterisation of eGFP-transgenic BALB/c mouse strain established by lentiviral transgenesis. *Transgenic Res.* 19: 105–112.

42. Choi, I., H. K. Chung, S. Ramu, H. N. Lee, K. E. Kim, S. Lee, J. Yoo, D. Choi, Y. S. Lee, B. Aguilar, and Y. K. Hong. 2011. Visualization of lymphatic vessels by Prox1-promoter directed GFP reporter in a bacterial artificial chromosome-based transgenic mouse. *Blood* 117: 362–365.

43. Nowotschin, S., and A. K. Hadjantonakis. 2009. Use of KikGR a photoconvertible green-to-red fluorescent protein for cell labeling and lineage analysis in ES cells and mouse embryos. *BMC Dev. Biol.* 9.

44. Vojkovics, D., Z. Kellermayer, D. Heidt, M. Mihalj, B. Kajtár, D. Ernszt, T. Kovács, P. Németh, and P. Balogh. 2016. Isolation and Characterization of a Murine Spontaneous High-Grade Follicular Lymphoma with Restricted In Vivo Spreading – a Model for Lymphatic Metastasis Via the Mesentery. *Pathol. Oncol. Res.* 22: 421–430.

45. Strebe, N., F. Breitling, D. Moosmayer, B. Brocks, and S. Dübel. 2010. Cloning of Variable Domains from Mouse Hybridoma by PCR. *Antib. Eng.* 3–14.

46. Alamyar, E., P. Duroux, M. P. Lefranc, and V. Giudicelli. 2012. IMGT® tools for the nucleotide analysis of immunoglobulin (IG) and t cell receptor (TR) V-(D)-J repertoires, polymorphisms, and IG mutations: IMGT/V-QUEST and IMGT/HighV-QUEST for NGS. *Methods Mol. Biol.* 882: 569–604.

47. Zhou, W., H. C. Kang, M. O'Grady, K. M. Chambers, B. Dubbels, P. Melquist, and K. R. Gee. 2016. CellTrace™ Far Red & CellTracker™ Deep Red. *J. Biol. Methods* 3: e38.

48. Chin, S. S., L. Chorro, J. Chan, and G. Lauvau. 2019. Splenic innate B1 B cell plasmablasts produce sustained granulocyte-macrophage colony-stimulating factor and interleukin-3 cytokines during murine malaria infections. *Infect. Immun.* 87.

49. Balogh, P., G. Szekeres, and P. Németh. 1994. Hapten-mediated identification of cell membrane antigens using an anti-FITC monoclonal antibody. *J. Immunol. Methods* 169: 35–40.

50. Kvell, K., T. Czömpöly, T. Pikkarainen, and P. Balogh. 2006. Species-specific restriction of cell surface expression of mouse MARCO glycoprotein in murine cell lines. *Biochem. Biophys. Res. Commun.* 341: 1193–1202.

51. Kolde, R. 2019. Package "pheatmap." .

52. 2021. R Core Team (2017). R: A language and environment for statistical computing. R Foundation for Statistical Computing, Vienna, Austria. .

53. Czömpöly, T., Á. Lábadi, Z. Kellermayer, K. Olasz, H.-H. Arnold, and P. Balogh. 2011. Transcription Factor Nkx2-3 Controls the Vascular Identity and Lymphocyte Homing in the Spleen. *J. Immunol.* 186: 6981–6989.

54. Oberlin, E., A. Amara, F. Bachelerie, C. Bessia, J. L. Virelizier, F. Arenzana- Seisdedos, O. Schwartz, J. M. Heard, I. Clark-Lewis, D. F. Legler, M. Loetscher, M. Baggiolini, and B. Moser. 1996. The CXC chemokine SDF-1 is the ligand for LESTR/fusin and prevents infection by T-cell-line-adapted HIV-1. *Nature* 382: 833–835.

55. Burns, J. M., B. C. Summers, Y. Wang, A. Melikian, R. Berahovich, Z. Miao, M. E. T. Penfold, M. J. Sunshine, D. R. Littman, C. J. Kuo, K. Wei, B. E. McMaster, K. Wright, M. C. Howard, and T. J. Schall. 2006. A novel chemokine receptor for SDF-1 and I-TAC involved in cell survival, cell adhesion, and tumor development. *J. Exp. Med.* 203: 2201–2213.

56. Merad, M., P. Sathe, J. Helft, J. Miller, and A. Mortha. 2013. The dendritic cell lineage: Ontogeny and function of dendritic cells and their subsets in the steady state and the inflamed setting. *Annu. Rev. Immunol.* 31: 563–604.

57. Hao, Y., P. O'Neill, M. S. Naradikian, J. L. Scholz, and M. P. Cancro. 2011. A B-cell subset uniquely responsive to innate stimuli accumulates in aged mice. *Blood* 118: 1294–1304.

58. Pelletier, M., J. S. Thompson, F. Qian, S. A. Bixler, D. Gong, T. Cachero, K. Gilbride, E. Day, M. Zafari, C. Benjamin, L. Gorelik, A. Whitty, S. L. Kaled, C. Ambrose, and Y. M. Hsu. 2003. Comparison of soluble decoy IgG fusion proteins of BAFF-R and BCMA as antagonists for BAFF. *J. Biol. Chem.* 278: 33127–33133.

59. Farr, A. G., M. L. Berry, A. Kim, A. J. Nelson, M. P. Welch, and A. Aruffo. 1992. Characterization and cloning of a novel glycoprotein expressed by stromal cells in t-dependent areas of peripheral lymphoid tissues. *J. Exp. Med.* 176: 1477–1482.

60. Hertzler, A. E. 1926. THE OMENTUM. *J. Am. Med. Assoc.* 86: 1785–1785.

61. Jia, X., F. Gábris, Ó. Jacobsen, G. Bedics, B. Botz, Z. Helyes, Z. Kellermayer, D. Vojkovics, G. Berta, N. Nagy, Z. Jakus, and P. Balogh. 2020. Foliate Lymphoid Aggregates as Novel Forms of Serous Lymphocyte Entry Sites of Peritoneal B Cells and High-Grade B Cell Lymphomas. *J. Immunol.* 204: 23–36.

62. Zhang, W., H. Zhang, S. Liu, F. Xia, Z. Kang, Y. Zhang, Y. Liu, H. Xiao, L. Chen, C. Huang, N. Shen, H. Xu, and F. Li. 2019. Excessive CD11c+Tbet+ B cells promote aberrant TFH differentiation and affinity-based germinal center selection in lupus. *Proc. Natl. Acad. Sci. U. S. A.* 116: 18550–18560.

63. Hochweller, K., J. Striegler, G. J. Hämmerling, and N. Garbi. 2008. A novel CD11c.DTR transgenic mouse for depletion of dendritic cells reveals their requirement for homeostatic proliferation of natural killer cells. *Eur. J. Immunol.* 38: 2776–2783.

Acknowledgement

Foliate Lymphoid Aggregates as Novel Forms of Serous Lymphocyte Entry Sites of Peritoneal B Cells and High-Grade B Cell Lymphomas

Xinkai Jia,* Fanni Gábris,* Óli Jacobsen,* Gábor Bedics,* Bálint Botz,[†,‡,§] Zsuzsanna Helyes,[†,‡] Zoltán Kellermayer,*,[¶] Dóra Vojkovics,*,[¶] Gergely Berta,[‖] Nándor Nagy,[#] Zoltán Jakus,**,[††] and Péter Balogh*,[¶]

The cellular homeostasis of lymphoid tissues is determined by the continuous interactions of mobile hematopoietic cells within specialized microenvironments created by sessile stromal cells. In contrast to the lymph nodes and mucosal lymphoid tissues with well-defined entry and exit routes, the movement of leukocytes in the peritoneal cavity is largely unknown. In this study, we report that, in addition to the omental milky spots and fat-associated lymphoid clusters, in mice, the serous surface of the mesenteric adipose streaks contains lymphocyte-rich organoids comprised of a highly compacted leaf-like part connected to the adipose tissue that can also efficiently bind B cells and high-grade B cell lymphoma (diffuse large B cell lymphoma) cells. Denoted as foliate lymphoid aggregates (FLAgs), these structures show incomplete T/B segregation and a partially differentiated stromal architecture. LYVE-1–positive macrophages covering FLAgs efficiently bind i.p. injected normal B cells as well as different types of diffuse large B cell lymphoma cells. Within FLAgs, the lymphocytes compartmentalize according to their chemokine receptor pattern and subsequently migrate toward the mesenteric lymph nodes via the mesenteric lymphatic capillaries. The blood supply of FLAgs includes short vascular segments displaying peripheral lymph node addressin, and the extravasation of lymphocytes to the omental and mesenteric adipose tissues is partly mediated by L-selectin. The appearance of i.p. injected cells in mesenteric lymph nodes suggests that the mesentery-associated lymphatics may also collect leukocytes from the fat-associated lymphoid clusters and FLAgs, thus combining the mucosal and serous exit of mobile leukocytes and increasing the range of drainage sites for the peritoneal expansion of lymphoid malignancies. *The Journal of Immunology*, 2020, 204: 000–000.

The omentum and mesentery are primarily adipose tissues associated with the gastrointestinal organs, harboring an unusual type of peripheral lymphoid tissues (1, 2). Although the leukocytes dwelling in these serous tissues constitute a distinct immunological compartment, they are fully integrated components of systemic immunity, including their extensive traffic to structured peripheral lymphoid organs during activation and differentiation (3, 4). In addition, the specific significance of omental protection during i.p. inflammations or in perforating abdominal injuries has long been recognized and appreciated (5). Although both the peritoneal and pleural cavities are important reservoirs for B1 B lymphocytes, the tissue characteristics of a local specialized microenvironment that allows the survival and interaction within serous lymphoid organs during immune responses and as peritoneal tumor dissemination sites have only recently been investigated in more detail (6).

*Department of Immunology and Biotechnology, Clinical Center, University of Pécs, 7643 Pécs, Hungary; †Department of Pharmacology and Pharmacotherapy, Medical School, University of Pécs, 7624 Pécs, Hungary; ‡Molecular Pharmacology Research Group, Szentágothai Research Center, University of Pécs, 7624 Pécs, Hungary; §Department of Radiology, Clinical Center, University of Pécs, 7624 Pécs, Hungary; ¶Lymphoid Organogenesis Research Group, Szentágothai Research Center, University of Pécs, 7624 Pécs, Hungary; ‖Department of Medical Biology and Central Electron Microscope Laboratory, Medical School, University of Pécs, 7643 Pécs, Hungary; #Department of Anatomy, Histology and Embryology, Semmelweis University, 1085 Budapest, Hungary; **MTA-SE Lendulet Lymphatic Physiology Research Group of the Hungarian Academy of Sciences and Semmelweis University, 1094 Budapest, Hungary; and ††Department of Physiology, Semmelweis University, 1094 Budapest, Hungary

ORCIDs: 0000-0003-1767-3642 (O.J.); 0000-0003-4628-2384 (G.B.); 0000-0001-9560-6424 (Z.K.); 0000-0003-3388-0019 (D.V.); 0000-0002-6223-5214 (N.N.); 0000-0002-6304-2369 (Z.J.).

Received for publication July 19, 2019. Accepted for publication October 25, 2019.

This work was supported by Hungarian Science Foundation National Research, Development and Innovation Office Grants 128322 (P.B.) and GINOP-2.3.2-15-2016-00022. N.N. was supported by Hungarian Science Foundation NKFI Grant 124740. Z.K. was supported by the ÚNKP-17-4-I-PTE-83 New National Excellence Program of the Ministry of Human Capacities of Hungary and the postdoctoral research grant of the Faculty of Medicine, University of Pécs. B.B. was supported by the János Bolyai Research Scholarship of the Hungarian Academy of Sciences and the ÚNKP-19-4-P-PTE-458 New National Excellence Program of the Ministry for Innovation and Technology. Z.H. was supported by University of Pécs projects GINOP-2.3.2-15-2016-00048 (Stay Alive)

Address correspondence and reprint requests to Dr. Péter Balogh, Department of Immunology and Biotechnology, Clinical Center, University of Pécs, Szigeti út 12, H-7643 Pécs, Hungary. E-mail address: balogh.peter@pte.hu

The online version of this article contains supplemental material.

Abbreviations used in this article: CTFR, CellTrace Far Red; DAB, diaminobenzidine; DLBCL, diffuse large B cell lymphoma; ECM, extracellular matrix; FALC, fat-associated lymphoid cluster; FLAg, foliate lymphoid aggregate; Fn, fibronectin; FSC, forward light scatter; HEV, high endothelial venule; ILC2, type 2 innate lymphoid cell; LEC, lymphatic endothelial cell; mLN, mesenteric lymph node; MS, milky spots; NIR, near-infrared; PEC, peritoneal exudate cell; pLN, peripheral lymph node; PNAd, pLN addressin; SSC, side light scatter.

As prototypic serous lymphoid organoids, the milky spots (MS) of the omentum were described first. In mice, MS are formed by the clustering of macrophages, dominantly B cells and, to a lesser extent, T cells, without compartmentalization into separate T and B cell zones characteristic of secondary lymphoid tissues (7). MS also function as lymphocyte exit ports from the systemic circulation (8).

More recently, similar leukocyte-rich gatherings (denoted as fat-associated lymphoid clusters [FALCs]) have been identified in the perivascular adipose tissue of mesentery (Supplemental Fig. 1). Regarding their functions, FALCs contain type 2 innate lymphoid cells (ILC2), capable of producing IL-5 and IL-13 in allergic reactions and during protection against helminth infections (9). In FALCs within the mediastinal adipose tissue, the activity of local ILC2 cells can be enhanced by resident stromal cells producing IL-33, leading to protective IgM production by B1 cells (10). Furthermore, omental MS may sustain B cell expansion, leading to germinal center formation coupled with affinity maturation and isotype switch, although without demonstrable follicular dendritic cell meshwork present in peripheral lymphoid organs (7). Similarly to peripheral lymph nodes (pLNs), CXCL13 is a critical chemokine required for B cell entry as well as FALC/MS formation and expansion; however, in contrast to other secondary lymphoid organs, FALC development occurs independently from lymphoid tissue inducer or subsets of ILC3 and LTβR engagement. In contrast, macrophage-derived TNF as well as nonlymphoid tissue inducer/ILC3–type innate lymphoid cells and commensal bacteria are necessary for the appearance of FALCs (9, 10).

These findings indicate that, although intra-abdominal fat-associated lymphoid tissues are anatomically separate and developmentally different from other peripheral lymphoid organs, they, nevertheless, contribute to the systemic immunity, including lymphocyte traffic and distribution. Importantly, their lymphocyte turnover mechanisms and kinetics have only been partially explored, including the access via blood vasculature or lymphatic circulation or migratory routes (11, 12).

In addition to leukocytes, the serous expansion of cancer cells, including colonic, gastric, and ovary tumors, also affects specific regions within the mesentery, in which local chemotactic as well as extracellular matrix (ECM) components may play important roles, including CXCR4/CXCL12 interactions and peritoneal collagen IV and fibronectin (Fn) (6, 13). Further propagation of metastasis may involve dissemination via lymphatic vessels situated within the mesenteric adipose streaks; however, the exact relationship between the cellular entry sites and lymphatic drainage remains to be determined. In addition to these cancers, expansion of high-grade extranodal B cell lymphomas may also lead to peritoneal lymphomatosis and serous effusions causing poor prognosis (14, 15).

In our previous work on a spontaneous mouse high-grade B cell lymphoma, we found a rapid dissemination toward the mesenteric lymph nodes (mLNs) coupled with the lymphomatous transformation of mesentery together with the accumulation of lymphoma cells within the mesenteric lymphatics (16). In the current study, we first investigated the i.p. lymphoma-binding sites of the serous membrane of abdominal cavity, allowing the identification and detailed characterization of a hitherto undescribed variant of serous lymphoid tissues that can efficiently bind i.p. lymphoma cells and normal lymphocytes. Owing to the leaf-like appearance of their main part, connected to omental and mesenteric adipose tissues or peritoneal membrane via a stalk, we chose to denote these structures as foliate lymphoid aggregates (FLAgs). These organoids possess partial lymphoid compartmentalization, which

also influences the tissue distribution of high-grade B cell lymphoma subsets, corresponding to the confinement of local homeostatic chemokine dominance. Furthermore, we demonstrate that the removal of LYVE-1–positive macrophages reduces lymphoma cell binding. Finally, we provide evidence that FLAgs can also be destination sites for blood-borne leukocytes via pLN addressin (PNAd)–positive high endothelial venules (HEVs) with the partial use of L-selectin for homing.

Materials and Methods

Mice

Inbred BALB/c, C57BL/6J, and BALB/c^{eGFP}-transgenic mice (17) were maintained at the specific pathogen-free animal facility of the Department of Immunology and Biotechnology. *Prox1*-GFP BAC lymphatic reporter–transgenic mice (18) obtained from the Mutant Mouse Regional Resource Center were maintained in heterozygous form and were used for breeding (*Prox1*-GFP C57BL/6J crossed with BALB/c) F1 mice as recipients for short-term homing. KikGR mice (19) on C57BL/6J background were obtained from The Jackson Laboratory and were backcrossed through 10 generations onto BALB/c background. All procedures involving live animals were carried out in accordance with the guidelines set out by the Ethics Committee on Animal Experimentation (University of Pécs, Hungary) under license number BA02/2000-16/2015, with approval for the use of genetically modified organisms under license number SF/27-1/2014 issued by the Ministry of Rural Development, Hungary.

Abs and reagents

For flow cytometry rat mAbs against mouse, CD5 (YTS121.5), CD19 (1D3), MHC class II (IBL-5/22), CD21 (7G6), CD23 (B3B4), LFA-1/CD11a/CD18 (M17.7 and IBL-6/2), MAC-1/CD11b/CD18 (M1/70), CD45 (IBL-3/16), B220/CD45R (RA3-6B2), IgM (B7.6), Thy-1/CD90 (IBL-1), ICAM-1/CD54 (YN1/1), MAdCAM-1 (MECA-367), VCAM-1/CD106 (M/K-2.7), and L-selectin/CD62L (MEL-14) were used as hybridoma supernatants. Rat mAb against mouse CD138 (281-2) and PE-conjugated rat mAb against mouse CXCR5 (2G8) were obtained from BD Biosciences (Diagon, Budapest, Hungary) and biotinylated anti-CCR7 mAb (4B12) from BioLegend (Biomedica Hungaria, Budapest, Hungary), the latter detected with streptavidin–PE/Cy5 conjugate (from BD Biosciences). Rat mAb against mouse LYVE-1 (223322) Ag and goat polyclonal Abs against mouse CCL21 and CXCL13 were purchased from Bio-Techne (R&D Systems, Diagon, Budapest, Hungary), FITC-conjugated donkey anti-goat Abs and HRP-conjugated sheep anti-FITC Abs were purchased from SouthernBiotech (Bio-Kasztel, Budapest, Hungary). For immunohistochemistry, rat mAbs were detected using ImmPRESS goat anti-rat IgG-HRP polymeric conjugate (Vector Laboratories, BioMarker, Gödöllő, Hungary). Rabbit anti-Fn and tetramethylrhodamine-labeled goat anti-rabbit polyclonal Abs were purchased from Abcam (Bio-Kasztel, Budapest, Hungary). Chemicals for buffers and histochemical substrates were purchased from Sigma-Aldrich.

Flow cytometry

For the labeling of CXCR5 and CCR7 A20 and Bc.DLFL1, lymphoma cells were incubated with biotinylated or PE-conjugated mAbs against chemokine receptors in mixture with anti-B220 mAb conjugated with Alexa Fluor 647 (prepared at the Department of Immunology and Biotechnology) at room temperature, followed by washing. After further incubation with streptavidin–PE/Cy5 conjugate, the samples were washed and fixed in 1% buffered paraformaldehyde. For other cell surface markers, the lymphoma cells were incubated on ice with rat mAbs listed above, followed by washing and incubation with goat anti-rat IgG FITC conjugate. After fixation, 10,000 events gated on forward light scatter (FSC)/side light scatter (SSC) parameters and B220 reactivity, or KikGR expression combined with CD45 expression, were collected and analyzed using BD FACSCalibur and CellQuest Pro software package.

Whole-mount immunofluorescence and immunohistochemistry

After the removal of the entire gut complex from esophagus until the upper third of rectum, the gut was placed in a petri dish, with its folds arranged, and fixed in 4% buffered paraformaldehyde for 10 min. After rinsing in PBS, a short hematoxylin staining was performed, followed by rinsing in tap water. Either the whole omentum or the mesentery or some selected regions were isolated under stereomicroscopic dissection. For immunofluorescence, the samples were rinsed in PBS containing 0.1% saponin, followed by incubation in PBS containing 0.1% saponin and 5% BSA for 1 h.

The samples were incubated with FITC anti-IgM, TAMRA anti–Thy-1 or Alexa Fluor 647 anti-CD45 mAbs overnight, followed by extensive washing in PBS containing 0.1% saponin and 0.1% BSA. For indirect immunofluorescence FITC or PE-conjugated anti-rat, anti-goat, or anti-rabbit secondary Abs (adsorbed for mouse IgG) were added and incubated overnight, followed by extensive washing for at least 6 h. Confocal fluorescence images were taken using an Olympus FluoView FV1000 laser scanning confocal imaging system (Olympus Europa SE & Co., Hamburg, Germany).

For immunohistochemistry, the tissue samples were incubated in 2 mg/ml phenylhydrazine hydrochloride in PBS containing 0.1% saponin to quench endogenous peroxidase activity, followed by extensive washing. The tissues were blocked with a 1:1 mixture of 20% normal goat serum and 5% BSA for 1 h, followed by the addition of rat mAbs in the presence of 5% DMSO. For detecting CFSE-labeled lymphoma cells, HRP-conjugated sheep anti-FITC Abs were used. The samples were incubated overnight with continuous agitation, followed by washing in PBS–0.1% saponin. The bound rat Abs were detected using goat anti-rat IgG-HRP conjugate following overnight incubation and were visualized using diaminobenzidine (DAB)–H_2O_2 (Dako, Kromat, Budapest, Hungary). After mounting, the sections were viewed under an Olympus BX61 microscope. The acquisition of digital pictures with a charge-coupled device camera was performed using the ZEN software; the pictures were processed using Adobe Photoshop 6.0 with adjustments for brightness contrast and color balance applied for the entire images.

Transmission electron microscopy

Dissected mouse intestines and harvested FLAgs were fixed overnight at 4°C with 4% buffered paraformaldehyde, washed in PBS, and postfixed with 2% glutaraldehyde, followed by dehydration in graded ethanol. Tissue samples were treated with 1% osmium tetroxide (Polysciences, Warrington, PA) for 2 h and embedded in a Polybed/Araldite 6500 mixture (Polysciences). The 1-μm-thick semithin sections were stained with toluidine blue. The ultrathin sections were contrasted with uranyl acetate and lead citrate and studied with a Hitachi Electron microscope type H-7600.

Cell labeling and transfer

A20 cells were cultured in RPMI 1640 (Sigma-Aldrich) supplemented with 10% heat-inactivated FBS (EuroClone, Biocenter, Szeged, Hungary) and transduced using replication-defective retroviral vectors containing the bacterial gene for β-galactosidase (LacZ) using the supernatant of PA317 packaging cells (kindly provided by Dr. C. L. Cepko) followed by G418 selection (0.5 mg/ml final concentration; Sigma-Aldrich). LacZ detection was performed using standard X-gal (Sigma-Aldrich) staining. Bc.DLFL1 cells (16) were maintained as serial i.p. passage, where the lymphoma cells were collected from the tumor-laden mLNs. For tracing, the injected cells were either labeled with 5 μM CFSE (Thermo Fisher Scientific, Life Technologies, Budapest, Hungary) as recommended, or with 10 μM CellTrace Far Red (CTFR) (20) kindly provided by Dr. K. R. Gee, Thermo Fisher Scientific, Eugene, OR). Normal peritoneal B cells were purified from BALB/c mice using FITC-labeled anti-B220 and anti-FITC beads, followed by separation on VarioMACS (Miltenyi Biotec). For near-infrared (NIR) fluorescence bioimaging of MACS-purified B cells or lymphoma cells, we used lipophilic XenoLight DiR dye (PerkinElmer) as recommended by the vendor. After labeling, the cells were washed in RPMI 1640 basal medium and were injected i.p. at 2×10^6 cells per recipient dosage.

NIR fluorescence imaging

MACS-purified B cells or lymphoma cells (A20 or Bc.DLFL1) were labeled with XenoLight DiR dye, followed by i.p. injection. The fluorescence in the excised gut samples was measured using the IVIS Lumina III (PerkinElmer, Waltham MA) in vivo imaging system with the following parameters: autoacquisition time, F/stop = 1, Binning = 2, excitation: 740 nm, and emission filter: 790 nm. The tissue binding of Bc.DLFL1 lymphoma cells was quantified by NIR analysis of microdissected serous lymphoid organoids placed in Greiner Bio-One CELLSTAR plate after the hematoxylin staining of 4% paraformaldehyde–fixed omentum and mesentery of mice previously injected i.p. with XenoLight DiR–labeled lymphoma cells. The data were processed and analyzed using Living Image software (PerkinElmer) by displaying the fluorescence intensity using the total radiant efficiency ([photons per second per square centimeter per steradian]/[microwatt per square centimeter]) as a pseudocolor overlay image.

KikGR photoconversion and competitive homing

KikGR photoconversion of lymph nodes was performed by placing whole inguinal lymph nodes in a drop of sterile PBS, followed by exposure to a custom-made illumination device (Optics Engineering, Budapest, Hungary) through 6-mm-diameter fiber optics using indium gallium nitride–based 410-nm chip light-emitting diode (no. APGC1 410, 125 mW) for 2×5 min from two sides at room temperature. After the mechanical release of lymphocytes, KikR cells were placed on ice, whereas lymphocytes from unconverted (KikG) lymph nodes were incubated with 10 μg/ml anti–L-selectin/CD62L mAb MEL-14 (21). After incubation, the lymphocytes were washed and resuspended at 1:1 KikG/KikR ratio (with the final donor cell mixture verified by flow cytometry) and were injected in the tail vein in BALB/c recipients at 5×10^7 total cells per recipient in 250 μl volume. The degree of inhibition was determined by the KikG/KiR ratio following anti-CD45 labeling, corrected with the KikG/KikR ratio of donor cell mixture.

Quantitative RT-PCR

Total RNA from inguinal lymph node, omentum, and mesentery homogenates was isolated using NucleoSpin RNA (Macherey-Nagel). Purity and concentration of RNA was analyzed by NanoDrop. cDNA was synthesized using High-Capacity cDNA Reverse Transcription Kit (Life Technologies). RT-PCR was run on an Applied Biosystems PRISM 7500 machine in duplicates using previously described SYBR Green primers for PNAd core proteins and glycosylation enzymes, creating the MECA-79 epitope (22). Results are shown as fold change of target gene relative to the β-actin housekeeping gene mRNA level, defining the relative value pLN as 1.

Statistical analysis

Data analysis was performed using SPSS 22.0 (IBM). Normality of data distribution was assessed by Shapiro–Wilks test. A t test or Mann–Whitney U test was employed to compare two groups with normally distributed and nonnormally distributed data, respectively. Data are represented as mean ± SEM. A p value < 0.05 was considered statistically significant.

Results

Selective binding of high-grade B cells lymphoma reveals preferential homing sites of the serosa for malignant and normal B cells

Our previous study of the spontaneous extrafollicular high-grade B cell lymphoma Bc.DLFL1 in BALB/c mice revealed spreading via the lymphatic capillaries embedded in the perivascular fat pads of the mesentery and subsequent expansion restricted to mLNs and spleen (16). As this condition represented an advanced stage of disease, we aimed at studying the early steps of lymphoma expansion. Therefore, we first investigated the initial adhesion site of the serous surface, followed by the lymphatic propagation and eventual expansion along the perivascular fat. Four hours after i.p. injection of XenoLight DiR–labeled lymphoma cells followed by NIR fluorescence detection, transabdominal imaging revealed three main positive regions, seemingly corresponding to the mLNs and spleen as main target tissues for Bc.DLFL1 seeding in addition to the injection site. However, after opening up the abdomen, we observed that the omentum was the major dominant fluorescent signal-emitting site, together with a series of small foci arranged in a bead-like pattern along the edge of mesenteric fat streaks connected to the middle segment of small intestine, whereas the mLNs and the spleen were label-free (Fig. 1A–F).

Although the focal pattern of lymphoma accumulation within mesenteric fat and the omentum suggested specific tissue-binding pattern to exclude potential labeling artifacts because of the accumulation of lipophilic dye–tagged lymphoma cells in an adipose tissue environment, we performed a similar short-term transfer experiment using CFSE-labeled cells, followed by anti-FITC whole-mount hapten immunohistochemistry. This approach allows light-microscopical inspection over a wide range of magnification of the entire gastrointestinal tract while eliminating high-level autofluorescence of intestines related to alimentary compounds typically emitting at fluorescein spectrum (23). Using anti-FITC–PO immunohistochemical detection, we observed
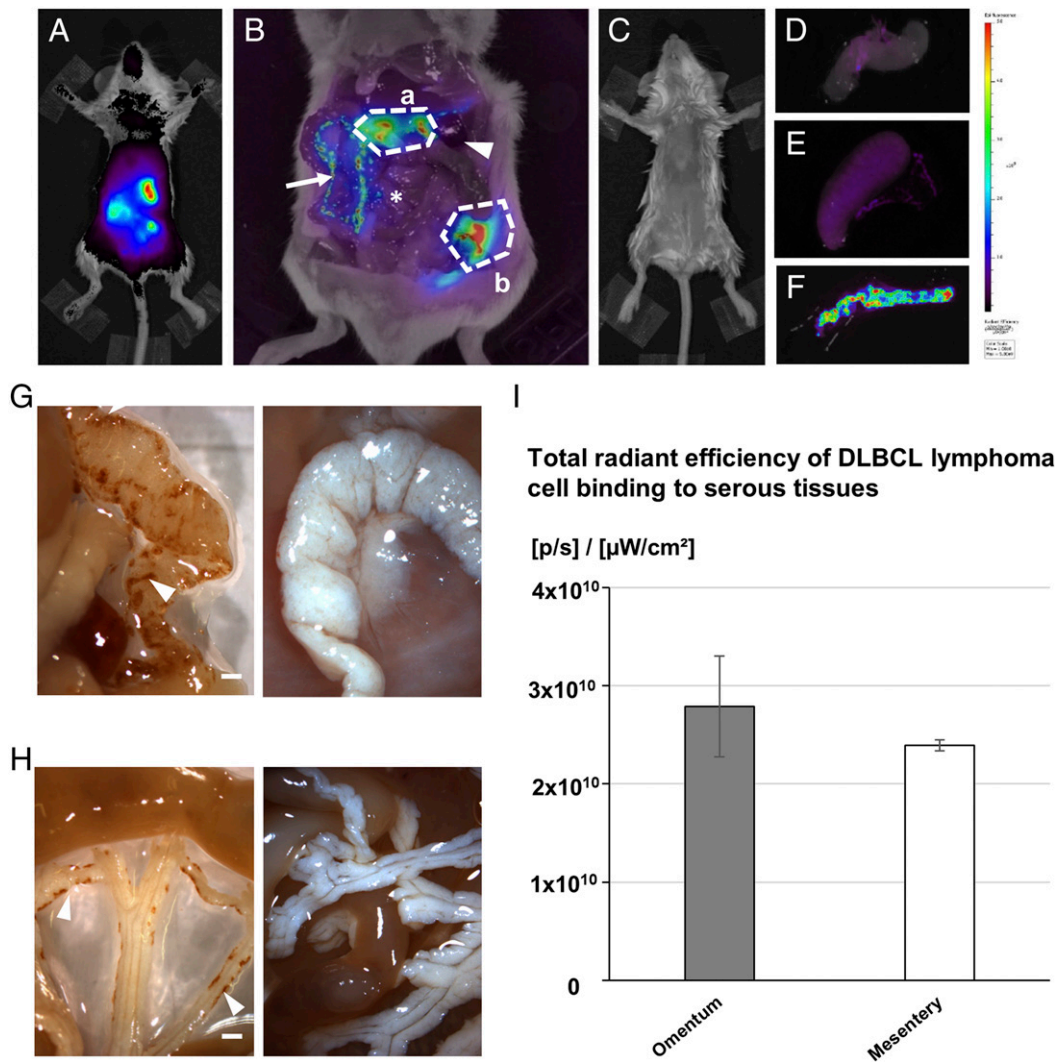
FIGURE 1. In vivo bioimaging of early lymphoma adherence to the peritoneum. (**A**) Transabdominal imaging with three diffusely labeled areas 4 h after injection of XenoLight DiR–labeled Bc.DLFL1 cells; (**B**) several gut-associated bead-like accumulations of lymphoma cells are distinguishable along the mesentery (arrow) and in the omentum (indicated with polygon "a"). Polygon "b" indicates the injection site at the left abdominal region. Note the absence of fluorescence signal in the mLNs (labeled with "*") and spleen (labeled with arrowhead). (**C**) Uninjected sample for imaging setting. (**D**) Ex vivo separated mLN or spleen (**E**) are devoid of detectable signal, while omentum (**F**) shows robust signal emission (representative of three mice). (**G**) Whole-mount immunohistochemical detection of omental clustering of CFSE-labeled Bc.DLFL1 lymphoma cells using anti-FITC–PO detection resulting in brown precipitate (left) 4 h after injection (arrowheads) compared with uninjected control (right). (**H**) Mesenteric adipose tissue stained with anti-FITC–PO resulting in brown precipitate for CFSE-labeled Bc.DLFL1 lymphoma cells (arrowheads) arranged in a chain (left) compared with uninjected sample (right) after anti-FITC immunohistochemistry. Scale bars, 1 mm. (**I**) Quantitation of XenoLight DiR–labeled Bc.DLFL1 lymphoma binding to omentum and mesentery by total radiant efficiency (n = 6 mice per group).

a distribution pattern of CFSE-marked lymphoma cells similar to NIR imaging (Fig. 1G, 1H). Quantitative comparison of omental and mesentery-associated XenoLight DiR fluorescence signal emission indicated that although the individual lymphoma-binding sites are relatively small, their total lymphoma-binding capacity equals that of the omentum (Fig. 1I).

To test whether normal B cells also display similar selective homing sites to the serous surface, MACS-purified peritoneal B cells were labeled with XenoLight DiR dye, and their location was investigated using NIR imaging. We found that, similarly to the distribution of Bc.DLFL1 cells, several B cell foci alongside the mesentery were present 4 h after the injection, in addition to the robust omental localization of peritoneal B cells (Fig. 2A). Interestingly, the quantitative analysis revealed that, compared with the similar diffuse large B cell lymphoma (DLBCL) retention by omentum and mesentery, the capacity of the entire mesentery for the uptake of normal peritoneal exudate cell

(PEC) B cells was significantly higher than that of the omentum (Fig. 2B).

To further investigate the adherence kinetics of lymphocytes to the serous tissues in comparison with the entry into mLNs, we next injected normal BALB/c mice i.p. with lymphocytes isolated from enhanced GFP–reporter mice, followed by their detection in the omentum, mesentery, and mLNs and in the PEC pool at 2, 6, 24, and 48 h after injection. We found that the frequency of residual donor cells in PEC compartment continuously decreased after 6 h. In mLNs, the increase of GFP-positive cells' frequency was first observed at 24 h, and it was maintained until 48 h. Interestingly, we observed a significant reduction after 24 h in the mesentery, whereas in the omentum, the donor cell frequency remained stable until 48 h (Fig. 2C).

These findings establish that, in addition to the omentum, the perivascular adipose streaks of mesentery contain specialized sites that can bind both normal B lymphocytes and high-grade B cell
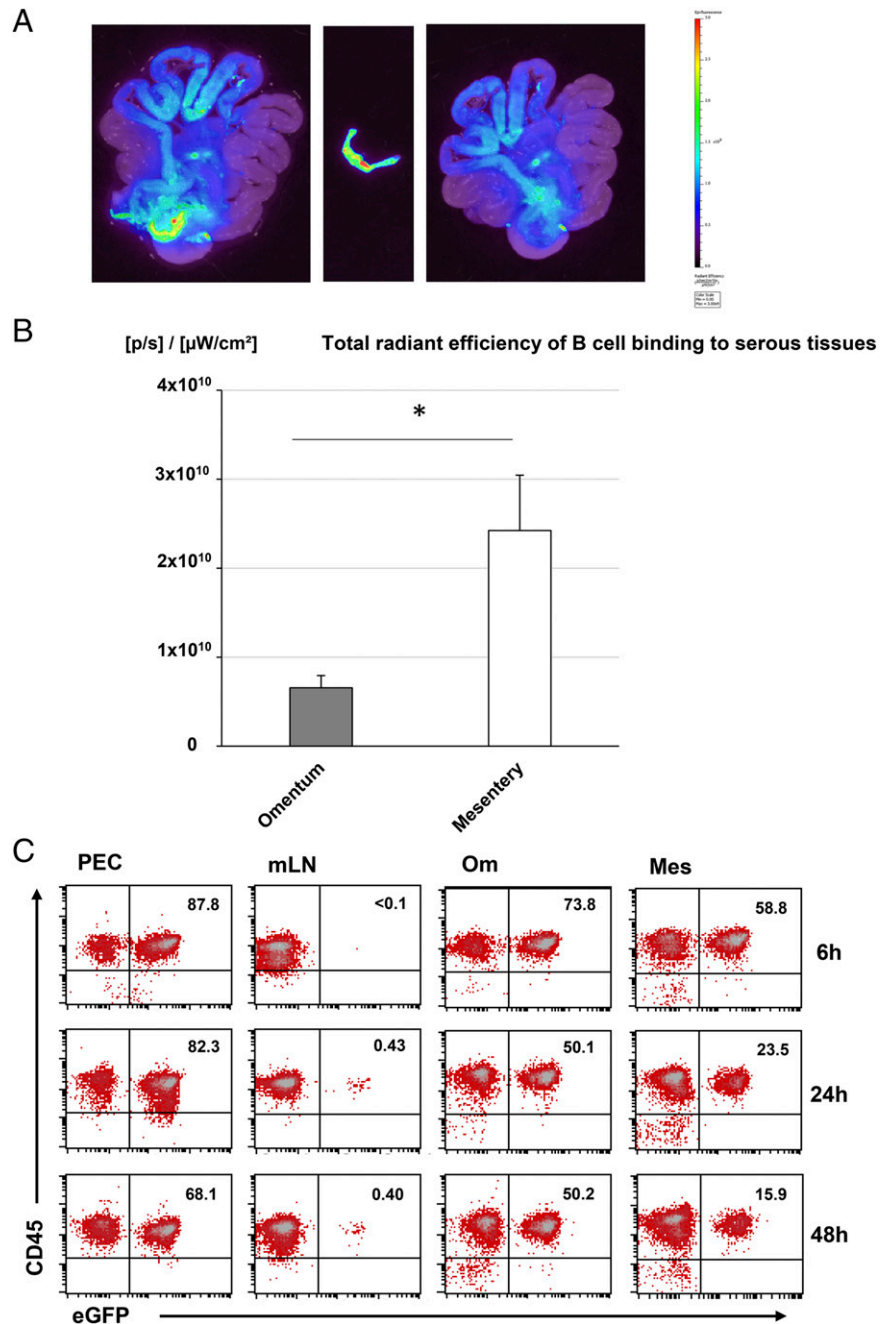
FIGURE 2. Serous accumulation of B cells after i.p. injection. (**A**) Accumulation of Xeno-Light DiR–labeled and MACS-purified B cells 4 h after injection, detected NIR fluorescence imaging in the whole gut–spleen–omentum (Om) complex (left); isolated Om (middle) and residual gut-spleen complex (right) compared with the intensity range (colored bar reference). Representative sample (*n* = 5 mice per group) repeated twice. (**B**) Quantitation of the binding of XenoLight DiR–labeled B cells to Om and mesentery (Mes) by total radiant efficiency (*n* = 6 mice per group). *p < 0.05. (**C**) Kinetics of the distribution of lymphocytes from GFP–transgenic BALB/c donors in wild-type recipients in the PEC, mLNs, Om, and Mes at the time points indicated on the right (gated on size/granularity) using CD45/GFP detection by flow cytometry. Numbers indicate the frequency of gated cells in the upper-right quadrant (representative sample from *n* = 6 mice per group).

lymphoma cells. We found, in this study, that the transit time for the bulk of lymphocytes entering and departing the serous lymphoid tissues is between 6 and 48 h, with a delayed departure from the omentum compared with the mesentery within this period.

Structurally distinguishable types of serous lymphoid organoids with different lymphoma-binding characteristics

To characterize the mesenteric lymphocyte–binding regions, we next removed the whole gut–omentum–mesentery complex and stained it with hematoxylin, combined with lymphoma tracing. We found leaf-like formations, connected to the mesenteric adipose tissue either directly or via a slender stalk (Fig. 3A, 3B), both types showing robust uptake of Bc.DLFL1 cells (Fig. 3C). In addition, similar formations were also observed in the membrane lining of the omental bursa, appearing in paired or, less frequently, in single arrangement (Fig. 3D–F). Owing to their particular appearance, we denote these formations as FLAgs. Their dimensions

were in the range of 250–450-μm length from base to tip, 150–250-μm width, and 30–80-μm thickness, respectively. The most typical location for FLAgs were the omental bursa, but in the omentum and in the mesenteric fat streaks, ~5–15% of lymphoma-binding foci also comprised adipose-associated FLAgs in young adult mice (6–10 wk of age). Furthermore, several distinct leukocyte-rich FALCs and crescent-shaped protrusions (Fig. 3B), both capable of DLBCL binding (Fig. 3C), were also present in both the omentum and mesentery, in addition to the FLAgs.

To compare the lymphoma-binding efficiencies of the FLAgs with FALCs and protrusions, next, we performed a quantitative measurement using XenoLight DiR fluorescence. Hematoxylin staining revealed that FLAgs and protrusions represent more condensed leukocyte clustering compared with FALCs and omental MS located on the adipose surface with less-defined boundaries. Moreover, protrusions connect with broader attachment area to the underlying adipose base and lack identifiable stalks, thus allowing
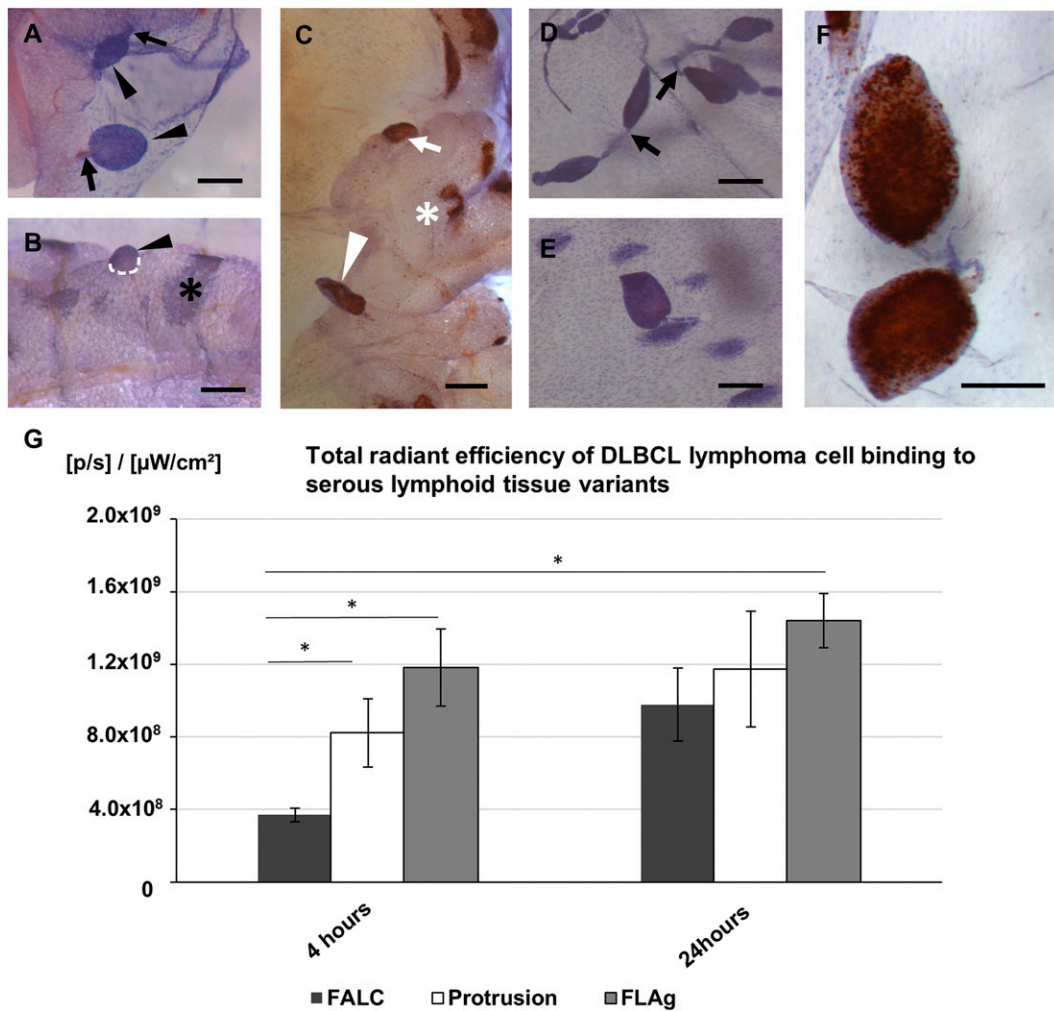
FIGURE 3. Appearance of lymphoma-binding serous lymphoid organoids. (**A**) Hematoxylin-stained single FLAgs (arrowhead) connected to mesenteric fat via slender stalks (labeled with arrows). (**B**) Omental lymphoid formations also include crescent-shaped protrusion (labeled with arrowhead) and diffuse MS (labeled with "*"; hematoxylin stain). Note the extended perimeter of the base (dotted line) of a typical protrusion connecting to the adipose tissue and the absence of stalk. (**C**) CFSE-labeled Bc.DLFL1 cells attach to mesenteric FLAgs (arrowhead), FALCs (*) and protrusion (arrow), visualized by brown anti-FITC–PO staining. (**D**) In the bursal membrane, the FLAgs typically occur in paired arrangement attached to the two sides of the peritoneum through slender stalks (indicated with arrows). (**E**) A solitary FLAg attached to the bursal peritoneum. (**F**) Bursal FLAgs efficiently bind CFSE-labeled Bc.DLFL1 cells 4 h after i.p. injection (anti-FITC–PO staining, brown). Scale bars, 200 μm. (**G**) Quantitation of XenoLight DiR–labeled Bc.DLFL1 lymphoma binding to serous lymphoid tissue types, as indicated by total radiant efficiency ($n = 6$ mice per group). *$p < 0.05$.

the microdissection of these different omental and mesenteric adipose lymphoid tissues after i.p. injection of XenoLight DiR–labeled Bc.DLFL1 cells. We observed the highest fluorescence signal in FLAgs (and with FALCs generating the lowest signal) at both the 4- and 24-h time points. In contrast, FALCs showed a marked increase of lymphoma binding by 24 h, whereas in FLAgs, the increase was less pronounced (Fig. 3G).

To determine whether these FLAgs occur only in BALB/c mice as a strain-specific trait, we also inspected C57BL/6J mice as a standard mouse strain used in immunological studies. We found in our C57BL/6J specific pathogen-free colony a similar occurrence of FLAgs in mice older than 8–10 wk. Their number is variable, usually in the range of 10–30 per mouse, with approximately twice as many sharply demarcated protrusions, and ~50–80 FALCs/MS together in the omenta and mesentery, although latter structures are sometimes difficult to evaluate as one or more confluent clusters using hematoxylin staining (data not shown).

Peritoneal lavage is a regular procedure to obtain murine PEC for the analysis of the leukocyte composition and characteristics of this

compartment. To investigate whether lavage affects the presence of FLAgs, we compared their appearance and frequency after hematoxylin staining but found no difference to untreated controls, indicating that during PEC collection the detachment of cells from FLAgs is minimal if any (data not shown).

Subsequent electron microscopic analysis using semithin sections revealed that the FLAg structures are enveloped in a mesothelial layer. Underneath this capsule, the cortical area is richly perfused with capillaries, whereas the medullary region is enriched for lymphocytes (Fig. 4A–C). The serous surface of mesothelial cells covering FLAgs display several microvilli, whereas in the deeper regions, CD138-positive plasma cells can be frequently observed intermingled with reticular cells, often in paired arrangements, comprising around 2.5–6.5% of leukocytes (35–55 cells stained positive for CD138 from a midlevel focus plane of FLAgs containing 850–1250 cells) (Fig. 4D–F).

According to these findings, the murine visceral serous surface contains preformed leukocyte-rich areas with different appearances that can bind DLBCL cells. Among these structures, the FLAgs represent a uniquely shaped variant present in

FIGURE 4. Ultrastructure of FLAgs. (**A**) One-micron-thick longitudinal section of a FLAg with the stalk attachment to the peritoneal membrane, stained with toluidine blue. (**B** and **C**) High-power magnification views of the boxes marked in figure (A). (B) The surface of the FLAg is covered by mesothelial cells (dashed line). Reticular cells [arrows in (B)] and lymphocytes [in (C)] fill the FLAg body. (**D**) Electron micrograph of the FLAg's central part showing mesothelial cells with microvilli (arrowheads), one capillary (C), and the extravascular region populated by lymphocytes. (**E**) High-magnification electron micrograph showing two adjacent plasma cells containing extensive endoplasmic reticulum. (**F**) Representative image of anti-CD138 whole-mount immunohistochemistry of FLAgs shows single or paired (arrow) plasma cells (*n* = 6). Scale bar, 100 μm.
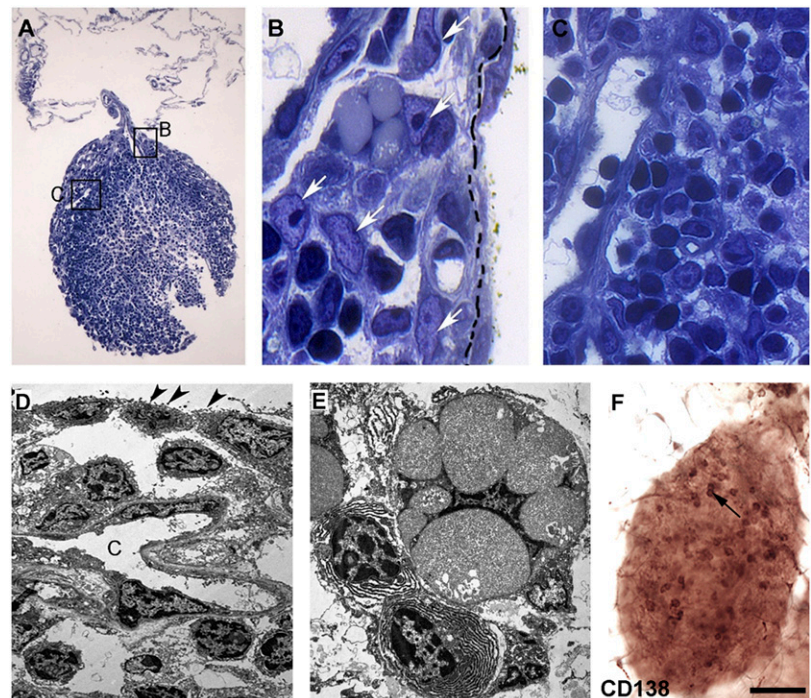
both membrane-attached and adipose-associated locations, and these formations collect most efficiently the lymphoma cells injected i.p.

Lymphoid architecture and homeostatic chemokine domains of FLAgs affecting the segregation of lymphocytes and DLBCL subtypes

The striking form of FLAgs clearly distinguishable from the more diffuse forms of serous leukocyte clusters (such as MS or FALCs) prompted us to investigate their lymphoid subset composition using whole-mount immunohistochemistry. To verify their leukocyte content, we first used anti-CD45 labeling, resulting in a robust reactivity throughout the FLAgs, compared with the slightly less–dense labeling of the FALCs on the serous surface of adipose cuffs (Fig. 5A). Anti–Thy-1/CD90 labeling demonstrated a concentrated accumulation of T cells within the medullary region of FLAgs, whereas the anti-B220 labeling revealed a more diffuse B cell distribution (Fig. 5B, 5C). The marginal area of the FLAgs contained a dense network of LYVE-1–positive cells (Fig. 5D), previously described as FALC/MS-associated macrophages (10). Using dual immunofluorescence for Thy-1 and IgM, followed by confocal microscopy, we confirmed that Thy-1–positive T cells accumulated separately from the IgM-positive B cells, latter typically located at the peripheral regions toward the stalk connection and the tip regions as well as on the surface (Fig. 5E).

The partially segregated pattern of T and B cells suggested the presence of homeostatic chemokines recruiting specific lymphocyte subsets to separate domains within FLAgs. Labeling for Thy-1, B220, and either CCL21 or CXCL13 revealed discrete regions with different chemokine production. Thus, CCL21 production was confined to the central region of the FLAgs coupled with T cell clustering, whereas CXCL13 expression appeared more widespread (Fig. 5F, 5G). These findings suggest that within FLAgs a central region with T cell enrichment is partially separate from the peripheral B cell rich regions, parallel to corresponding homeostatic chemokine dominance.

To test whether the central CCL21-positive domain and the peripheral CXCL13-producing region can also affect the positioning of B cell lymphoma cells with different lymphoid compartment derivation, we compared the distribution of Bc.DLFL1 as extrafollicular DLBCL and A20 as centroblastic DLBCL (24), respectively. Cell surface phenotyping for B cell–associated markers revealed that whereas both Bc.DLFL1 and A20 cells demonstrated similar levels of surface CD19, in Bc.DLFL1 cells, the expression of CD21 and CD23 were reduced, whereas MAC-1/CD11b/CD18 expression was increased compared with A20 cells (Fig. 6A). Importantly, A20 cells display CXCR5 and lack CCR7, whereas Bc.DLFL1 cells have the opposite chemokine receptor pattern (Fig. 6B). Spectral karyotyping analysis (performed at the Molecular Cytogenetics Facility MD Anderson Center, Houston, TX) also revealed a different karyotype for Bc.DLFL1 cell, including 39–41 XX with t(6:10); t(10:6); t(10:11), in contrast to 39X/−, t (2, 15), del (6), del (9), dup (14) reported for A20 (24). Thus, these two DLBCL lines represent genetically and phenotypically two distinct lymphoma variants.

We found that 2 h after i.p. injection of mixed lymphoma cells, A20 cells accumulate at the cortical rim of the FLAgs, whereas Bc.DLFL1 cells readily enter the central region of the FLAg body where, under normal circumstances, T cells congregate. Interestingly, within the omental or mesentery-associated flat FALCs, such segregation did not occur, the A20 and Bc.DLFL1 cells remained mixed (Fig. 6C, 6D). To exclude that the differential migration within FLAgs was due to a competition between two different cell types being simultaneously present, we repeated this experiment using A20^{Lacz} cells alone. We found that, at the same time point, A20^{Lacz} cells remained excluded from the center of the FLAgs and accumulated in the cortical rim, whereas in FALCs, they were diffusely distributed (Fig. 6E, 6F), thus their exclusion from the FLAg center was not due to the presence of competing cells.

These data establish that, within FLAgs, different chemokine domains exist that segregate T and B cells and can also influence the specific accumulation of DLBCL subtypes as defined by their chemokine receptor display, whereas in FALCs, such lymphoma segregation is absent.
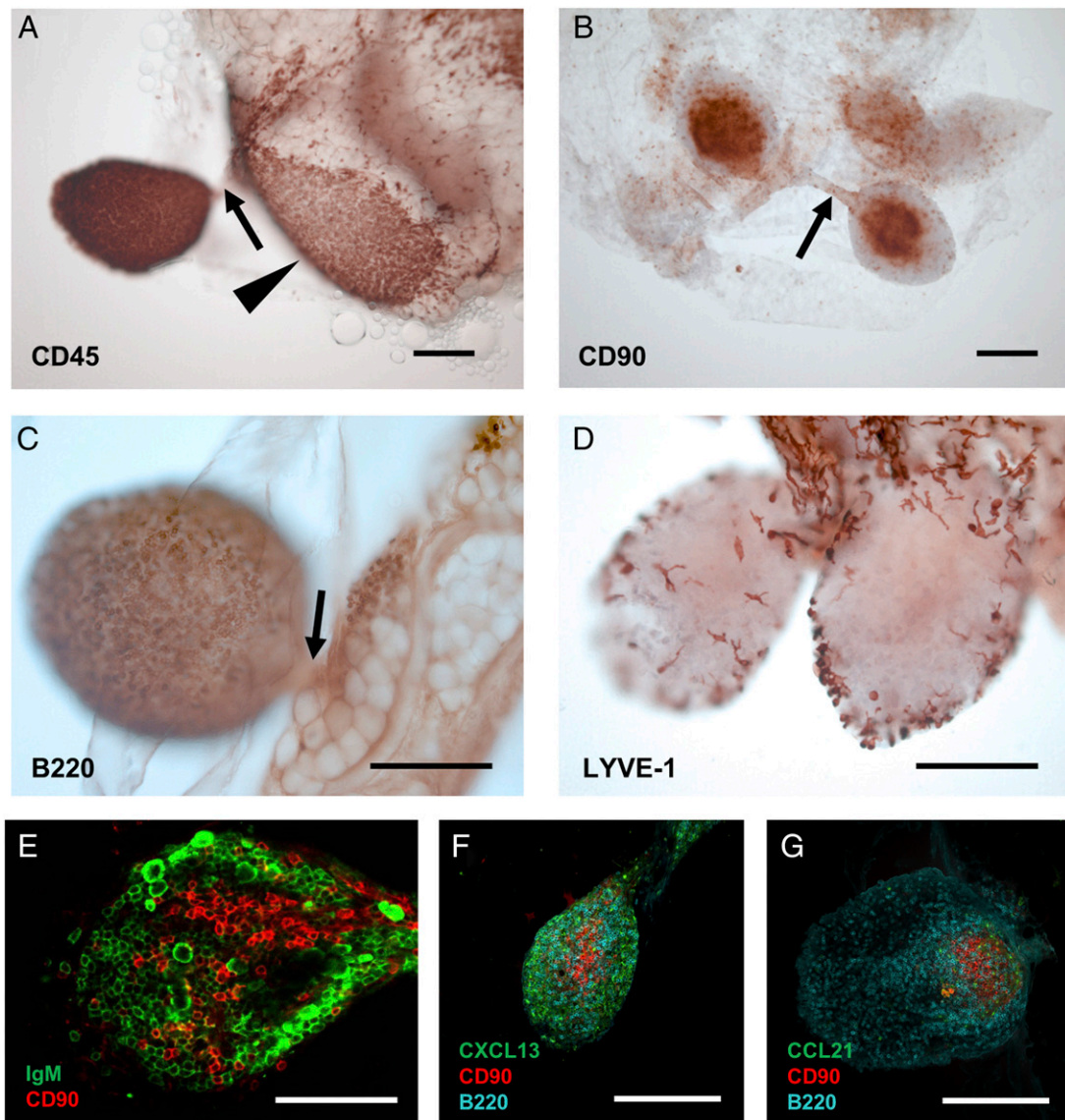
FIGURE 5. Lymphoid organization and homeostatic chemokine domains of FLAgs. Omental (**A**), membrane-bound (**B**), and mesentery-associated variants (**C** and **D**) were labeled for the markers as indicated using indirect immunohistochemistry and DAB reaction (brown) of whole-mount samples. Arrows in (A)–(C) mark stalk, arrowhead in (A) points to a FALC/MS. (**E**) Partial T/B compartmentalization revealed with anti-IgM (green) and anti-CD90/Thy-1 (red) dual immunofluorescence by confocal microscopy (2.5-μm optical section thickness). (**F**) B cell chemoattractant CXCL13 (green) is expanded in the peripheral segment enriched for B cells (turquoise) with a relative paucity in the region with T cell clustering (red). (**G**) Focal accumulation of CCL21 (green) adjacent to T cell clustering (red) and its absence in the B cell populated region in membrane-associated FLAg. Scale bars, 200 μm (representative figure, $n = 5$ mice per group, repeated twice).

Stromal organization and vascular layout of FLAgs

The presence of capillaries and reticular cells in FLAgs suggested the prolonged persistence of these lymphoid formations, raising the question of organization of their nonhematopoietic constituents. We first tested if FLAgs contain Fn as major ECM component. We found that FLAgs in both membrane- and adipose-associated locations contain an extensive Fn meshwork throughout the FLAg body, extending into the stalk regions (Fig. 7A). Using VCAM-1 as a broadly expressed stromal marker expressed in peripheral lymphoid organs, we found a pronounced capillary labeling along the FLAgs stalk, as well as cells with reticular fibroblastic appearance (Fig. 7B).

Using anti-CD31 immunohistochemistry, we found that both the stalk and body parts of FLAgs contain an elaborate meshwork of CD31-positive blood capillaries. Furthermore, within the stalk-proximal parts of both omental and mesentery-associated FLAgs,

short PNAd-positive vascular segments could be detected (Fig. 7C). Using anti–MAdCAM-1, CR1/2, and anti-ICAM immunohistochemistry, the FLAgs did not display any discernible follicular stromal reactivity suggesting follicular dendritic cells or mucosal-type HEVs (data not shown).

We also sought to identify lymphatic capillaries staining for hyaluronan receptor LYVE-1 (25) or the expression of lymphatic endothelial cell (LEC)–specific transcription factor Prox-1 (26). We found that FLAgs contained only a few scattered cells expressing GFP in Prox-1 reporter mice (Fig. 7D). Furthermore, whereas macrophages with intense LYVE-1 labeling were present in a discontinuous arrangement at the FLAg edges, as described for omental FALCs and MS (10), they showed no vascular organization, supporting the lack of lymphatics (Fig. 7E, 7F).

These findings reveal that the nonhematopoietic structure of FLAgs includes VCAM-1–positive stromal cells embedded in a
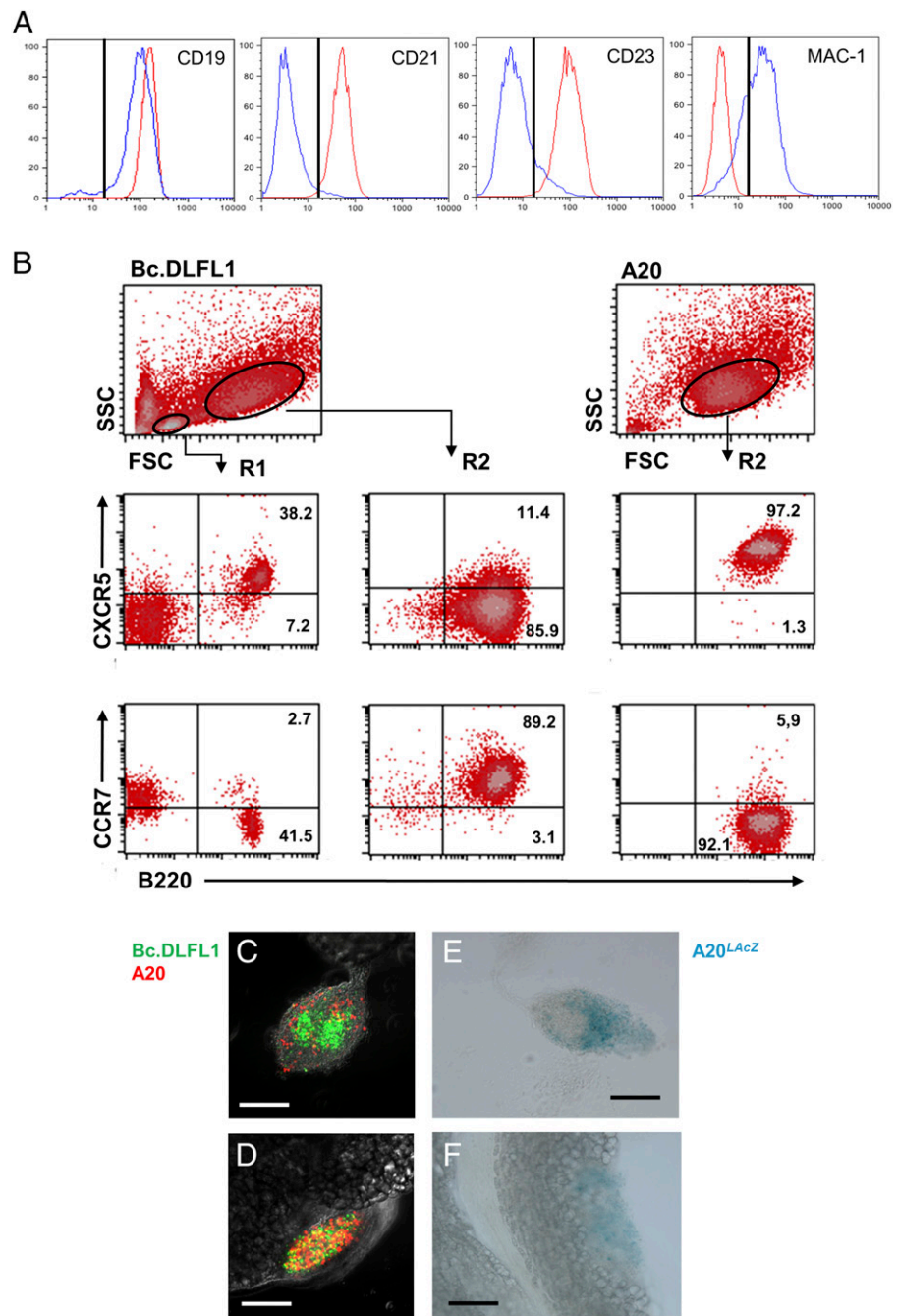
FIGURE 6. Surface characteristics and in vivo segregation of Bc.DLFL1 and A20 DLBCL cells in serous lymphoid tissues correlated with their chemokine receptor expression and tissue variant. (**A**) Different surface phenotype of Bc.DLFL1 (blue) and A20 (red) lymphoma cells in histogram overlays (markers indicated at the top, vertical line indicates the cutoff for control labeling). (**B**) Differential expression of chemokine receptors CXCR5 and CCR7 in Bc.DLFL1 and A20 cells in comparison with normal B cells (gated on live B220-positive lymphocytes [R1] or blast [R2] cells as defined by FSC/SSC). Representative sample of an experiment repeated twice. (**C**) Segregation of CFSE-labeled Bc.DLFL1 cells (green) and CTFR-labeled A20 cells (red) 2 h after injection segregate in FLAg. (**D**) In diffuse FALCs, the two lymphoma variants remain mixed (using differential interference contrast [DIC] image background). (**E**) Without competitor cells, A20^{Lacz} cells (detected by X-gal staining, blue) are also excluded from the central region and accumulate in the periphery of the FLAg but are scattered throughout the FALC (**F**). Scale bars, 100 μm (representative figures, $n = 6$ mice per group, repeated twice).

Fn-rich ECM, and FLAgs are supplied by blood capillaries containing short PNAd-positive segments, but FLAgs lack a defined LEC vasculature.

Peritoneal spreading of DLBCL involves LYVE-1–positive macrophages, followed by propagation through mesenteric lymphatic capillaries

To chart the lymphoma-binding and dissemination routes following i.p. injection involving FLAgs, next, we used various labeling strategies. First, we investigated whether Bc.DLFL1 cells bind to the LYVE-1–positive macrophages. Using CFSE-labeled lymphoma cells and combined immunofluorescence for LYVE-1 and Fn as FLAg ECM compound, we found that 1 h after injection, CFSE-labeled lymphocyte accumulate at the tip part of the FLAgs enriched for LYVE-1–positive macrophages, whereas a small fraction had already entered the FLAg body. Interestingly,

both migrating lymphoma cells and LYVE-1–positive macrophages could be observed in a close association with Fn bundles (Fig. 8A).

To confirm that it is indeed macrophages that mediate the early binding of lymphoma cells, next, we studied how their depletion by the i.p. administration of clodronate liposomes (27) affects lymphoma homing. We found that a 24-h-long pretreatment with clodronate liposome led to an ∼80% reduction in the subsequent mesenteric and omental binding of XenoLight DiR–labeled Bc.DLFL1 cells after a 4 h period (Fig. 8B, 8C) together with the substantial loss of LYVE-1–positive macrophages from the peritoneal membrane and FLAgs (Fig. 8D–F) compared with PBS-liposome control treatment, indicating effective removal of macrophages that, in turn, led to the significant reduction of serous lymphoma adhesion.
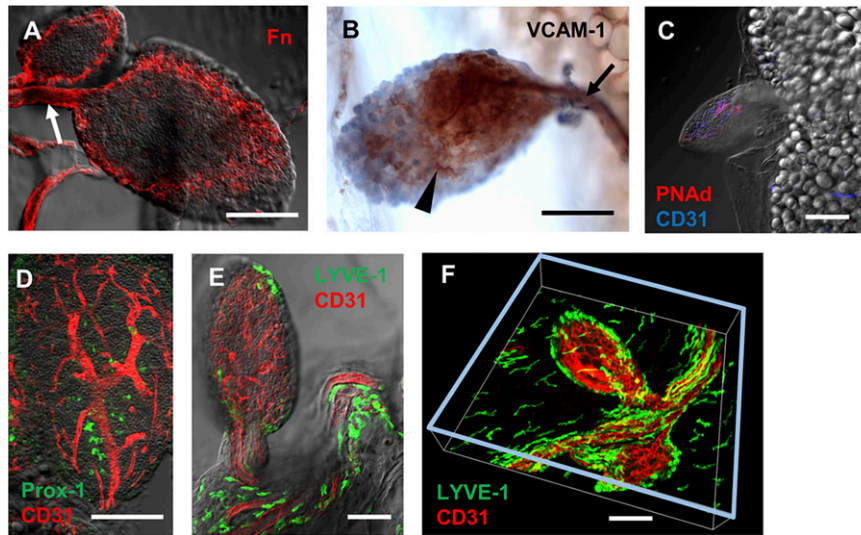
FIGURE 7. Stromal organization and patterning of FLAgs. (**A**) Peritoneal membrane-bound FLAg labeled for Fn reveals a dense Fn meshwork throughout the FLAg body, extending into the FLAg stalk (indicated with an arrow) with differential interference contrast (DIC) image background. (**B**) Anti–VCAM-1 immunohistochemistry (brown/DAB staining) of a mesentery-associated FLAg shows one capillary within the stalk (arrow) and several reticular cells with branched appearance in the FLAg body (arrowhead). (**C**) Within the extensive capillary meshwork in mesentery-associated FLAgs stained for CD31 (blue), short PNAd-positive segments (purple) are present. (**D**) Dispersed cells with Prox-1/GFP (green) expression correlated with CD31 (red) endothelial staining indicates the absence of defined lymphatic capillaries. (**E**) LYVE-1 staining (green) in combination with CD31 (red) labeling also demonstrates the lack of LECs, with strongly LYVE-1–positive cells displaying macrophage features. (**F**) Three-dimensional (3D) reconstitution of Z-stacks containing rich CD31-positive (red) capillary meshwork, with LYVE-1–positive macrophages (green) enriched at the edge of FLAgs, also present as individually dispersed cells in the peritoneal membrane. Scale bars 50 μm. (representative figures, $n = 6$ mice per group, repeated twice).

As the progress of Bc.DLFL1 lymphoma involves spreading into the mLNs, next, we studied whether injected lymphoma cells can be located within the mesenteric lymphatic capillaries. Using CFSE-labeled lymphocytes and anti-FITC whole-mount immunohistochemistry, first, we found thin-walled capillaries within the adipose streaks of mesentery in a close vicinity of original lymphoma attachment at 24 h after the injection, suggestive of lymphatic vessels (Fig. 8G). To verify the entry of lymphoma cells into lymphatic capillaries, we used (*Prox1*-GFP crossed with BALB/c) F1 backcross mice as lymphoma recipients expressing GFP in LECs (18); thus, the positioning of CTFR (red) fluorescence labeled lymphoma cells within capillaries formed by GFP-marked LECs could be analyzed by confocal microscopy without immunological rejection. We found that, as early as 4 h postinjection, CTFR lymphoma cells enter the GFP-positive lymphatic capillaries (Fig. 8H, 8I) in the mesentery.

According to our findings, the initial event for the serous propagation of DLBC lymphoma cells is their attachment to LYVE-1–positive macrophages in FLAgs and less efficiently in FALCs. Next, the lymphoma cells migrate toward the lymphatic capillaries within the mesentery, where the lymphoma cells can enter the draining capillaries, thus gaining access to the mLNs for subsequent expansion. Moreover, as the FLAgs (although they efficiently bind B cells and DLBCL cells) are devoid of demonstrable lymphatic capillaries, the entry sites of i.p. injected lymphoma cells into the mesenteric lymphatic drainage are located outside the FLAgs.

Vascular entry of lymphocytes to serous lymphoid tissues is partly L-selectin dependent

The presence of PNAd-positive segments in both mesenteric and omental FLAgs and FALCs raised the possibility of their involvement in the local leukocyte extravasation mediated by PNAd ligand L-selectin, similar to pLNs. To determine whether the blockade of L-selectin abrogates the serous extravasation of lymphocytes from

blood vessels, we performed a competitive adoptive cell transfer experiment using KikGR detection (19). In this study, KikG cells pretreated with saturating amount of anti–L-selectin mAb MEL-14 were coinjected i.v. with untreated KikR cells (with the Kik fluoroprotein switched to red variant upon photoconversion of pLNs from KikG mice), and their relative appearance in the omentum and mesentery was determined by flow cytometer following CD45 labeling (Fig. 9A). We found that, 1 h after the injection, a substantial blockade occurred in the pLNs, whereas no measurable alteration of the original KikG/KikR ratio was observed in the spleen with L-selectin–independent homing. In the mesentery, a partial blockade could be observed, at around 50% less inhibition of homing compared with pLN (Fig. 9B). In the omentum, we detected only very sparse Kik donor cell appearance in this period, hampering the precise determination of the degree of inhibition (data not shown).

Next, we compared the expression of mRNA for the core proteins and glycosylation enzymes necessary for the production of MECA-79 epitope of PNAd. Although the FLAgs are more abundant in the mesentery in variable distribution, we chose omenta as sample, owing to their more uniform tissue size and composition, including the presence of FLAgs. With quantitative PCR of omental samples, we found that *Cd34*, endomucin (*Emcn*) and podocalyxin (*Podxl*) core proteins mRNA and β1-6GlcNAc transferase (*Cgnt2*) enzyme mRNA levels variably increased, whereas GLYCAM (*Glycam1*) core protein, intercellular cell adhesion molecule/ICAM (*Icam*) as well as *Cgnt1*, β-1,3-N-acetylglucosaminyltransferase (*B3gnt3*) and fucosyltransferase (*Fut7*) enzyme mRNA increased to different degrees in comparison with pLN reference of target gene/β-actin mRNA ratios (Fig. 9C, 9D).

These data indicate that the extravasation of blood-borne lymphocytes to serous lymphoid tissues partially depends on the interaction between L-selectin and MECA-79–positive PNAd endothelial ligands, generated by the concerted action of several core proteins and modifying enzymes with detectable level of
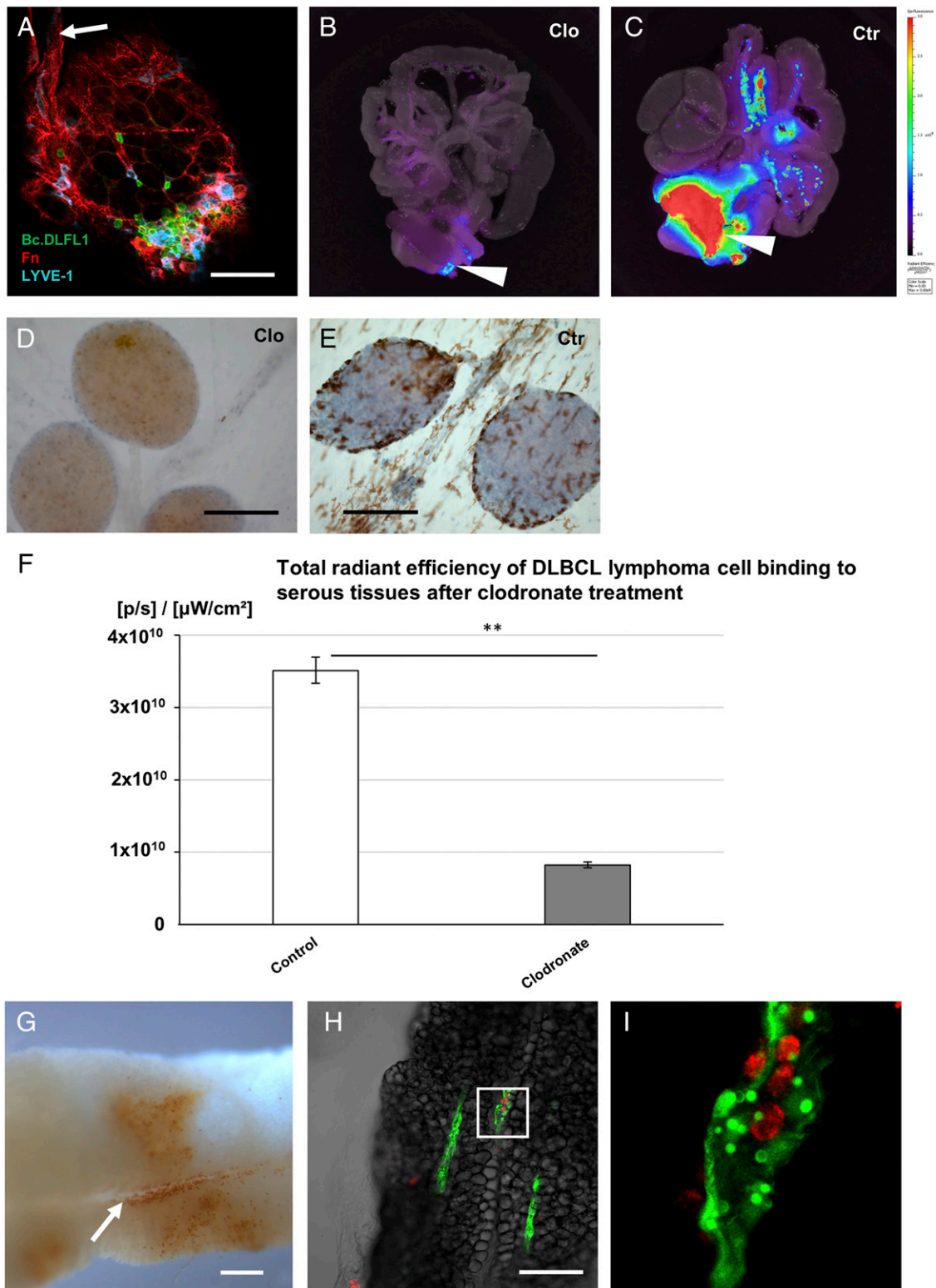
FIGURE 8. DLBCL binding to LYVE-1–positive macrophages and entry into *Prox1*-positive lymphatic vessels. (**A**) Initial binding of CFSE-labeled Bc.DLFL1 cells (green) to LYVE-1–positive (blue) macrophages at the tip of membrane-associated FLAg (outlined by Fn-staining, red; median plane, 2.5-μm optical thickness) 2 h after i.p. injection of lymphoma cells; arrow indicates a stalk. (**B**) Pretreatment with clodronate liposome effectively reduces adherence of XenoLight Dir–labeled lymphoma cells to serous lymphoid organoids compared with PBS-liposome pretreatment (**C**) [arrowheads in (B) and (C) point to omental signal source]. (**D**) Administration of clodronate liposome treatment eliminates LYVE-1–positive macrophages compared with PBS–liposome control (**E**) (samples stained with anti–LYVE-1 immunohistochemistry using H_2O_2/DAB [brown] development 24 h after liposome treatment). Scale bars, 200 μm. (**F**) Quantitation of the reduction of serous binding of XenoLight DiR–labeled Bc.DLFL1 lymphoma in clodronate liposome-treated mice as indicated by total radiant efficiency (average ± SD; $n = 3$ mice per group). **$p < 0.01$. (**G**) Congregation of CFSE-labeled lymphoma cells (detected with anti-FITC–HRP, brown) around and within a thin-walled mesenteric lymphatic vessel (arrow). Scale bar, 1 mm. (**H**) Using dual fluorescence CTFR-labeled cells (red) are positioned within or adjacent to these structures expressing *Prox1*^{GFP}. Scale bars, 200 μm. (**I**) A higher magnification of the region outlined with a rectangle in (H) is demonstrated. Representative image from a cohort of three mice.
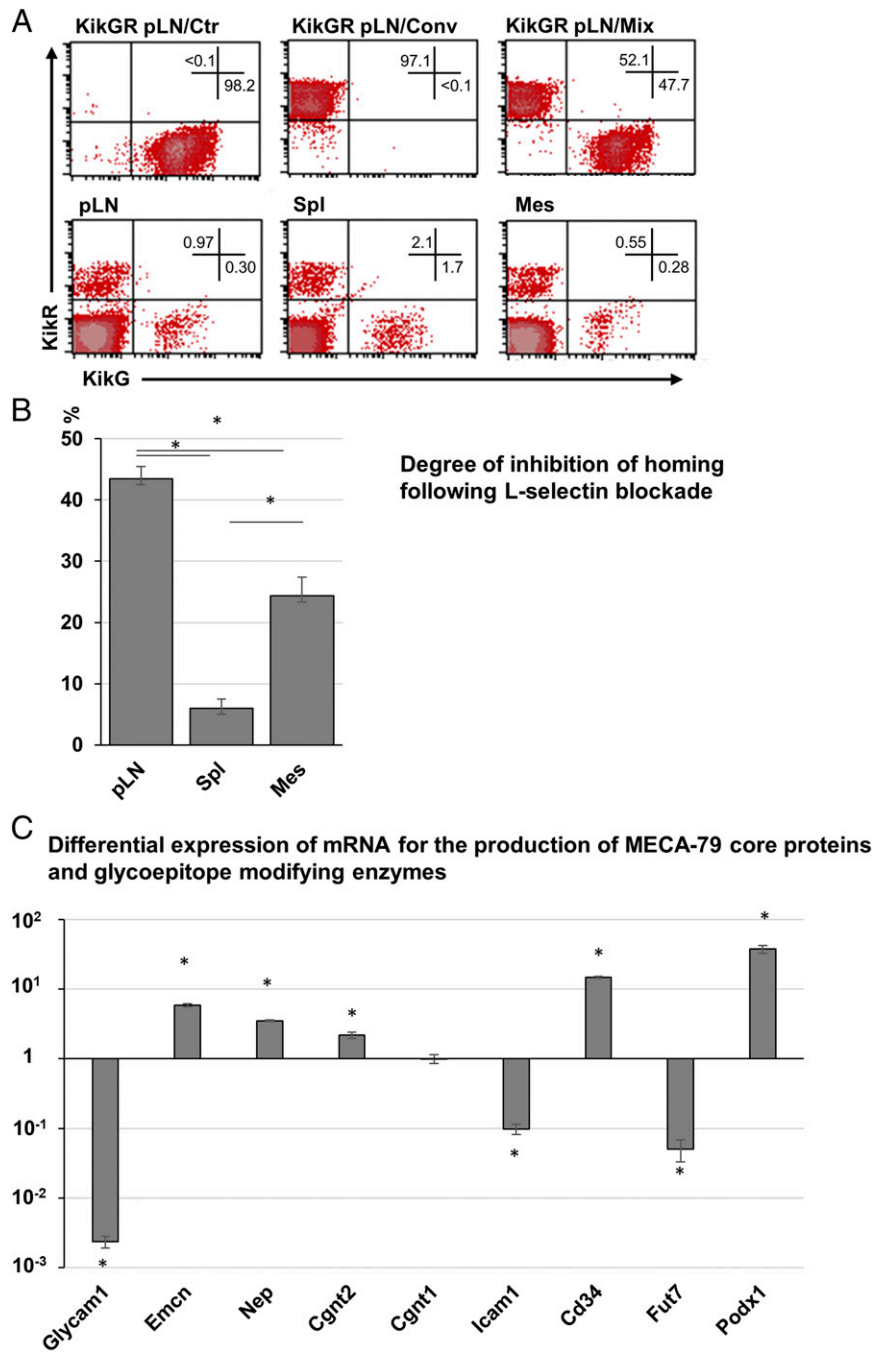
FIGURE 9. Partial L-selectin dependence of serous homing and mRNA profile of omental PNAd production. (**A**) Flow cytometric identification of lymphocytes from unconverted KikG (top left) and converted KikR (top middle) lymph nodes and their mixture (top right) gated on FSC/SSC/CD45, with the frequency of cells in the corresponding quadrants indicated in the upper-right quadrant of the density plots, with the KikG/KikR parameters indicated at the horizontal and vertical axes. In the bottom row, the KikG/KikR distribution is shown in pLNs, spleen (Spl), and mesentery (Mes) from mice injected with a mixture of anti–L-selectin, mAb-treated KikG and untreated KikR lymphocytes (representative figures from a group of three mice). (**B**) Quantitation of the degree of inhibition of tissue homing of KikG lymphocytes by MEL-14 mAb 2 h after the injection of KikG/KikR lymphocyte mixture ($n = 3$ mice per group). (**C**) Comparison of core protein and glycosylation enzyme mRNA involved in the production of MECA-79 in the omentum and lymph nodes by quantitative PCR (qPCR). The ratios of target gene/β-actin mRNA ratio are depicted, in which the pLN value is indicated as 1 (average $\pm$ SEM, $n = 3$ mice/group). *$p < 0.05$.

mRNA production, probably via the simultaneous involvement of different serous lymphoid organoids.

Discussion

In our present work, we establish that, following i.p. injection, normal B cells and DLBCL cells readily colonize various serous lymphoid organoids in the abdominal cavity whence, despite the lack of lymphatic vessels, they gain access to the mesenteric lymphatic capillaries. These capillaries, in turn, thus represent a dual afferentation route for the mLNs, draining both the gut and the peritoneal cavity. As early serous docking sites, morphologically different lymphoid formations may be seeded by lymphoma cells (6) and normal B cells, including a hitherto undescribed structure denoted as FLAg in a process involving LYVE-1–positive peritoneal macrophages. FLAgs show a partial T/B compartmentalization and the presence of domains

producing CXCL13 and CCL21 homeostatic chemokines. Furthermore, in contrast with the previously described diffuse MS and FALC structures (1, 2), FLAgs are completely enveloped into mesothelial cells, suggesting a hitherto unknown type or stage of adipose-associated peripheral lymphoid tissues.

The degree of compartmentalization of the bulk of omental lymphoid tissues into T and B cell zones is substantially less than that of the mucosal draining sites, such as mLNs or Peyer's patches (1, 2, 10). However, in FLAgs, a concentrated T-zone can typically be identified, corresponding to the region producing CCL21, whereas the peripheral region of FLAgs is enriched for CXCL13 production, which is necessary for omental B cell entry (7, 10). In the omentum, CXCL13 production has been attributed to both hematopoietic cells and, to a lesser extent, nonhematopoietic stromal cells (8, 10). In FLAgs, the relative enrichment of VCAM-1–positive stromal cell in the center suggests possible

involvement in CCL21 production, whereas the more prominent production of CXCL13 in the periphery can be linked to LYVE-1–positive macrophages (10), in addition to VCAM-1 being a possible key vascular adhesion molecule for omental homing of recirculating B cells (11). Whether follicular dendritic cells as cardinal CXCL13-producing stromal cells in secondary lymphoid tissues are also present in FLAgs requires further investigations, including phenotypic analysis and functional assays, particularly germinal center formation and long-term immune complex retention. Although the treatment of EL4 T cell lymphoma cells with pertussis toxin did not affect their accumulation in omental foci (7), T and B cells and various DLBCL variants within FLAgs show evidences for partial segregation, indicating that the various forms (MS and FALCs) of serous lymphoid aggregates have different levels of chemokine-mediated organization affecting T/B positioning. It is not yet known whether B-1 B cells within the B cell–rich areas accumulate to separate regions relative to the B-2 subset. Thus, for determining the significance of pertussis toxin–sensitive chemokine signaling in the subsequent omental or mesenteric migration of B cells and DLBCL cells within different types of serous lymphoid tissues, further investigations are needed.

Importantly, previous studies demonstrated that the surgical removal of omentum did not prevent the departure of peritoneal B cells, hinting at other potential exit sites (11), with mesenteric FALCs and FLAgs offering possible candidates as demonstrated in our present work. Our findings indicate mesenteric lymphoid organoids (including FALCs and FLAgs) as alternative lymphocyte-binding sites for subsequent exit routes, at an efficiency of lymphoma binding nearly equal to omental MS lymphoma adhesion. Among various formations, we observed different lymphoma-binding kinetics, indicating faster homing to FLAgs compared with FALCs, which may mediate both more efficient adherence and faster exchange kinetics, as the FLAg-bound lymphoma cell load did not change significantly over a 24-h period.

In contrast to the abundance of blood vasculature, in the omentum, we found only occasional LEC-marker expression, unlike in the mesentery, where typically several confluent lymphatic vessels displaying Prox-1 and LYVE-1 are present. Moreover, relying on these markers, we failed to detect lymphatic connection between the FALCs or FLAgs as mesenteric lymphoma-docking sites and the deep-running lymphatic vessels. Therefore, we can rule out direct lymphatic communication connecting either FLAgs or FALCs and mesenteric lymphatics, clearly necessitating further investigations to clarify the movement of FLAg/FALC-attached lymphocytes and lymphoma cells toward the mesenteric lymphatic vessels. Nevertheless, our kinetic analyses suggest that relatively early (4 h) after the i.p. injection, DLBCL cells are already detectable within the mesenteric lymphatic capillaries. Furthermore, the kinetics of normal B cell distribution following i.p. injection also suggests a faster departure from the mesentery than from the omentum after 24 h, possibly because of the drainage via the mesenteric lymphatic vessels, which appear absent in the omentum. Moreover, similar early accumulation of both normal B cells and DLBCL cells in human tumors with disrupted Gα13 (thus compromising S1P-mediated inhibition of migration induced by CXCL12) was also noted in the parathymic lymph nodes, where lymphocytes could reach this site either across the lymphatic stomata of the diaphragma or via lymphatic vessels (11, 28). In addition, radiodiagnostic imaging of human patients has also revealed the propagation of Burkitt lymphoma and DLBCL via the gastrocolic, gastrosplenic, and other peritoneal ligaments toward the mesocolon

(29). Subsequent inflammatory reactions may expand the pre-existing lymphatic vasculature by LEC proliferation upon the effect of VEGF-C produced by perivascular smooth muscle cells and macrophages or by the direct integration of LEC-switched macrophages (30).

The capacity of lymphoma cells to adhere to such serous lymphoid formations along the mesentery represents a significantly expanded spectrum of potential propagation sites for this type of malignancies in addition to the omental MS also targeted by gastric, colonic, and ovary cancer cells (6, 31, 32). As both mesenteric FALCs and omental MS are able to host local immune responses, the entry of tumor cells into these lymphoid territories may elicit an immune reaction against such cells (1, 2, 6). However, the adipose microenvironment also offers a supportive milieu for cancers, thus antagonizing the efficiency of antitumor immune responses (31, 33, 34), in which cytotoxic reactions can also be modulated by ILC2 and myeloid-derived suppressor cells (8, 35). This tumor growth–promoting function may manifest in several ways, including the niche function of local microenvironment to support cancer stem cell growth. Alternatively, these sites may attract putative tumor–associated stroma precursors, including myofibroblast precursors or mesenchymal stem cells that exert immunosuppressive activity (36, 37) as well as chemotactic signals, including CXCL12–CXCR4 and CCL22–CCR4 interactions (38, 39). In omental tissue, the local microvascular network of actively sprouting CD105-positive capillaries influenced by VEGF-A binding several tumor types (32) may facilitate both the entry for recirculating stroma precursors and exit for cancer cell dissemination. In addition, local mesothelium–mesenchymal transition may also promote the appearance of cancer-associated fibroblasts, whereas adipocytes may also contribute to vessel expansion following their dedifferentiation and endothelial redifferentiation (40, 41).

The i.v. entry of lymphocytes to the MS and their retention, and their peritoneal entry are likely to be mediated by different adhesion events, as the egress from the peritoneal cavity was independent from β7 integrin ligand binding (11). The detectable level of mRNA for various PNAd core proteins and modifying enzymes involved in the generation of MECA-79 epitope in selective segments of vasculature within the omenta and mesentery supports the view that the local formation of available endothelial ligand permits L-selectin–mediated homing of blood-borne leukocytes, similar to pLN HEVs. However, the precise comparison with pLN HEVs necessitates the isolation of FLAgs for the enrichment of MECA-79–positive endothelial cells. Furthermore, anti–L-selectin treatment could only partly inhibit the entry of blood-borne lymphocytes to serous lymphoid tissues, indicating other potential endothelial recognition mechanisms, also likely to be independent from MAdCAM-1 binding, as the FLAg-associated vascular segments lacked this addressin. Because of the small size and transparent appearance of FLAgs, our attempts to isolate them in unfixed and unstained conditions have remained unsuccessful. Nevertheless, the presence of PNAd-positive vessels as well as the efficient binding through LYVE-1–positive macrophages together (thus offering access for both blood-borne and serous leukocytes) may explain the increased lymphocyte density within FLAgs compared with omental or mesenteric FALCs. Further analyses are required to identify other endothelial ligand–receptor pairs that facilitate serous homing of recirculating leukocytes.

In summary, we propose that the serous lymphoid aggregates function as peritoneal collection sites for both normal B cells and DLBCL cells. These lymphoid clusters have diverse structural variants displaying different degrees of lymphocyte compartmentalization, with FLAgs demonstrating a more organized

variant. From these sites, the peritoneal lymphocytes may subsequently reach the mesenteric lymphatic capillaries, which, in turn, thus represent shared transit routes for both leukocytes, leaving the mucosal and the serous compartments, whereas the dissemination of peritoneal leukocytes and lymphoma cells may involve also other routes, particularly toward the mediastinal cavity and pleural surface. As initial contact partner cells binding B cell and DLBCL, LYVE-1–positive macrophages may play crucial roles; however, the identity of chemotactic and other factors guiding the lymphocytes toward the mesenteric lymphatic capillaries remains to be determined.

Acknowledgments

Disclosures

The authors have no financial conflicts of interest.

References

1. Meza-Perez, S., and T. D. Randall. 2017. Immunological functions of the omentum. *Trends Immunol.* 38: 526–536.
2. Cruz-Migoni, S., and J. Caamaño. 2016. Fat-associated lymphoid clusters in inflammation and immunity. *Front. Immunol.* 7: 612.
3. Jackson-Jones, L. H., and C. Bénézech. 2018. Control of innate-like B cell location for compartmentalised IgM production. *Curr. Opin. Immunol.* 50: 9–13.
4. Ha, S. A., M. Tsuji, K. Suzuki, B. Meek, N. Yasuda, T. Kaisho, and S. Fagarasan. 2006. Regulation of B1 cell migration by signals through toll-like receptors. *J. Exp. Med.* 203: 2541–2550.
5. Liebermann-Meffert, D. 2000. The greater omentum. Anatomy, embryology, and surgical applications. *Surg. Clin. North Am.* 80: 275–293, xii.
6. Liu, J., X. Geng, and Y. Li. 2016. Milky spots: omental functional units and hotbeds for peritoneal cancer metastasis. *Tumour Biol.* 37: 5715–5726.
7. Rangel-Moreno, J., J. E. Moyron-Quiroz, D. M. Carragher, K. Kusser, L. Hartson, A. Moquin, and T. D. Randall. 2009. Omental milky spots develop in the absence of lymphoid tissue-inducer cells and support B and T cell responses to peritoneal antigens. *Immunity* 30: 731–743.
8. Ansel, K. M., R. B. Harris, and J. G. Cyster. 2002. CXCL13 is required for B1 cell homing, natural antibody production, and body cavity immunity. *Immunity* 16: 67–76.
9. Moro, K., T. Yamada, M. Tanabe, T. Takeuchi, T. Ikawa, H. Kawamoto, J. Furusawa, M. Ohtani, H. Fujii, and S. Koyasu. 2010. Innate production of T(H)2 cytokines by adipose tissue-associated c-Kit(+)Sca-1(+) lymphoid cells. *Nature* 463: 540–544.
10. Bénézech, C., N. T. Luu, J. A. Walker, A. A. Kruglov, Y. Loo, K. Nakamura, Y. Zhang, S. Nayar, L. H. Jones, A. Flores-Langarica, et al. 2015. Inflammation-induced formation of fat-associated lymphoid clusters. *Nat. Immunol.* 16: 819–828.
11. Berberich, S., S. Dähne, A. Schippers, T. Peters, W. Müller, E. Kremmer, R. Förster, and O. Pabst. 2008. Differential molecular and anatomical basis for B cell migration into the peritoneal cavity and omental milky spots. *J. Immunol.* 180: 2196–2203.
12. Lábadi, A., and P. Balogh. 2009. Differential preferences in serosal homing and distribution of peritoneal B-cell subsets revealed by in situ CFSE labeling. *Int. Immunol.* 21: 1047–1056.
13. Kasagi, Y., Y. Harada, Y. Morodomi, T. Iwai, S. Saito, K. Yoshida, E. Oki, H. Saeki, K. Ohgaki, M. Sugiyama, et al. 2016. Peritoneal dissemination requires an Sp1-dependent CXCR4/CXCL12 signaling axis and extracellular matrix-directed spheroid formation. *Cancer Res.* 76: 347–357.
14. Karaosmanoglu, D., M. Karcaaltincaba, B. Oguz, D. Akata, M. Ozmen, and O. Akhan. 2009. CT findings of lymphoma with peritoneal, omental and mesenteric involvement: peritoneal lymphomatosis. *Eur. J. Radiol.* 71: 313–317.
15. Cabral, F. C., K. M. Krajewski, K. W. Kim, N. H. Ramaiya, and J. P. Jagannathan. 2013. Peritoneal lymphomatosis: CT and PET/CT findings and how to differentiate between carcinomatosis and sarcomatosis. *Cancer Imaging* 13: 162–170.
16. Vojkovics, D., Z. Kellermayer, D. Heidt, M. Mihalj, B. Kajtár, D. Ernszt, T. Kovács, P. Németh, and P. Balogh. 2016. Isolation and characterization of a murine spontaneous high-grade follicular lymphoma with restricted in vivo spreading--a model for lymphatic metastasis via the mesentery. *Pathol. Oncol. Res.* 22: 421–430.
17. Kvell, K., T. Czömpöly, L. Hiripi, P. Balogh, J. Kóbor, L. Bodrogi, J. E. Pongrácz, W. A. Ritchie, and Z. Bosze. 2010. Characterisation of eGFP-transgenic BALB/c mouse strain established by lentiviral transgenesis. *Transgenic Res.* 19: 105–112.
18. Choi, I., H. K. Chung, S. Ramu, H. N. Lee, K. E. Kim, S. Lee, J. Yoo, D. Choi, Y. S. Lee, B. Aguilar, and Y. K. Hong. 2011. Visualization of lymphatic vessels by Prox1-promoter directed GFP reporter in a bacterial artificial chromosome-based transgenic mouse. *Blood* 117: 362–365.
19. Nowotschin, S., and A. K. Hadjantonakis. 2009. Use of KikGR a photo-convertible green-to-red fluorescent protein for cell labeling and lineage analysis in ES cells and mouse embryos. *BMC Dev. Biol.* 9: 49–61.
20. Zhou, W., H. C. Kang, M. O'Grady, K. M. Chambers, B. Dubbels, P. Melquist, and K. R. Gee. 2016. CellTrace™ Far Red & CellTracker™ Deep Red—long term live cell tracking for flow cytometry and fluorescence microscopy. *J. Biol. Methods* 3: e38.
21. Gallatin, W. M., I. L. Weissman, and E. C. Butcher. 1983. A cell-surface molecule involved in organ-specific homing of lymphocytes. *Nature* 304: 30–34.
22. Czömpöly, T., A. Lábadi, Z. Kellermayer, K. Olasz, H. H. Arnold, and P. Balogh. 2011. Transcription factor Nkx2-3 controls the vascular identity and lymphocyte homing in the spleen. *J. Immunol.* 186: 6981–6989.
23. Inoue, Y., K. Izawa, S. Kiryu, A. Tojo, and K. Ohtomo. 2008. Diet and abdominal autofluorescence detected by in vivo fluorescence imaging of living mice. *Mol. Imaging* 7: 21–27.
24. Guja, K., T. Liehr, M. Rincic, N. Kosyakova, and S. S. Hussein Azawi. 2017. Molecular cytogenetic characterization identified the murine B-cell lymphoma cell line A-20 as a model for sporadic Burkitt's lymphoma. *J. Histochem. Cytochem.* 65: 669–677.
25. Prevo, R., S. Banerji, D. J. Ferguson, S. Clasper, and D. G. Jackson. 2001. Mouse LYVE-1 is an endocytic receptor for hyaluronan in lymphatic endothelium. *J. Biol. Chem.* 276: 19420–19430.
26. Wigle, J. T., N. Harvey, M. Detmar, I. Lagutina, G. Grosveld, M. D. Gunn, D. G. Jackson, and G. Oliver. 2002. An essential role for Prox1 in the induction of the lymphatic endothelial cell phenotype. *EMBO J.* 21: 1505–1513.
27. Van Rooijen, N., and A. Sanders. 1994. Liposome mediated depletion of macrophages: mechanism of action, preparation of liposomes and applications. *J. Immunol. Methods* 174: 83–93.
28. Muppidi, J. R., R. Schmitz, J. A. Green, W. Xiao, A. B. Larsen, S. E. Braun, J. An, Y. Xu, A. Rosenwald, G. Ott, et al. 2014. Loss of signalling via Gα13 in germinal centre B-cell-derived lymphoma. *Nature* 516: 254–258.
29. Vicens, R. A., M. Patnana, O. Le, P. R. Bhosale, T. L. Sagebiel, C. O. Menias, and A. Balachandran. 2015. Multimodality imaging of common and uncommon peritoneal diseases: a review for radiologists. *Abdom. Imaging* 40: 436–456.
30. Vaahtomeri, K., S. Karaman, T. Mäkinen, and K. Alitalo. 2017. Lymphangiogenesis guidance by paracrine and pericellular factors. *Genes Dev.* 31: 1615–1634.
31. Clark, R., V. Krishnan, M. Schoof, I. Rodriguez, B. Theriault, M. Chekmareva, and C. Rinker-Schaeffer. 2013. Milky spots promote ovarian cancer metastatic colonization of peritoneal adipose in experimental models. *Am. J. Pathol.* 183: 576–591.
32. Gerber, S. A., V. Y. Rybalko, C. E. Bigelow, A. A. Lugade, T. H. Foster, J. G. Frelinger, and E. M. Lord. 2006. Preferential attachment of peritoneal tumor metastases to omental immune aggregates and possible role of a unique vascular microenvironment in metastatic survival and growth. *Am. J. Pathol.* 169: 1739–1752.
33. Liu, X. Y., Z. F. Miao, T. T. Zhao, Z. N. Wang, Y. Y. Xu, J. Gao, J. H. Wu, Y. You, H. Xu, and H. M. Xu. 2013. Milky spot macrophages remodeled by gastric cancer cells promote peritoneal mesothelial cell injury. *Biochem. Biophys. Res. Commun.* 439: 378–383.
34. Oosterling, S. J., G. J. van der Bij, M. Bögels, J. R. van der Sijp, R. H. Beelen, S. Meijer, and M. van Egmond. 2006. Insufficient ability of omental milky spots to prevent peritoneal tumor outgrowth supports omentectomy in minimal residual disease. *Cancer Immunol. Immunother.* 55: 1043–1051.
35. Horikawa, N., K. Abiko, N. Matsumura, J. Hamanishi, T. Baba, K. Yamaguchi, Y. Yoshioka, M. Koshiyama, and I. Konishi. 2017. Expression of vascular endothelial growth factor in ovarian cancer inhibits tumor immunity through the accumulation of myeloid-derived suppressor cells. *Clin. Cancer Res.* 23: 587–599.
36. Bazhanov, N., J. H. Ylostalo, T. J. Bartosh, A. Tiblow, A. Mohammadipoor, A. Foskett, and D. J. Prockop. 2016. Intraperitoneally infused human mesenchymal stem cells form aggregates with mouse immune cells and attach to peritoneal organs. *Stem Cell Res. Ther.* 7: 27.
37. Klopp, A. H., Y. Zhang, T. Solley, F. Amaya-Manzanares, F. Marini, M. Andreeff, D. Debeb, W. Woodward, R. Schmandt, R. Broaddus, et al. 2012. Omental adipose tissue-derived stromal cells promote vascularization and growth of endometrial tumors. *Clin. Cancer Res.* 18: 771–782.
38. Terai, S., S. Fushida, T. Tsukada, J. Kinoshita, K. Oyama, K. Okamoto, I. Makino, H. Tajima, I. Ninomiya, T. Fujimura, et al. 2015. Bone marrow derived "fibrocytes" contribute to tumor proliferation and fibrosis in gastric cancer. *Gastric Cancer* 18: 306–313.
39. Cao, L., X. Hu, J. Zhang, G. Huang, and Y. Zhang. 2014. The role of the CCL22-CCR4 axis in the metastasis of gastric cancer cells into omental milky spots. *J. Transl. Med.* 12: 267.
40. Poloni, A., G. Maurizi, S. Anastasi, E. Mondini, D. Mattiucci, G. Discepoli, F. Tiberi, S. Mancini, S. Partelli, A. Maurizi, et al. 2015. Plasticity of human dedifferentiated adipocytes toward endothelial cells. *Exp. Hematol.* 43: 137–146.
41. Sandoval, P., J. A. Jiménez-Heffernan, Á. Rynne-Vidal, M. L. Pérez-Lozano, Á. Gilsanz, V. Ruiz-Carpio, R. Reyes, J. García-Bordas, K. Stamatakis, J. Dotor, et al. 2013. Carcinoma-associated fibroblasts derive from mesothelial cells via mesothelial-to-mesenchymal transition in peritoneal metastasis. *J. Pathol.* 231: 517–531.

Role of adipose-associated lymphoid tissues in the immunological homeostasis of the serosal surface

Xinkai Jia [a,b], Gergely Berta [c], Fanni Gábris [a,b], Zoltán Kellermayer [a,b], Péter Balogh [a,b,*]

[a] *Department of Immunology and Biotechnology, Lymphoid Organogenesis Research Group, Szentágothai Research Center, University of Pécs Medical School, Hungary*
[b] *Lymphoid Organogenesis Research Group, Szentágothai Research Center, University of Pécs Medical School, Hungary*
[c] *Department of Medical Biology and Central Electron Microscope Laboratory, Medical School, University of Pécs, Hungary*

A B S T R A C T

Although not typical lymphoid organs, analysis of the visceral adipose-associated lymphoid tissues has recently substantially expanded our knowledge about the immunological features of these elusive compartments. Recent data have highlighted their considerable complexity in cellular organization and interactions in several biological processes, including adaptive immune responses, tissue plasticity to accommodate mesenchymal stem cells and progenitors, and providing a suitable microenvironment for serosal tumor propagation. This review aims to present a comprehensive view of the adipose-associated lymphoid tissues in local and systemic immune responsiveness, with particular emphasis on the omental and mesenteric lymphoid tissues in the serosal defense of abdominal organs.

1. Introduction

According to the Norse sagas collected by Snorri Sturluson, the acclaimed medieval Icelandic poet of the 13th century, Thormud Kolbunarskald (also a famed poet in the army of King Olaf II of Norway) in CE 1030 succumbed to an arrow that had struck his heart, but not before pulling it out himself. Upon inspecting the barb of the removed arrowhead, the mortally wounded poet uttered his last grateful remarks to his former employer: "Well hath the king fed us; fat am I still about the roots of the heart!" His remarkable stoicism notwithstanding, what the dying poet must have failed to notice within the fat attached to the pieces of flesh were those small leukocyte congregates that have been later identified as a new type of lymphoid organelles, typically associated with visceral adipose depots around several organs, including the heart and the intestines. Owing to their small size and scattered distribution, the existence of most of these lymphoid structures were unknown until fairly lately; however, recent studies have revealed the remarkable potential of these practically invisible lymphoid tissues to mediate local immune responses as well as contributing to systemic immunological defense.

The skin, airways, gastrointestinal tract and genitourinary system represent those body surfaces where the immunological defense is typically directed against external pathogens. These sites either contain different types of secondary lymphoid tissues (such as the Peyer's patches and other developmentally programmed lymphoid tissues) formed prior to antigenic exposure [1] or, upon microbial exposure, can establish such tissues (including the bronchus-associated lymphoid tissues [BALT] in the lungs or maturation of intestinal cryptopatches [CP] into isolated lymphoid follicles [ILFs]) [2,3]. Subsequently, these organized secondary or tertiary lymphoid tissues can launch efficient local immune responses [4]. In addition, via lymphatics these regions are connected to an extensive network of lymph nodes to collect pathogens escaping local elimination, thus establishing a second line of defense [4,5].

In addition to these frontier regions open to the external environmental, the dual-layer serosal covering of the internal body cavities in both humans and mice also represent an important surface for immunological surveillance, including the parietal and visceral facets of pericardium around the heart, the pleura around the lungs, and the peritoneum covering the abdominal organs [5–8]. These linings (also enclosing a small amount of greasing exudate fluid to allow the repositioning of enwrapped organs, thus permitting the floating of leukocytes between the opposing surfaces and distinct locations) have been for a long time considered a separate immunological compartment, particularly due to the selective local accumulation of B1 B cells [9,10]. Owing to their liquid-dwelling nature, these lymphocytes and peritoneal

---

leukocytes (granulocytes and macrophages) were thought of as diffuse immune compartment without tissue organization, while recent data indicated the existence of organized leukocyte congregates with immunological roles at various serosal locations.

A typical feature of these lymphoid congregates is that they reside in fat-rich connective tissue microenvironment, in a rather complex anatomical setting combining adipose tissue and serosal lining, without being encapsulated [5,7]. Although their structure is less well defined, data indicate the presence of vascular and mesenchymal stroma as well as specialized mesothelial cells, capable of supporting dynamic interactions between various lymphoid cells via cytokines and chemotactic factors, also allowing these adipose-associated lymphoid organoids to respond to inflammatory stimuli [11–13]. Furthermore, mesenteric adipose tissues also accommodate adipose tissue-derived stem cells and progenitors (ASCs and ADMPC – adipose derived multi-lineage progenitor cells) that can differentiate along several mesenchymal lineages similarly to bone marrow derived mesenchymal stem cells (BMMSCs), including adipocytes and osteoblasts, and can also exert immunomodulatory activities [14–16].

Recently renewed interest in the significance of adipose tissue-associated lymphoid organoids has provided a more comprehensive view of their functions. In the present review focusing on the abdominal adipose-associated lymphoid tissues, we summarize their general features, involvement in local lymphoid organization and immune responses, as well as their role in the serosal propagation of lymphoid and other malignancies.

2. Immunological features of adipose-associated lymphoid tissues

Adipose tissue represents the largest fraction of mesenchyme of the human body, which has emerged as a separate immunological compartment (reviewed in [17]). Its basic constituents are adipocytes, while the smaller non-fat stromal-vascular fraction (SVF) is composed of a mixture of mesenchymal, endothelial, also containing hematopoietic cells. The latter can be assigned to various lymphoid (Treg and Th2 cells, B cells and plasma cells, iNKT cells and ILC2 cells) and distinct phagocytic subsets associated with the vasculature (vasculature-associated macrophages [VAMs]) identifiable by the surface expression of CD11b, CD206, MHCII, Tim4 and CD64 molecules [18,19]. The leukocyte composition of adipose tissues may change in obesity, deviating towards pro-inflammatory preference, including the increase of Th1, Th17 cells and ILC1 as well as IL-6 and TNF production by adipocytes, coupled with macrophage polarization and metabolic alterations [20,21].

While the leukocytes are typically scattered throughout the subcutaneous adipose tissue, a substantial part of the visceral adipose-associated lymphoid organoids of the serosal linings are relatively densely populated by leukocytes in a focal pattern, and are covered with mesothelial cells producing CXCL1 and CXCL13 [11]. These lymphocyte-rich organoids are not separated from their adipocyte embedding, in contrast to lymph nodes, where the perinodal fat cells develop from local preadipocyte precursors found in the embryonic fat pad [22]. Upon contact with lymphoid tissue inducer cells (LTi), these preadipocytes in a lymphotoxin β receptor (LTβR)-dependent manner involving NF-κB2:RelB signaling can also give rise to several stromal cells secreting IL-7 within the lymph nodes [22]. Thus, while promoting lymph node fibroblastic maturation, LTβR signaling negatively impacts the adipogenic differentiation of mesenchymal precursors [23]. In contrast to the lack of lymph nodes, the presence of adipose-associated lymphoid tissues in mice deficient for LTβR indicates that the local mesenchymal differentiation without LTβR signaling permits the establishment of microenvironment suitable for supporting lymphoid accumulation.

In the following section, we will overview the structural and functional characteristics of abdominal adipose lymphoid tissues.

2.1. Omental milky spots and local adaptive immune responsiveness

Due to its capacity to sequester abdominal inflammation, the omentum has traditionally been described (mainly by surgeons) as a policeman of the peritoneal cavity. [24]. The omental leukocyte clusters are termed milky spots (MSs) [25] which structures function as peritoneal exit ports for blood-borne leukocytes [9]. The MSs collect fluids, particles, and cells from the peritoneal cavity [26–28]. MSs are loose structures containing various leukocytes and an extensive capillary meshwork lined by CD31-positive endothelium, also expressing MAdCAM-1 and PNAd addressins in a segmental pattern [29]. Furthermore, recent studies have established that, despite the relatively diffuse appearance of omental lymphoid organoids, the vasculature in these structures is surrounded by phenotypically distinct fibroblastic subsets comprising PDGFRα producing CCL19 or CCL11, and lacking other fibroblastic markers including Thy-1/CD90 and fibroblast activation protein-α (FAPα) [11]. Omental milky spots contain a substantial number of B cells, including B1 and B2 subsets. In mice B1 cells express a high level of IgM and less IgD, display MAC-1 (CB11b/CD18) integrin and are the major source of natural antibodies [30]. B1 cells also express CXCR5 and display more active chemotactic responses to CXCL13 than B2 cells [9], which can be produced by macrophages and also non-macrophage stromal cells and mesothelial cells that are located in the MSs [9,10]. For B2 cells, migration into and out from the peritoneal cavity also relies on the VCAM-1:α4β1 integrin binding and it is also influenced by the peritoneal microenvironment [29,31]. In situ labeling of peritoneal lymphocytes also revealed different exchange kinetics between the T cells, B1 and B2 cells, with the B1 cells retained within the peritoneal cavity for the longest period; however, upon LPS treatment B1 cells can efficiently translocate into the thoracic cavity [32]. In humans, omental adipose tissue has also been shown to harbor plasma cells and at the same time express various Fc receptors, thus enabling plasma cells to influence adipocytes via local antibody production [33].

In addition to serving as lymphocyte accumulation sites, omental MSs have also been demonstrated to host T-dependent humoral immune responses. Splenectomized mice deficient for lymphotoxin-α ($Lta^{-/-}$) thus lacking spleen, lymph nodes and Peyer's patches (SLP mice) were immunized with 4-hydroxy-3-nitrophenyl-acetyl(15)-OVA (NP-OVA) and sheep erythrocytes (SRBC). Upon the i.p. administration of NP-OVA, in SLP mice the serum titers of NP-specific IgM and IgG rapidly increased. Similar immunization with T-dependent antigens was coupled with the omental appearance of rapidly proliferating PCNA-positive and Bcl6-positive centroblasts and plasma cells undergoing affinity maturation and Ig isotype switch in a LTα-dependent manner also requiring CXCL13, but without the emergence of germinal centers and definable follicular dendritic cells [34,35]. Furthermore, in mice harboring OVA-specific TcR OTII CD4^{+} T cells the immunization with their cognate antigen could also induce their rapid proliferation and the appearance of CD8^{+} OVA-specific T cells, indicating the capacity of omental microenvironment to support T-cell immune responses as well [34].

2.2. FALCs in the peritoneal cavity

More recently, fat-associated lymphoid clusters (FALCs) were first identified by Moro et al. in the mesentery [36], and also in other locations such as mediastinal, pericardial and gonadal fat [5,37]. On HE stained sections, FALCs are located in visceral white adipose tissue, or have a close relationship with it [6]. FALCs were first identified in the mesenteries in mice and humans as loose structures attaching to the nearby adipose tissue [36]. They contain B cells, T cells, macrophages and several other innate lymphoid cells playing important roles in the local immune challenges. In mesenteric FALCs, B220^{+} or IgM^{+} B cells, CD4^{+} T cells and CD11b^{+} myeloid cells are observed with no distinguishable pattern [5,36]. FALCs show high-level expression of IL-5 in GATA-3-dependent type 2 innate lymphoid cells (ILC2) which support

B1 cell proliferation [36], whereas FALC formation is independent from RORγt-dependent type 3 ILC cells [38]. Considering their similar structural features and cellular composition, it is feasible to consider omental MSs and mesenteric FALCs as the same type of adipose lymphoid tissues, thus justifiably designating them as omental and mesenteric FALCs, respectively [39].

The adipose tissue location and the small size of FALCs pose substantial obstacles to their identification and analysis. An effective approach for their structural assessment is via whole-mount staining. Various adipose tissues were analyzed by this technique, revealing differences in FALC content, showing that the pericardium harbors most lymphoid clusters [5]. FALCs are arranged around capillaries lined by CD31$^+$ endothelium, and contain abundant B cells (including B1 cells), few T cells and myeloid cells. However, LYVE-1$^+$ lymphatics were not detected [5], while CXCL13$^+$ stromal cells with elongated appearance were identified within FALCs [5]. As discussed above, CXCL13 is important for recruiting B cells in FALCs [5,9]. As crucial morphogenic cytokines, TNF and LTβ are highly expressed in FALCs [5].

The initiation of FALC formation requires type 2 ILCs (ILC2), and it partially depends on TNF signaling, which can be augmented by peritoneal inflammation [5]. Macrophages are the main source of TNF, eliciting TNFR-mediated signals in radiation-resisted stromal cells which, together with NKT cells, play an important role in FALCs formation in which IL-4Rα signaling is also required [5]. Following the STAT5-directed commitment of common lymphoid progenitors (CLP) and stepwise maturation influenced by IL-7 and Notch signaling in the fetal liver, the mesenteric maturation of ILC2 cells is supported by platelet-derived growth factor receptor α (PDGFRα)-positive mesenchymal cells coexpressing gp38 stromal marker [40]. In addition, mesothelial cells as well as fibroblastic cells may jointly influence macrophage organization of FALCs in a Wilms tumor-1 (Wt1) transcription factor – retinaldehyde (RA, generated by RA dehydrogenases 1 and 2 [Raldh1/2], and recognized by RARβ) – GATA-6 regulatory circuit, also affecting local IgA isotype switch and RA-supported enhancement of intestinal homing of B1 cells [41–44].

Omental and mesenteric FALCs are structurally similar; however, omental FALCs show evidences for T/B cell segregation [36]. Normally, the number and size of FALC is dependent on the age of the individual [36]. Mesenteric FALCs contain a substantial number of Lin$^-$ c-Kit$^+$ Sca-1$^+$ ILC2 cells, whereas omental FALCs harbor only a few [36].

In a manner similar to the effects of peritoneal challenges, the pleural inflammation induced by *Litomosoides sigmodontis*, a rodent parasite stimulates local FALCs, leading to the activation and expansion of antigen-specific B cells and differentiation into CD138$^+$ plasma cells secreting antigen-specific IgM [7]. This process was largely dependent on IL-33, with B1a cells being relatively resistant to the absence of IL-33. IL-33 is produced by several cell types residing in FALCs, including gp38/podoplanin$^+$ fibroblastic reticular (FRC) stromal cells and perivascular white adipose-associated multipotential stromal cells (WAT-MSC) (identified as FAP$^+$, CD90$^+$, podoplanin$^+$, CD29$^+$, CD73$^+$, CD34$^+$, Sca1/Ly6a$^+$, CD63$^+$, vimentin$^+$). In addition to supplying IL-33, ICAM-1 on WAT-MSCs can bind to LFA-1 expressed by ILC2 cells, leading to their activation. In a bidirectional manner, these WAT-MSCs receive IL-4/IL-13 stimuli from ILC2 cells and, as a result can produce substantial amount of CCL11/eotaxin, to attract eosinophil granulocytes [45]. Pleural ILC2 cells also produce IL-5 for supporting B1a cells [7]. It remains to be seen whether similar processes also occur in omental or mesenteric FALCS [46,47].

The ILC2 pool in mesenteric FALCs is an important source of type 2 cytokines in the peritoneal cavity [36]. IL17 plays a role in the differentiation of type 2 ILCs in mesenteric FALCs, and together with stem cell factor (SCF/c-Kit ligand) it promotes the survival of ILC2 cells, supporting B1 cell division. Interestingly, in the peritoneal FALCs another regulatory circuit for the FRCs has recently been identified. Signaling through TLR9 appears to reduce the expression of mRNA for several chemokines (Cxcl2 and Cxcl5 for attracting neutrophils; Cxcl3 and Ccl2

for monocytes; Ccl19 and Ccl2 for DCs; Cxcl13 for B cells, Ccl19 and Ccl21 for T cells, respectively) by FALC-resident fibroblastic cells. The substantially reduced level of CXCL13 cytokine led to fewer B1 cells and blunted peritoneal protection. As a result, the fewer peritoneal B1 cells caused a reduced local production of GM-CSF, thus also affecting macrophage and neutrophil phagocytosis and removal of bacteria, in addition to their reduced peritoneal recruitment following TLR9 stimulation. Intraperitoneal transfer of *Tlr9$^{-/-}$* FRCs could augment the defense against peritoneal bacterial infections, raising their potential therapeutic use in septic conditions following abdominal infections [12]. Neutrophil release of neutrophil extracellular traps (NETs) expands their ability to trap abdominal contaminants & metastatic cells [11,48].

The significance of stromal regulation of FALC functions was further demonstrated by the impact of MYD88-dependent activation of FRCs in promoting the omental FALCs' potential to mount local humoral immune responses. Stimulation with S. typhi-derived outer membrane proteins C and F as antigen is followed by both T-dependent and T-independent immune responses, and remodeling of omental FALCs, including the accumulation of myeloid cells in a TNF-dependent manner and the expansion of a select FALC-associated FRC subset producing CCL19, thus allowing the specific manipulation of this stromal subset [13,49]. Selective Ccl19:Cre-mediated ablation of MYD88 in FALC FRCs abrogated the bacterial antigen-induced FALC transformation, possibly via preventing the upregulation of several chemokines. Moreover, although MYD88-depletion did not influence the amount of antigen-specific IgM-secreting cells, it reduced the number of Fas$^+$/GL7$^+$ centroblast-like cells and antigen-specific IgG-secreting plasma cells [13,49].

The schematic diagram in Fig. 1. summarizes the composition, cellular interactions and main molecular mediators in FALC formation.

2.3. FLAgs – partially organized adipose-associated lymphoid docking sites

The typical morphological appearance of omental or mesenteric FALCs suggests a similar diffuse leukocyte accumulation. In a serendipitous observation during a study of peritoneal metastasis of a spontaneous high-grade B-cell lymphoma [50] in mouse, we observed a sharply demarcated dense collection of lymphocytes, attached to the omentum, mesentery and the peritoneal ligaments forming the omental bursa. These structures attach to either the adipose tissue (as singles) or peritoneal ligaments (pairwise) via a stalk, and have an elongated architecture with a curved tip. Owing to these morphological characteristics, we named these sites as Foliate Lymphoid Aggregates (FLAgs), which have a more efficient capacity to immobilize lymphoma cells injected intraperitoneally as well as normal B cells then the FALCs [51]. Moreover, in both the omentum and mesentery we could observe crescent-shaped formations densely packed with lymphocytes, which we denote as protrusions. FLAgs are covered with mesothelial cells, and at the tip segment, a focal concentration of LYVE-1-positive macrophages can be observed. These cells appear to play an important role in immobilizing the lymphoma cells, as their removal by clodronate-containing liposomes significantly reduced the lymphoma binding to these structures. Importantly, T cells accumulate within the central regions, corresponding to the local presence of CCL21 chemokine, while B cells congregate at the peripheral rim together with the presence of CXCL13. These separate chemokine domains in FLAgs also selectively attract germinal center-derived CXCR5-positive A20 lymphoma cells and CCR7-positive extranodal Bc.DLFL1 lymphoma cells, whereas in either mesenteric or omental FALCs with diffuse organization such lymphoma subtype-selective segregation is absent. In addition, the FLAg body contains VCAM-1-positive stromal cells and an extensive meshwork of fibronectin. Their vascular connection includes blood vasculature with segmental PNAd expression mediating partly L-selectin-dependent lymphocyte homing from blood (Fig. 2), whereas
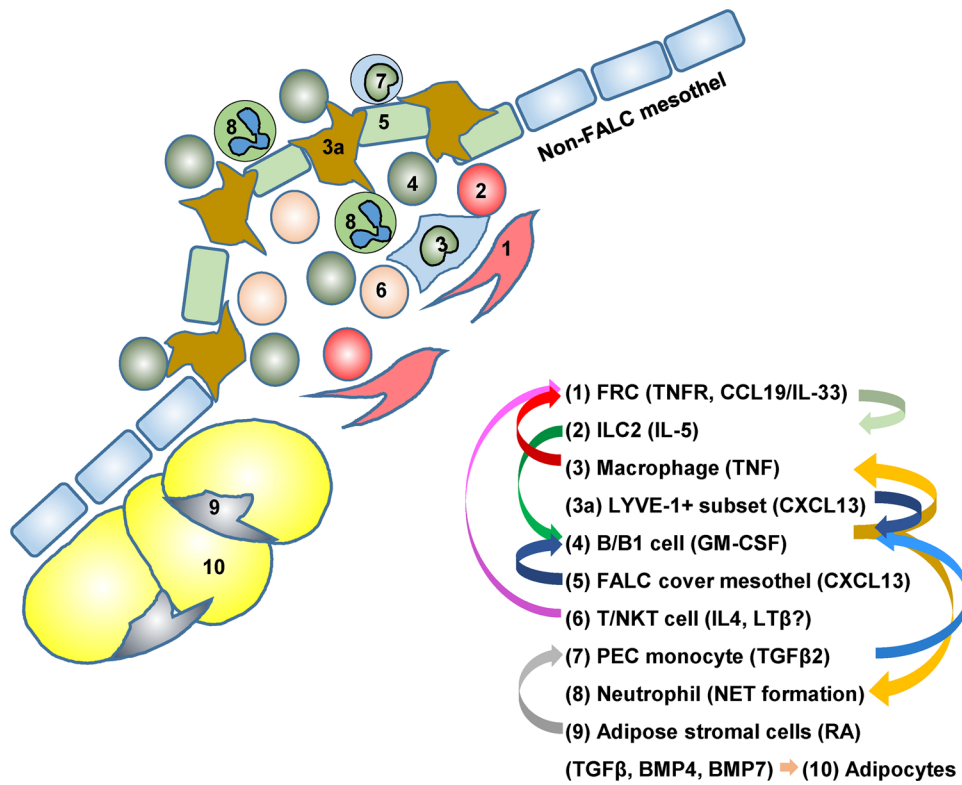
Fig. 1. Multiple cellular interactions and regulatory circuits between hematopoietic and stromal cells in FALC formation and local immune responses. Numbers indicate various cell types as denoted, soluble factors and receptors involved in the various cellular interactions are listed in brackets. For details please follow the text with references included.
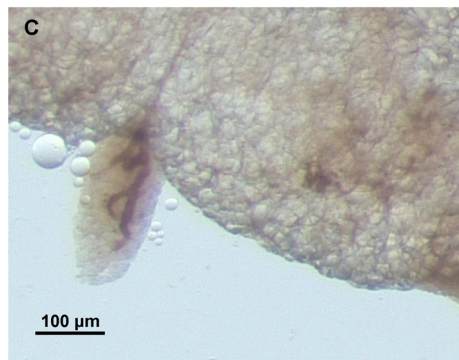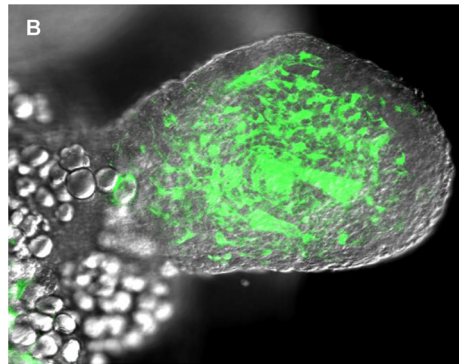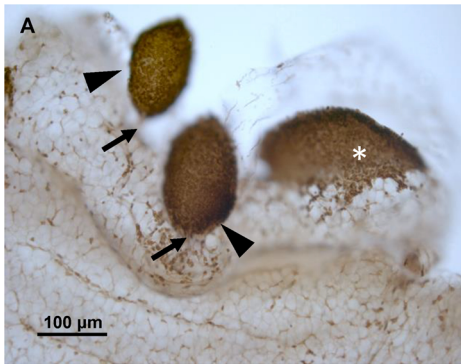

Fig. 2. Structural features of FLAgs.

(A) Mesenteric FLAgs (arrowheads) densely populated by leukocytes in mouse mesentery are sharply demarcated from the neighboring tissues, unlike the diffuse FALC (*), and are attached to the adipose tissue via stalks (arrows) and are densely populated by leukocytes. The adipose surface and attached peritoneal membranes contain CD45-dim macrophages (anti-CD45 immunohistochemical staining with DAB/H_2O_2 detection in whole-mount, brown color).

(B) FLAGs contain an extensive stromal-vascular scaffolding, observed in hematopoietic chimeras using wild-type bone marrow transplanted into irradiated eGFP-positive recipients, with eGFP expression restricted to radiation-resistant stroma (confocal fluorescence microscopy image combined with differential interference contrast [DIC] imaging).

(C) The vasculature of FLAgs includes vascular segments lined by PNAd-positive endothelial cells (MECA-79 anti-PNAd labeling of whole-mount with DAB/H_2O_2 detection, brown reaction product).

lymphatic vessels were not detectable, thus the route of dissemination from FLAgs towards the mesenteric lymph nodes is yet unknown [51]. The specific immunological functions of FLAgs beyond lymphocyte docking sites and their existence in other species require further studies.

3. Adipose-associated stem cells, tissue regeneration and tumor propagation – hidden treasures or clear and present dangers?

In addition to serving as an energy depot and hosting lymphoid organoids as direct responders for local immunological stimuli, the visceral adipose tissues also possess a remarkable potential for tissue regeneration. One existing differentiation event is manifested in peritoneal dialysis patients, demonstrating excessive fibroblast expansion resulting in fibrosis. Using in vitro fluid stress models in explant tissues containing mesothelial cells and endothelium the adipose compartment gives rise to adipose stem cells (ASCs) with the potential to expand the visceral adipocyte load; however, in this in vitro model no adipose-derived mesenchymal stem cells (MSCs) were identified [52]. On the other hand, in vivo allogeneic transplantation with adipose derived multilineage progenitor cells (ADMPC) from the omentum enabled a successful periodontal regeneration, comparable to MSC-mediated regeneration, also illustrating the immunosuppressive capacity of omental ADMPCs to promote the acceptance of histoincompatible host tissue [53]. Furthermore, in a xenogeneic model, human MSCs injected intraperitoneally into immunocompetent mouse recipients formed multicellular complexes with peritoneal B cells and macrophages, and subsequently firmly adhered to omental and mesenteric FALCs [54]. In addition, the embedded human MSCs exerted a potent recruitment of mouse B cells and macrophages. Thus, on one hand, the omental adipose tissue can supply MSCs and functionally equivalent ADMPCs for connective tissue remodeling; on the other hand, MSCs can specifically be directed to preferential docking within FALCs. The stromal-vascular fraction (SVF) could also generate adherent cells defined as ASCs, which could form vascular structures. Following high-density seeding in fibrin scaffold, and after being transplanted into SCID mice, in these aggregates increased vascular formation occurred [15,55]. These findings reveal that the local cell/tissue differentiation potential of the abdominal visceral adipose tissues extends beyond supporting the MSC-adipocyte-fibroblast transformation triangle.

While the omental sequestration of peritoneal inflammatory agents has been appreciated as a beneficial feature, infiltration of the mesentery by various gastrointestinal tumors, urinary bladder or ovary cancer has been considered a fatal complication of disease progression. Upon injection of various human ovary carcinoma cell lines into immunodeficient mice, cancer cells were found to accumulate in omental and abdominal MSs regions, followed by the gradual wasting of recipient adipose content accompanied with the local growth of cancer, thus playing complementary roles in initial tumor adhesion and subsequent expansion [56]. In addition, in vitro studies confirmed the existence of omental adipose-derived mesenchymal stem cells that could promote the growth of ovary cancer cells by inducing chemoresistance, enhanced migration and radiation resistance as well [57].

As potential partner cells for FALC-directed adhesion of cancer cells, recent studies indicated an enhanced neutrophil influx in premetastatic stage, and NET formation in the FALC regions, followed by the efficient binding of carcinoma cells. Here the NET formation is induced by yet unidentified soluble products of the cancer cells. Following prevention of NET formation by anti-Ly6G antibody-mediated depletion of granulocytes or in mice with neutrophil-specific deficiency of peptidylarginine deiminase 4 (PAD4), an enzyme required for NET formation, the FALC-directed cancer cell metastasis was blocked without interfering with the tumor growth at the site of inoculation [48]. In addition to the ovary cancer model, EL4 T-cell lymphoma cells were also found to be able to bind to omental and mesenteric FALCs, in which the binding was independent from pertussis toxin (Ptx) sensitive G-protein coupled signaling, but subsequent clustering could be blocked by treating the

cells with Ptx [34]. In our studies, we found that both A20 follicular diffuse large B-cell (DLBCL) and Bc.DLFL1 extafollicular DLBCL lymphoma cells can bind to omental and mesenteric lymphoid clusters [51]. These data indicate that, in addition to hosting various multicellular lymphoid tissue formations, omental and mesenteric adipose tissue can provide a supportive microenvironment for mesenchymal trans-differentiation, potentially resulting in MSC-like cells with immuno-suppressive capacity, as well as tumor-supportive conditions including adhesive and chemotactic influences for tumor cell binding and subsequent positioning of both hematopoietic and solid tissue tumors. Further studies are necessary to determine how the adipose tissues' capacity to generate potentially immunosuppressive MSCs (coupled with serving as energy source for tumor cells from fat depots) can be antagonized with the efficient stimulation of serosal lymphoid organoids to shield preformed sites from potential tumor dissemination and eliminate peritoneal metastatic foci.

4. Concluding remarks

Due to their unique location, omental and mesenteric lymphoid organs are at the crossroads between the visceral adipose tissues and secondary lymphoid tissues, although with incomplete tissue architecture. Despite their rudimentary organization, they can expand and adapt to immunological challenges, incorporating ILC2-derived cytokines, and providing stromal support to facilitate leukocyte movement and positioning. Local myeloid cells contribute to promote the TNF-mediated development of FALCs. In addition, these lymphoid tissues can simultaneously be influenced by adipose tissue resident mesenchymal stem cells and progenitors. The unique tissue organization of intraabdominal adipose-associated lymphoid tissues combines preformed adhesion sites for peritoneal propagations of tumors, thus posing a considerable challenge for preserving their immunological competence and harness their tumor niche potential.

Declaration of Competing Interest

The authors declare that they have no known competing financial interests or personal relationships that could have appeared to influence the work reported in this paper.

Acknowledgements

References

[1] H. Veiga-Fernandes, M.C. Coles, K.E. Foster, A. Patel, A. Williams, D. Natarajan, A. Barlow, V. Pachnis, D. Kioussis, Tyrosine kinase receptor RET is a key regulator of Peyer's patch organogenesis, Nature 446 (7135) (2007) 547–551, https://doi.org/10.1038/nature05597.

[2] T. Sminia, G.J. van der Brugge-Gamelkoorn, S.H. Jeurissen, Structure and function of bronchus-associated lymphoid tissue (BALT), Crit. Rev. Immunol. 9 (2) (1989) 119–150.

[3] R.G. Lorenz, R.D. Newberry, Isolated lymphoid follicles can function as sites for induction of mucosal immune responses, Ann. N. Y. Acad. Sci. 1029 (2004) 44–57, https://doi.org/10.1196/annals.1309.006.

[4] N.H. Ruddle, E.M. Akirav, Secondary lymphoid organs: responding to genetic and environmental cues in ontogeny and the immune response, J. Immunol. 183 (2009) 2205–2212, https://doi.org/10.4049/jimmunol.0804324.

[5] C. Bénézech, N. Luu, J.A. Walker, A.A. Kruglov, A. Mcintosh, J. Marshall, F. Barone, D.R. Withers, K.M. Toellner, N.D. Jones, M. Veldhoen, Europe PMC Funders Group, Inflammation-induced formation of fat-associated lymphoid clusters, Nat. Immunol. 16 (2016) 819–828, https://doi.org/10.1038/ni.3215. Inflammation-induced.

[6] L. Wu, R. Dalal, C.D. Cao, J.L. Postoak, G. Yang, Q. Zhang, Z. Wang, H. Lal, L. van Kaer, IL-10–producing B cells are enriched in murine pericardial adipose tissues and ameliorate the outcome of acute myocardial infarction, Proc. Natl. Acad. Sci. U. S. A. 116 (2019) 21673–21684, https://doi.org/10.1073/pnas.1911464116.

[7] L.H. Jackson-Jones, S.M. Duncan, M.S. Magalhaes, S.M. Campbell, R.M. Maizels, H. J. McSorley, J.E. Allen, C. Bénézech, Fat-associated lymphoid clusters control local IgM secretion during pleural infection and lung inflammation, Nat. Commun. 7 (2016), https://doi.org/10.1038/ncomms12651.

[8] I. Negri, E. Diaz Villamil, L. De Roeck, D. Communi, M. Horckmans, P2Y $_2$ nucleotide receptor is a regulator of the formation of cardiac adipose tissue and its fat-associated lymphoid clusters, Stem Cells Dev. 29 (2020) 100–109, https://doi. org/10.1089/scd.2019.0200.

[9] K.M. Ansel, R.B.S. Harris, J.G. Cyster, CXCL13 is required for B1 cell homing, natural antibody production, and body cavity immunity, Immunity 16 (2002) 67–76, https://doi.org/10.1016/S1074-7613(01)00257-6.

[10] S.A. Ha, M. Tsuji, K. Suzuki, B. Meek, N. Yasuda, T. Kaisho, S. Fagarasan, Regulation of B1 cell migration by signals through Toll-like receptors, J. Exp. Med. 203 (2006) 2541–2550, https://doi.org/10.1084/jem.20061041.

[11] L.H. Jackson-Jones, P. Smith, J.R. Portman, M.S. Magalhaes, K.J. Mylonas, M. M. Vermeren, M. Nixon, B.E.P. Henderson, R. Dobie, S. Vermeren, L. Denby, N. C. Henderson, D.J. Mole, C. Bénézech, Stromal cells covering omental fat-associated lymphoid clusters trigger formation of neutrophil aggregates to capture peritoneal contaminants, Immunity 52 (2020) 700–715, https://doi.org/10.1016/ j.immuni.2020.03.011, e6.

[12] L. Xu, Y. Li, C. Yang, P. Loughran, H. Liao, R. Hoffman, T.R. Billiar, M. Deng, TLR9 signaling in fibroblastic reticular cells regulates peritoneal immunity, J. Clin. Invest. 129 (9) (2019) 3657–3669, https://doi.org/10.1172/JCI127542.

[13] C. Perez-Shibayama, C. Gil-Cruz, H.W. Cheng, L. Onder, A. Printz, U. Mörbe, M. Novkovic, C. Li, C. Lopez-Macias, M.B. Buechler, S.J. Turley, M. Mack, C. Soneson, M.D. Robinson, E. Scandella, J. Gommerman, B. Ludewig, Fibroblastic reticular cells initiate immune responses in visceral adipose tissues and secure peritoneal immunity, Sci. Immunol. 3 (26) (2018), https://doi.org/10.1126/ sciimmunol.aar4539 eaar4539.

[14] F. Abo-Aziza, A.A. Zaki, The impact of confluence on bone marrow mesenchymal stem (BMMSC) proliferation and osteogenic differentiation, Int. J. Hematol. Stem Cell Res. 11 (2) (2017) 121–132.

[15] D.D. Manavella, L. Cacciottola, C.M. Desmet, B.F. Jordan, J. Donnez, C.A. Amorim, M.M. Dolmans, Adipose tissue-derived stem cells in a fibrin implant enhance neovascularization in a peritoneal grafting site: a potential way to improve ovarian tissue transplantation, Hum. Reprod. 33 (2018) 270–279, https://doi.org/ 10.1093/humrep/dex374.

[16] S. Aoki, K. Udo, H. Morimoto, S. Ikeda, T. Takezawa, K. Uchihashi, A. Nishijima-Matsunobu, M. Noguchi, H. Sugihara, S. Toda, Adipose tissue behavior is distinctly regulated by neighboring cells and fluid flow stress: a possible role of adipose tissue in peritoneal fibrosis, J. Artif. Organs 16 (2013) 322–331, https://doi.org/ 10.1007/s10047-013-0702-8.

[17] D. Frasca, B.B. Blomberg, Adipose Tissue: A Tertiary Lymphoid Organ: Does It Change with Age? Gerontology 66 (2) (2020) 114–121, https://doi.org/10.1159/ 000502036.

[18] L.C. Davies, S.J. Jenkins, J.E. Allen, P.R. Taylor, Tissue-resident macrophages, Nat. Immunol. 14 (2013) 986–995, https://doi.org/10.1038/ni.2705.

[19] C.N. Lumeng, J.L. Bodzin, A.R. Saltiel, Obesity induces a phenotypic switch in adipose tissue macrophage polarization, J. Clin. Invest. 117 (1) (2007) 175–184, https://doi.org/10.1172/JCI29881. https://www.jci.org/articles/view/29881.

[20] S. Boulenouar, X. Michelet, D. Duquette, D. Alvarez, A.E. Hogan, C. Dold, D. O'Connor, S. Stutte, A. Tavakkoli, D. Winters, M.A. Exley, D. O'Shea, M. B. Brenner, U. von Andrian, L. Lynch, Adipose type one innate lymphoid cells regulate macrophage homeostasis through targeted cytotoxicity, Immunity 46 (2) (2017) 273–286, https://doi.org/10.1016/j.immuni.2017.01.008.

[21] A. Weinstock, H. Moura Silva, K.J. Moore, A.M. Schmidt, E.A. Fisher, Leukocyte heterogeneity in adipose tissue, including in obesity, Circ. Res. 126 (11) (2020) 1590–1612, https://doi.org/10.1161/CIRCRESAHA.120.316203.

[22] C. Bénézech, E. Mader, G. Desanti, M. Khan, K. Nakamura, A. White, C.F. Ware, G. Anderson, J.H. Caamaño, Lymphotoxin-β receptor signaling through NF-κB2-RelB pathway reprograms adipocyte precursors as lymph node stromal cells, Immunity 37 (4) (2012) 721–734, https://doi.org/10.1016/j. immuni.2012.06.010.

[23] A. Lovas, D. Radke, D. Albrecht, Z.B. Yilmaz, U. Möller, A.J. Habenicht, F. Weih, Differential RelA- and RelB-dependent gene transcription in LTbetaR-stimulated mouse embryonic fibroblasts, BMC Genomics 9 (2008) 606, https://doi.org/ 10.1186/1471-2164-9-606.

[24] J.C. Hall, K.A. Heel, J.M. Papadimitriou, C. Platell, The pathobiology of peritonitis, Gastroenterology 114 (1) (1998) 185–196, https://doi.org/10.1016/s0016-5085 (98)70646-8.

[25] A.E. Hertzler, The omentum, J. Am. Med. Assoc. 86 (1926) 1785, https://doi.org/ 10.1001/jama.1926.02670490047029.

[26] M.E. Fedorko, J.G. Hirsch, Studies on transport of macromolecules and small particles across mesothelial cells of the mouse omentum. I. Morphologic aspects, Exp. Cell Res. 69 (1) (1971) 113–127, https://doi.org/10.1016/0014-4827(71) 90317-x.

[27] S.A. Gerber, V.Y. Rybalko, C.E. Bigelow, A.A. Lugade, T.H. Foster, J.G. Frelinger, E. M. Lord, Preferential attachment of peritoneal tumor metastases to omental immune aggregates and possible role of a unique vascular microenvironment in metastatic survival and growth, Am. J. Pathol. 169 (5) (2006) 1739–1752, https:// doi.org/10.2353/ajpath.2006.051222.

[28] C. Hodel, Ultrastructural studies on the absorption of protein markers by the greater omentum, Eur. Surg. Res. 2 (6) (1970) 435–449, https://doi.org/10.1159/ 000127543.

[29] S. Berberich, S. Dähne, A. Schippers, T. Peters, W. Müller, E. Kremmer, R. Förster, O. Pabst, Differential molecular and anatomical basis for B cell migration into the peritoneal cavity and omental milky spots, J. Immunol. 180 (4) (2008) 2196–2203, https://doi.org/10.4049/jimmunol.180.4.2196.

[30] S. Avrameas, T. Ternynck, Natural autoantibodies: the other side of the immune system, Res. Immunol. 146 (4–5) (1995) 235–248, https://doi.org/10.1016/0923-2494(96)80259-8.

[31] S. Berberich, R. Förster, O. Pabst, The peritoneal micromilieu commits B cells to home to body cavities and the small intestine, Blood 109 (11) (2007) 4627–4634, https://doi.org/10.1182/blood-2006-12-064345.

[32] A. Lábadi, P. Balogh, Differential preferences in serosal homing and distribution of peritoneal B-cell subsets revealed by in situ CFSE labeling, Int. Immunol. 21 (9) (2009) 1047–1056, https://doi.org/10.1093/intimm/dxp071.

[33] J. Palming, B.G. Gabrielsson, E. Jennische, U. Smith, B. Carlsson, L.M. Carlsson, M. Lönn, Plasma cells and Fc receptors in human adipose tissue–lipogenic and anti-inflammatory effects of immunoglobulins on adipocytes, Biochem. Biophys. Res. Commun. 343 (1) (2006) 43–48, https://doi.org/10.1016/j.bbrc.2006.02.114.

[34] J. Rangel-Moreno, J.E. Moyron-Quiroz, D.M. Carragher, K. Kusser, L. Hartson, A. Moquin, T.D. Randall, Omental milky spots develop in the absence of lymphoid tissue-inducer cells and support B and T cell responses to peritoneal antigens, Immunity 30 (5) (2009) 731–743, https://doi.org/10.1016/j. immuni.2009.03.014.

[35] J.S. Weinstein, D.C. Nacionales, P.Y. Lee, K.M. Kelly-Scumpia, X.J. Yan, P. O. Scumpia, D.S. Vale-Cruz, E. Sobel, M. Satoh, N. Chiorazzi, W.H. Reeves, Colocalization of antigen-specific B and T cells within ectopic lymphoid tissue following immunization with exogenous antigen, J. Immunol. 181 (5) (2008) 3259–3267, https://doi.org/10.4049/jimmunol.181.5.3259.

[36] K. Moro, T. Yamada, M. Tanabe, T. Takeuchi, T. Ikawa, H. Kawamoto, J. Furusawa, M. Ohtani, H. Fujii, S. Koyasu, Innate production of T(H)2 cytokines by adipose tissue-associated c-Kit(+)Sca-1(+) lymphoid cells, Nature 463 (7280) (2010) 540–544, https://doi.org/10.1038/nature08636.

[37] Y.H. Elewa, O. Ichii, S. Otsuka, Y. Hashimoto, Y. Kon, Characterization of mouse mediastinal fat-associated lymphoid clusters, Cell Tissue Res. 357 (3) (2014) 731–741, https://doi.org/10.1007/s00441-014-1889-6.

[38] T. Nagatake, S. Fukuyama, D.Y. Kim, K. Goda, O. Igarashi, S. Sato, T. Nochi, H. Sagara, Y. Yokota, A.M. Jetten, T. Kaisho, S. Akira, H. Mimuro, C. Sasakawa, Y. Fukui, K. Fujihashi, T. Akiyama, J. Inoue, J.M. Penninger, J. Kunisawa, H. Kiyono, Id2-, RORgammat-, and LTbetaR-independent initiation of lymphoid organogenesis in ocular immunity, J. Exp. Med. 206 (11) (2009) 2351–2364, https://doi.org/10.1084/jem.20091436.

[39] S. Cruz-Migoni, J. Caamaño, Fat-associated lymphoid clusters in inflammation and immunity, Front. Immunol. 7 (2016) 612, https://doi.org/10.3389/ fimmu.2016.00612.

[40] S. Koga, K. Hozumi, K.I. Hirano, M. Yazawa, T. Terooatea, A. Minoda, T. Nagasawa, S. Koyasu, K. Moro, Peripheral PDGFRα+gp38+ mesenchymal cells support the differentiation of fetal liver-derived ILC2, J. Exp. Med. 215 (6) (2018) 1609–1626, https://doi.org/10.1084/jem.20172310.

[41] Y. Okabe, R. Medzhitov, Tissue-specific signals control reversible program of localization and functional polarization of macrophages, Cell 157 (4) (2014) 832–844, https://doi.org/10.1016/j.cell.2014.04.016.

[42] M.B. Buechler, K.W. Kim, E.J. Onufer, J.W. Williams, C.C. Little, C.X. Dominguez, Q. Li, W. Sandoval, J.E. Cooper, C.A. Harris, M.R. Junttila, G.J. Randolph, S. J. Turley, A stromal niche defined by expression of the transcription factor WT1 mediates programming and homeostasis of cavity-resident macrophages, Immunity 51 (1) (2019) 119–130, https://doi.org/10.1016/j.immuni.2019.05.010, e5.

[43] M. Rosas, L.C. Davies, P.J. Giles, C.T. Liao, B. Kharfan, T.C. Stone, V.B. O'Donnell, D.J. Fraser, S.A. Jones, P.R. Taylor, The transcription factor Gata6 links tissue macrophage phenotype and proliferative renewal, Science 344 (6184) (2014) 645–648, https://doi.org/10.1126/science.1251414.

[44] L.H. Jackson-Jones, C. Bénézech, FALC stromal cells define a unique immunological niche for the surveillance of serous cavities, Curr. Opin. Immunol. 64 (2020) 42–49, https://doi.org/10.1016/j.coi.2020.03.008. Advance online publication.

[45] B. Rana, E. Jou, J.L. Barlow, N. Rodriguez-Rodriguez, J.A. Walker, C. Knox, H. E. Jolin, C.S. Hardman, M. Sivasubramaniam, A. Szeto, E.S. Cohen, I.C. Scott, M. A. Sleeman, C.I. Chidomere, S. Cruz Migoni, J. Caamano, H.F. Jorgensen, S. Carobbio, A. Vidal-Puig, A. McKenzie, A stromal cell niche sustains ILC2-mediated type-2 conditioning in adipose tissue, J. Exp. Med. 216 (9) (2019) 1999–2009, https://doi.org/10.1084/jem.20190689.

[46] M. Rodbell, A.B. Jones, Metabolism of isolated fat cells. 3. The similar inhibitory action of phospholipase C (Clostridium perfringens alpha toxin) and of insulin on lipolysis stimulated by lipolytic hormones and theophylline, J. Biol. Chem. 241 (1) (1966) 140–142.

[47] L.D. Erickson, T.M. Foy, T.J. Waldschmidt, Murine B1 B cells require IL-5 for optimal T cell-dependent activation, J. Immunol. 166 (3) (2001) 1531–1539, https://doi.org/10.4049/jimmunol.166.3.1531.

[48] W. Lee, S.Y. Ko, M.S. Mohamed, H.A. Kenny, E. Lengyel, H. Naora, Neutrophils facilitate ovarian cancer premetastatic niche formation in the omentum, J. Exp. Med. 216 (1) (2019) 176–194, https://doi.org/10.1084/jem.20181170.

[49] C. Perez-Shibayama, C. Gil-Cruz, R. Pastelin-Palacios, L. Cervantes-Barragan, E. Hisaki, Q. Chai, L. Onder, E. Scandella, T. Regen, A. Waisman, A. Isibasi, C. Lopez-Macias, B. Ludewig, IFN-γ-producing CD4+ T cells promote generation of protective germinal center-derived IgM+ B cell memory against Salmonella typhi,

J. Immunol. 192 (11) (2014) 5192–5200, https://doi.org/10.4049/jimmunol.1302526.

[50] D. Vojkovics, Z. Kellermayer, D. Heidt, M. Mihalj, B. Kajtár, D. Ernszt, T. Kovács, P. Németh, P. Balogh, Isolation and characterization of a murine spontaneous high-grade follicular lymphoma with restricted in vivo spreading–a model for lymphatic metastasis via the mesentery, Pathol. Oncol. Res. 22 (2) (2016) 421–430, https://doi.org/10.1007/s12253-015-0025-6.

[51] X. Jia, F. Gábris, Ó. Jacobsen, G. Bedics, B. Botz, Z. Helyes, Z. Kellermayer, D. Vojkovics, G. Berta, N. Nagy, Z. Jakus, P. Balogh, Foliate lymphoid aggregates as novel forms of serous lymphocyte entry sites of peritoneal B cells and high-grade B cell lymphomas, J. Immunol. 204 (1) (2020) 23–36, https://doi.org/10.4049/jimmunol.1900851.

[52] S. Aoki, K. Udo, H. Morimoto, S. Ikeda, T. Takezawa, K. Uchihashi, A. Nishijima-Matsunobu, M. Noguchi, H. Sugihara, S. Toda, Adipose tissue behavior is distinctly regulated by neighboring cells and fluid flow stress: a possible role of adipose tissue in peritoneal fibrosis, J. Artif. Organs 16 (3) (2013) 322–331, https://doi.org/10.1007/s10047-013-0702-8.

[53] V.S. Venkataiah, K. Handa, M.M. Njuguna, T. Hasegawa, K. Maruyama, E. Nemoto, S. Yamada, S. Sugawara, L. Lu, M. Takedachi, S. Murakami, H. Okura, A. Matsuyama, M. Saito, Periodontal regeneration by allogeneic transplantation of adipose tissue derived multi-lineage progenitor stem cells in vivo, Sci. Rep. 9 (1) (2019) 921, https://doi.org/10.1038/s41598-018-37528-0.

[54] N. Bazhanov, J.H. Ylostalo, T.J. Bartosh, A. Tiblow, A. Mohammadipoor, A. Foskett, D.J. Prockop, Intraperitoneally infused human mesenchymal stem cells form aggregates with mouse immune cells and attach to peritoneal organs, Stem Cell Res. Ther. 7 (2016) 27, https://doi.org/10.1186/s13287-016-0284-5.

[55] F. De Francesco, V. Tirino, V. Desiderio, G. Ferraro, F. D'Andrea, M. Giuliano, G. Libondi, G. Pirozzi, A. De Rosa, G. Papaccio, Human CD34/CD90 ASCs are capable of growing as sphere clusters, producing high levels of VEGF and forming capillaries, PLoS One 4 (8) (2009) e6537, https://doi.org/10.1371/journal.pone.0006537.

[56] R. Clark, V. Krishnan, M. Schoof, I. Rodriguez, B. Theriault, M. Chekmareva, C. Rinker-Schaeffer, Milky spots promote ovarian cancer metastatic colonization of peritoneal adipose in experimental models, Am. J. Pathol. 183 (2) (2013) 576–591, https://doi.org/10.1016/j.ajpath.2013.04.023.

[57] A. Nowicka, F.C. Marini, T.N. Solley, P.B. Elizondo, Y. Zhang, H.J. Sharp, R. Broaddus, M. Kolonin, S.C. Mok, M.S. Thompson, W.A. Woodward, K. Lu, B. Salimian, D. Nagrath, A.H. Klopp, Human omental-derived adipose stem cells increase ovarian cancer proliferation, migration, and chemoresistance, PLoS One 8 (12) (2013) e81859, https://doi.org/10.1371/journal.pone.0081859.

Age-Associated B Cell Features of the Murine High-Grade B Cell Lymphoma Bc.DLFL1 and Its Extranodal Expansion in Abdominal Adipose Tissues

Xinkai Jia,[*,†] Judit Bene,[‡] Noémi Balázs,[*] Katalin Szabó,[*] Gergely Berta,[§] Róbert Herczeg,[¶] Attila Gyenesei,[¶] and Péter Balogh[*,†]

Diffuse large B cell lymphoma comprises a heterogeneous group of B cell–derived tumors, with different degrees of aggressiveness, as defined by their cellular origin and tissue microenvironment. Using the spontaneous Bc.DLFL1 lymphoma originating from a BALB/c mouse as a diffuse large B cell lymphoma model, in this study we demonstrate that the lymphoma cells display surface phenotype, IgH V-region somatic mutations, transcription factor characteristics and in vivo location to splenic extrafollicular regions of age-associated B cells (ABCs), corresponding to T-bet^{+} and Blimp-1^{+}/CD138^{−} plasmablasts derivation. The expansion of lymphoma cells within lymphoid tissues took place in a close arrangement with CD11c^{+} dendritic cells, whereas the extranodal infiltration occurred selectively in the mesentery and omentum containing resident gp38/podoplanin^{+} fibroblastic reticular cells. Antagonizing BAFF-R activity by mBR3-Fc soluble receptor fusion protein led to a significant delay of disease progression. The extranodal expansion of Bc.DLFL1 lymphoma within the omental and mesenteric adipose tissues was coupled with a significant change of the tissue cytokine landscape, including both shared alterations and tissue-specific variations. Our findings indicate that while Bc.DLFL1 cells of ABC origin retain the positioning pattern within lymphoid tissues of their physiological counterpart, they also expand in non-lymphoid tissues in a BAFF-dependent manner, where they may alter the adipose tissue microenvironment to support their extranodal growth. *The Journal of Immunology*, 2022, 208: 1–11.

Crucial roles are played by B cells in the humoral immune responsiveness in vertebrates, and these cells are subjects of an extensive array of influences, which determine their differentiation from mature naive B cells into Ab-secreting effector cells (1, 2). Following antigenic stimuli, resting naive B cells initiate robust proliferation and signal-dependent specification along memory B cells or plasmacytes, as defined by their lymphoid and stromal microenvironmental cues and transcriptional preferences (2–4).

In addition, B cells themselves can also exert immunoregulatory functions via secretion of a broad variety of cytokines. By producing various members of the lymphotoxin/TNF cytokine family, B cells promote the differentiation of their lymphoid tissue microenvironment (5, 6). Furthermore, via the secretion of regulatory IL-10, IL-35, and TGF-β (7–9) or IL-3 and GM-CSF affecting myeloid cells (10, 11), B cells can also influence both adaptive and innate leukocytes during immune responses. These B cell subpopulations with particular functional specifications have different origins (B2 cells with regulatory activities and B1 lymphocytes promoting innate-type responses,

respectively), and they typically constitute heterogeneous subsets, as defined by their cell surface phenotypes (12, 13).

While the actual Ag exposure of B cells significantly shapes the peripheral B cell pool, the process of aging can also alter the humoral immune responsiveness, including increased susceptibility to infections, autoimmunity, and lymphoproliferation associated with the expansion of age-associated B cells (ABCs) (12, 14–16). As described recently in more detail in mice, the ABC subset of Ag-experienced/memory B cells lacking CD21 and CD23 displays CD11b and CD11c, produces the T-bet transcription factor (16), and is responsible for autoantibody production in systemic lupus erythematosus–prone mice (17). In wild-type mice, CD11c^{+}/T-bet^{hi} ABCs accumulate in the spleen, where they are located in the border area between the T cell/B cell compartments (18, 19). Their differentiation involves a complex innate/cytokine regulation circuit between TLR ligands for TLR7 and TLR9, together with IL-21, IFN-γ, and IL-4, that induce T-bet expression and CD11c, although ABC-like functional equivalents may develop without T-bet activity (20). The IL-21–dependent differentiation of ABCs is balanced by the activity of SWEF RhoGTPase family members DEF6

*Department of Immunology and Biotechnology, Clinical Center, University of Pécs, Pécs, Hungary; †Lymphoid Organogenesis Research Group, Szentágothai Research Center, University of Pécs, Pécs, Hungary; ‡Department of Medical Genetics, Clinical Center, University of Pécs, Pécs, Hungary; §Department of Medical Biology and Central Electron Microscope Laboratory, Medical School, University of Pécs, Pécs, Hungary; and ¶Bioinformatics Research Group, Szentágothai Research Center, University of Pécs, Pécs, Hungary

ORCID: 0000-0001-6569-3862 (K.S.).

and SWAP-70 through IFN regulatory factor 5 (IRF5), as their absence results in expansion of the ABC pool and increased autoantibody production (21). The accumulation of ABCs leads to perturbed splenic germinal center (GC) reactions in murine lupus models where, despite the increased Ag-presenting capacity of ABCs through the excessive formation of follicular T helper cells, the GC affinity selection of centroblasts is impaired (22). This connection involving ABCs highlights the close relationship between the propensity of aged individuals for systemic autoimmunity and lymphoproliferation, ultimately leading to certain forms of B cell malignancies.

The most frequent B cell lymphoma type is the diffuse large B cell lymphoma (DLBCL), comprised of highly diverse cellular–morphological variants, genetic subtypes, and clinical courses. In addition to these pathogenetic complexities, DLBCLs of GC B cell origin and other, more aggressive forms of non-Hodgkin's lymphoma associate more often and with a wider spectrum of systemic and organ-specific autoimmune diseases than do other B cell lymphoma subtypes, including follicular lymphoma (23–25). Given the probable involvement of the ABC subset in the promotion of autoimmune conditions and their increase during aging, it is noteworthy that the lymphoma-generating potential of ABCs themselves—not to be confused with the activated B cell derivation variant of DLBCL, also abbreviated as ABC—has not yet been investigated.

In this study, we found that a recently isolated spontaneous DLBCL line Bc.DLFL1 (26) from a BALB/c mouse possessing plasmablast-like features has a remarkable similarity to the ABC subset, including cell surface phenotype, chemokine receptor pattern, and T-bet expression, associated with the production of Blimp-1, as well as similar in vivo lymphoid tissue location preference and Ig gene alterations. Furthermore, we also describe the cytokine landscape alterations associated with the extranodal expansion of these lymphoma cells in visceral adipose sites containing a fibroblastic reticular cell (FRC) meshwork, as well as the inhibitory effect of BAFF-R modulation in vivo. This lymphoma cell line may be a valuable tool for the analysis of ABC-derived B cell lymphoid malignancies.

Materials and Methods

Mice

Eight- to 10-wk-old BALB/c mice and BALB/c^{eGFP} transgenic (Tg) mice (27) were obtained from our departmental specific pathogen-free unit, and were kept under minimal disease conditions and fed with pelleted food and water ad libitum, with 12-h dark/12-h light cycles. The BcDLFL.1 lymphoma cells were propagated by serial i.p. passages of suspension prepared from lymphoma-infiltrated mesenteric lymph nodes (mLNs) as described earlier (26). All procedures involving live mice were performed in accordance with the Ethics Committee on Animal Experimentation (University of Pécs, Pécs, Hungary) under license number BA02/2000-16/2015.

mAbs and other immunoreagents

Monoclonal IgGs produced by anti-B220 hybridoma (clone RA3-6B2), anti-mouse CD3 (clone KT-3), and anti-mouse CD19 (clone 1D3) were purified from hybridoma supernatant by protein G chromatography and conjugated with Alexa Fluor 647 and FITC, followed by Sephadex G-25 size-exclusion chromatography. Anti-mouse MHC class II (clone IBL-5/22) mAb (28) was conjugated with FITC. The rat mAbs against mouse markers used for flow cytometry included PE-conjugated anti-CCR7 (clone 4B12), anti-CXCR4 (clone 2B11), and anti-CXCR5 (clone 2G8) from BD Biosciences (Diagon, Budapest, Hungary) and PE-labeled anti-CXCR7 (clone 73411) from R&D Systems (Bio-Techne R&D Systems, Budapest, Hungary). PE-conjugated anti-–BAFF-R (clone 7H22-E16), PE-labeled anti-TACI (clone 8F10), Alexa Fluor 647–conjugated rat anti-mouse anti-Blimp-1 (clone 5E7), and anti-mouse T-bet (clone 4B10) mAbs, PE-conjugated hamster anti-mouse gp38/podoplanin mAb (clone 8.1.1), and rat mAb against mouse Ki-67 Ag (clone 11F6) were obtained from BioLegend (Biomedica Hungaria, Budapest, Hungary). The anti-BCMA mAb (clone 161616, conjugated with FITC) was purchased from R&D Systems, and the biotinylated hamster anti-mouse CD11c mAb

(clone N418) from eBioscience (Thermo Fisher Scientific, Budapest, Hungary) was detected with streptavidin-PE conjugate (BD Biosciences). Goat anti-rat IgG-PE conjugate (BD Biosciences) and ImmPRESS goat anti-rat IgG-HRP conjugate (Vector Laboratories, Biomarker, Gödöllő, Hungary) were used as secondary Abs.

Flow cytometry and lymphoma sorting

mLNs harboring Bc.DLFL1 lymphoma following i.p. injection were collected from mice following euthanization by cervical dislocation. Enlarged mLNs were removed and gently crushed between the frosted ends of two microscope slides, followed by filtration through 70-μm pore size cell strainers (Greiner Bio-One Hungary, Mosonmagyaróvár, Hungary) using PBS containing 0.1% BSA and sodium azide. Cells (2×10^5) were incubated with fluorochrome-labeled Abs on ice for 30 min, then fixed in 1% PBS-buffered formaldehyde. For intracellular staining, samples were first labeled for cell surface markers, followed by fixation in 1% paraformaldehyde in PBS, followed by washing in PBS containing 0.1% saponin and 1% BSA, and then by incubation with mAbs against T-bet and Blimp-1 at room temperature. The samples were analyzed using BD FACSCalibur and the CellQuest Pro software, collecting at least 10,000 events gated on forward scatter (FSC)/side scatter (SSC) characteristics and B220 expression.

For IgV$_H$ sequencing, Bc.DLFL1 lymphoma cells were purified by a Bio-Rad S3e sorter and ProSort software v1.6 using FSC/SSC area/width gating combined with B220 labeling of lymphoblasts, followed by mRNA isolation from 10^5 lymphoma cells.

Bc.DLFL1 IgV$_H$ sequence analysis

Total mRNA from sorted Bc.DLFL1 cells was isolated using a NucleoSpin RNA XS kit (Macherey-Nagel, Izinta Biotech, Budapest, Hungary). Purity and concentration of mRNA were measured by NanoDrop. cDNA synthesis was performed using a high-capacity cDNA reverse transcription kit (Thermo Fisher Scientific). Endpoint PCR was carried out on Applied Biosystems 2720 thermal cycler using DreamTaq Green PCR master mix (Thermo Scientific) with described primers (29).

The PCR products were sequenced by a BigDye terminator cycle sequencing ready reaction kit v1.1 on an AB 3500 genetic analyzer (Applied Biosystems, Foster City, CA) and the results were analyzed by the IMGT/HighV-QUEST platform (30).

Immunohistology and immunofluorescence

From the mLNs and mesenteries of BALB/c mice with advanced stage of Bc.DLFL1 spreading frozen sections at 8 μm thickness were prepared with a Leica CM1850 cryostat. After drying, the sections were fixed in cold acetone. For immunohistochemistry with anti-B220 and anti–Ki-67 rat mAbs, the sections were incubated in 1 mg/ml phenyl-hydrazine in PBS for 20 min, followed by washing in PBS. Next, the sections were saturated with 5% BSA for 20 min, followed by the addition of primary Abs, and were incubated for 45 min at room temperature in a humidified chamber. After washing, the sections were incubated with HRP-conjugated anti-rat IgG and developed using diaminobenzidine/H$_2$O$_2$ in 20 mM Tris, 500 mM NaCl (pH 7.5). After rinsing in distilled water, the sections were counterstained with Mayer's hematoxylin and mounted in Pertex. Dual immunofluorescence for B220 and CD11c was performed by incubating acetone-fixed and BSA-blocked cryostat sections using a mixture of FITC anti-B220 and biotinylated anti-CD11c, followed by extensive washing and visualization of biotinylated mAb with a PE-streptavidin conjugate.

For combined immunofluorescence of GFP and gp38/podoplanin, the mesentery from lymphoma-injected BALB/c^{eGFP} recipients was fixed in 4% PBS-buffered paraformaldehyde for 2 h, followed by 30% sucrose equilibration overnight. Following embedding in Killik cryoprotective compound, the samples were frozen and 20-μm-thick cryostat sections were cut and placed on silane-coated microscope slides. Following drying, the sections were rehydrated and blocked in 5% BSA for 20 min, followed by incubation with PE-conjugated anti-gp38 mAb in PBS. After washing, the sections were mounted with 50% PBS-glycerol containing Hoechst 33342 nuclear counterstain. Confocal fluorescence images were taken using an Olympus FluoView FV1000 laser scanning confocal imaging system (Olympus Europa, Hamburg, Germany).

BAFF-R blockade in lymphoma-bearing mice

BALB/c mice ($n = 10$) received 5×10^6 Bc.DLFL1 cells in RPMI 1640 medium i.p. in 1-ml vol, followed by i.v. treatment of 100 μg of mBR3-Fc fusion protein (generously supplied by Genentech) in PBS three times a week, for a total of four injections. Control mice ($n = 10$) received a similar dose of mouse IgG1 isotype anti-fluorescein mAb F4/1 in PBS (31). The experiment was terminated on the 18th day after the lymphoma inoculation, followed by autopsy and macroscopic inspection of the mice. The effect of

BAFF-R blockade on the composition of peripheral lymph nodes was assessed by the flow cytometric analysis of axillary lymph nodes for the T cell/B cell ratio using FITC-conjugated anti-CD3 and Alexa Fluor 647–labeled anti-B220 mAbs.

In vitro culture of Bc.DLFL1 cells and lentiviral transduction with ZsGreen1 fluoroprotein

Bc.DLFL1 cells were seeded onto six-well plates (Greiner Bio-One Hungary, Mosonmagyaróvár, Hungary) containing adherent peritoneal exudate cells obtained by the peritoneal lavage of BALB/c mice with RPMI 1640 and 10% FBS containing 2 mM GlutaMAX (Thermo Fisher Scientific, Budapest, Hungary) and 5×10^{-5} M 2-ME.

Vesicular stomatitis virus glycoprotein G–pseudotyped lentiviral vectors encoding ZsGreen1 GFP driven by an EF1α promoter (Vectalys, Genomix Explorea, Budapest, Hungary) at a multiplicity of infection of 20 were incubated with the lymphoma cells overnight. After incubation, the lymphoma cells were washed and cultured in RPMI 1640 supplemented as above. Following the visual detection of green fluorescence using a ZOE fluorescent cell imager (Bio-Rad) in the lymphoma colonies, the lymphoma cells were collected and, following staining with anti-B220 Alexa Fluor 647 mAb conjugate, the lymphoma cells with the highest 10% expression of green fluorescence (Bc.DLFL1^{ZsGreen1}) were sorted using a Bio-Rad S3e sorter and subsequently propagated in vitro.

Homing of blood-borne Bc.DLFL1^{ZsGreen1} lymphoma cells

Bc.DLFL1^{ZsGreen1} cells were injected i.v. at 2×10^6 cells/recipient dose in a 100-μl vol via the tail vein in RPMI 1640. Twelve hours after injection, the recipient mice were sacrificed, and their spleens were processed for immunofluorescence detection using Alexa Fluor 647–labeled anti-B220 and anti-MARCO (no. IBL-12 [32]) Abs on cryostat sections at 8-μm thickness from 4% paraformaldehyde-fixed tissues after overnight equilibration in 20% sucrose. After mounting, the sections were viewed under an Olympus Fluo-View FV-1000 laser scanning confocal microscope; the images were edited using Adobe Photoshop 6.0 with corrections for brightness contrast and color balance applied for the entire images.

R&D Systems cytokine array of lymphoma tissue extract and quantification

Omentum, jejunal mesentery, and mLNs were collected either from the end-stage lymphoma–bearing mice or from untreated BALB/c mice. Of each sample, 20–30 mg of tissues was fast-frozen in liquid nitrogen, followed by lysing using T-PER tissue protein extraction reagent (Thermo Scientific) mixed with protease inhibitor mixture (Sigma-Aldrich, Budapest, Hungary) according to the manufacturers' protocols, and dissociated mechanically by Potter homogenizer at room temperature. The lysate was applied onto the membranes in Proteome Profiler array mouse XL cytokine array kit (R&D Systems) and processed according to the manufacturer's protocol. The membranes were imaged by using a LAS 4000 image reader and software using chemiluminescence measurements at 180-s exposure time and analysis using ImageJ (National Institutes of Health). Relative density parameters (X_{lymph} or X_{ctr}) were corrected by subtracting the negative reference values (N_{lymph} or N_{ctr}), and the ratio to the positive reference values (Ref_{lymph} or Ref_{ctr}) was calculated according to the following calculation: $X = [(X_{lymph} - N_{lymph})/(Ref_{lymph} - N_{lymph})]:[(X_{ctr} - N_{ctr})/(Ref_{ctr} - N_{ctr})]$.

Heatmap was created with the pheatmap (33) package within R (34). Raw data were normalized to Z scores. The complete clustering method with Euclidean distance was applied to the normalized dataset, which was visualized with the pheatmap function from the pheatmap package.

Statistical analysis

Statistical analysis of BAFF-R treatment effect on T cell/B cell distribution was performed by a Student t test using GraphPad Prism 5, where significance was considered with a p value <0.001. Analysis of CD80, CD86, T-bet, and Blimp-1 expression was performed using ANOVA. Error bar represents SEM. A Kaplan–Meier survival curve was generated by using GraphPad Prism 5 ($p < 0.01$).

Results

Bc.DLFL1 lymphoma cells display phenotypic features and tissue positioning similar to extrafollicular T-bet$^+$ B cells

Our earlier findings have revealed that Bc.DLFL1 lymphoma cells as a spontaneous DLBCL in BALB/c mice have remarkably restricted tissue propagation following i.p. injection, and they display several

mature B cell markers, including CD19, B220, MHC class II Ag, and MAC-1 (CD11b/CD18) without the expression of CD5, and they lack CD21 and CD23 markers (26, 35). The absence of CD5 excludes their B1-a B cell origin, and expression of the CCR7 chemokine receptor coupled with the absence of CXCR5 suggested an extrafollicular origin of Bc.DLFL1 cells (35). Therefore, we tested for the presence of the CXCR4 chemokine receptor for CXCL12 (36) together with the display of the atypical chemokine receptor CXCR7/ACKR3 competing for the same CXCL12 ligand (37). We found CXCR4 expression by >95% of the lymphoma cells, but no detectable CXCR7/ACKR3 display (Fig. 1A).

CXCR4 expression has been reported for a minor CD11c$^+$ extrafollicular splenic B cell subset linked to memory B cells, denoted as ABCs (16). We therefore next tested whether Bc.DLFL1 lymphoma cells display CD11c Ag by flow cytometry, and we found that the CD19$^+$ lymphoma cells overwhelmingly coexpress CD11c (Fig. 1B). Furthermore, systemic analysis of various cell populations in the lymphoma sample within the CD19$^-$/B220$^-$ non–B cell subset also revealed the presence of cells with a CD11c$^+$/MHC class II^{hi} additional phenotype, which we identify as dendritic cells
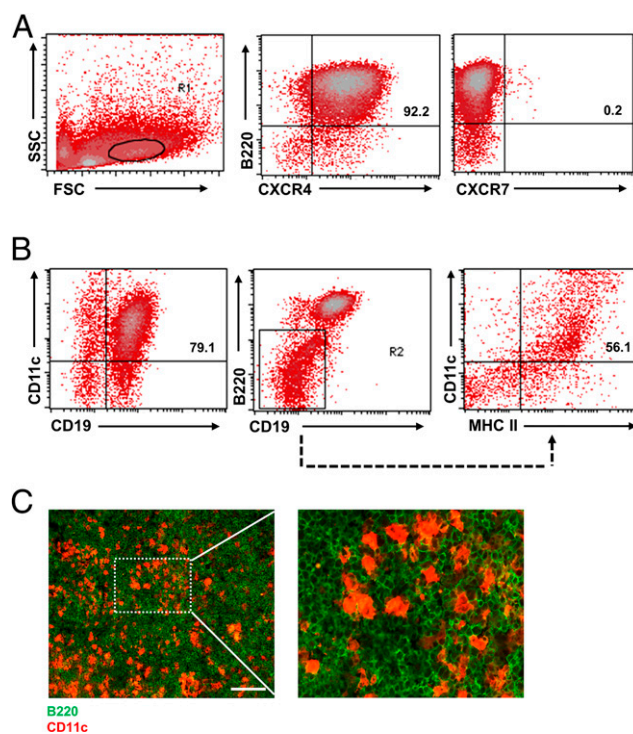

FIGURE 1. Bc.DLFL1 cells express CXCR4 chemokine receptor and CD11c and intermingle with CD11c$^+$ DCs. (**A**) Flow cytometric analysis illustrates lymphoma cells from mLNs gated on R1 according to size (FSC) and granularity (SSC, left), stained for B220 and CXCR4 (middle) or its decoy analog, CXCR7 (right). Numbers in the upper right quadrants correspond to the frequency of R1-gated double-positive cells, indicating the production of CXCR4 and the absence of CXCR7 on the lymphoma cells. Representative images are from a cohort of $n = 3$ mice. (**B**) Lymphoma samples from mLNs were labeled with CD19 and CD11c by flow cytometry, revealing CD11c expression by the lymphoma cells (left; the number indicates the frequency of FSC/SSC-gated [R1] lymphoma cells). Further gating on B220/CD19 double-negative non–B cells (R2, middle) stained for MHC class II and CD11c demonstrates the presence of MHC class II^{hi} CD11c$^+$ DCs (right). Representative images are from a cohort of $n = 3$ mice. (**C**) Staining of mLN sections from lymphoma-bearing mice (10 d after injection of Bc.DLFL1 cells) for B220 and CD11c demonstrates diffuse distribution of DCs in the lymphoma tissue (representative images are from a cohort of $n = 4$). Scale bar, 100 μm. Central region outlined with a dotted rectangle at a higher magnification is shown on the right.

(DCs) (38) (Fig. 1B). To determine the tissue distribution pattern of CD11c^{+} DCs, we stained spleen sections at advanced stage (day 10 postinjection) of lymphoma for B220 and CD11c, and found that the CD11^{+} DCs were detectable throughout the lymphoma infiltrate intermingled with B220^{dim} Bc.DLFL1 cells (Fig. 1C).

A characteristic feature of a normal CD11c^{+} ABC subset is expression of the T-bet transcription factor (14, 16, 17); therefore, we next investigated whether the CD11c^{+} Bc.DLFL1 cells produce this protein. Using flow cytometry, we found a readily detectable T-bet expression in lymphoma cells, whereas the residual normal B cells were negative. In addition, Blimp-1 transcription factor promoting plasmacellular differentiation of activated B cells (39) was also detectable (Fig. 2A); however, Bc.DLFL1 cells do not express CD138, a marker typical of mature plasma cells (data not shown). In addition to CD11c expression, Bc.DLFL1 cells also have an increased level of expression of both CD80 ($p < 0.0001$) and CD86 ($p < 0.05$) activation markers (18) compared with residual lymphocytes, also confirmed by statistical analysis of mean fluorescence intensities (MFIs), similarly to the activated/memory subset of the normal murine ABC pool (12) (Fig. 2B).

Assuming that the CXCR5^{−}/CCR7^{+}/CXCR4^{+} chemokine receptor composition guides the BcDLFL.1 cells outside the follicles, we next tested the distribution pattern of lymphoma cells in spleen following i.v. injection, as the positioning pattern of the ABC subset was described in detail in this organ (18). To trace the lymphoma cells, we lentivirally transduced the lymphoma cells with ZsGreen1 fluoroprotein followed by sorting and in vitro propagation, resulting in a homogeneous and intense fluorescence of lymphoma cells (Supplemental Fig. 1). We found that 12 h after the i.v. injection most Bc.DLFL1[ZsGreen1] cells congregated at extrafollicular compartments of the splenic white pulp, although a smaller fraction was also detectable either in the marginal zone or in the red pulp delineated by anti-MARCO immunolabeling (Fig. 3).

Taken together, these findings suggest that Bc.DLFL1 cells represent the DLBCL counterpart of non-follicular CD11c^{+}/CXCR4^{+}/CD138^{−} isotype-switched T-bet^{+} plasmablasts from ABC B cell subset origin. These lymphoma cells localize to extrafollicular locations within lymphoid organs, and they expand in a microenvironment containing numerous CD11c^{+}/MHC class II^{hi} DCs.

IgV_H region sequence of Bc.DLFL1 lymphoma reveals somatic hypermutation

As T-bet^{+} ABCs typically display memory B cell features (12, 16), we also investigated whether the V_H region of Bc.DLFL1 lymphoma cells contains point mutations that could confirm their potential memory B cell derivation. We sequenced the V region amplified from cDNA, and the sequence alignment (30) with the germline mouse IgV_H region (comprised of IgHV2-6-4*01/IgHD2-2*01/IgHJ*01 segments; GenBank accession no. MW191849; https://www.ncbi.nlm.nih.gov/nuccore/MW191849) revealed 11 non-silent mutations (two mutations in framework region 1 [FR1], one mutation in CDR1, and four mutations in CDR2 and CDR4 in FR3, respectively) and one silent mutation (in FR1), indicating a different V_H region usage than reported among the most frequent recombinant variations for the ABC subset associated with systemic lupus erythematosus (40). Furthermore, we also found that cytoplasmic IgG2a Igs are also detectable in the Bc.DLFL1 cells in agreement with the contribution of ABC cells in IgG-mediated recall responses (16) (Supplemental Fig. 2). These findings complement the phenotypic characteristics suggesting the memory-like ABC origin of Bc.DLFL1 lymphoma, also displaying plasmablastic features, including Blimp-1 expression and cytoplasmic IgG2a, despite the absence of CD138.
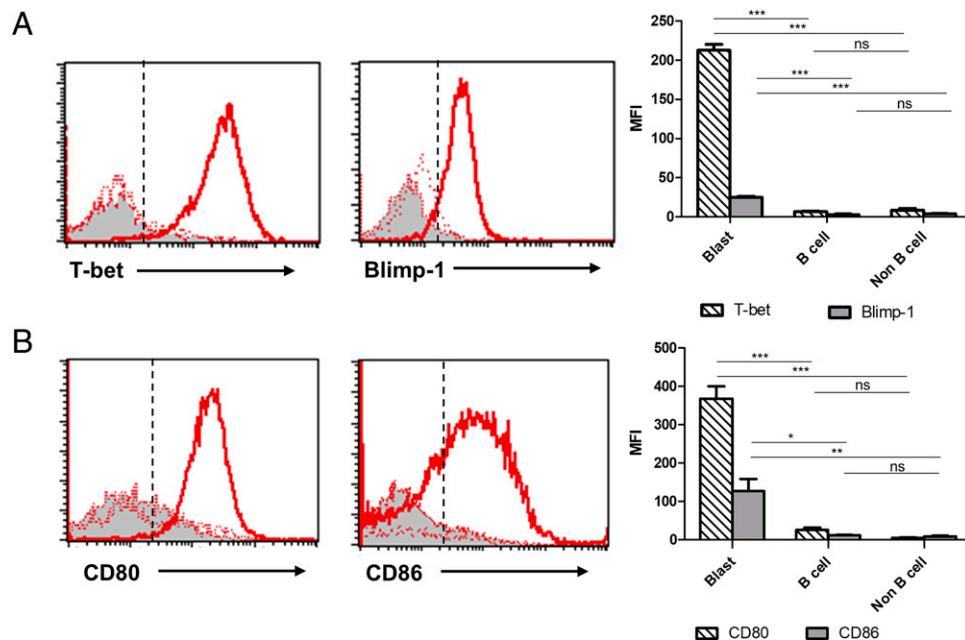

FIGURE 2. Expression of T-bet, Blimp-1, and activation-related surface markers by Bc.DLFL1 cells. (**A**) Bc.DLFL1 lymphoma (indicated by thick red line) produces T-bet (left) and Blimp-1 (right) transcription factors suggesting ABC-derived plasmablastic origin. Lymphoma cells (thick red line in the histogram overlays) were compared with residual normal B cells (dashed red line) and non−B cells (gray filling with red line). Vertical dashed lines in the histogram overlays correspond to the isotype-matched control with <1% of positive cell frequency. Representative data are from a cohort of $n = 3$ mice. Bar graphs demonstrate statistical analysis of mean fluorescence intensities (MFIs) for expression of T-bet (striped) and Blimp-1 (gray-filled) with SEM between Bc.DLFL1 lymphoma (Blast), residual B cells, and B220^{−} cells (non-B cell). ***$p < 0.001$. ns, not significant. (**B**) Staining for CD80 and CD86 reveals increased expression on lymphoma cells (thick red line in the histogram overlays) compared with residual normal B cells (dashed red line) and non−B cells (gray filling with red line; representative images are from a cohort of $n = 3$ mice). Vertical dashed lines correspond to the isotype-matched control with <1% of positive cell frequency. Bar graphs demonstrate statistical analysis of MFIs for expression of CD80 (striped) and CD86 (gray-filled) with SEM between Bc.DLFL1 lymphoma (Blast), residual B cells, and B220^{−} cells (non-B cells). *$p < 0.05$, **$p < 0.01$, ***$p < 0.001$. ns, not significant.
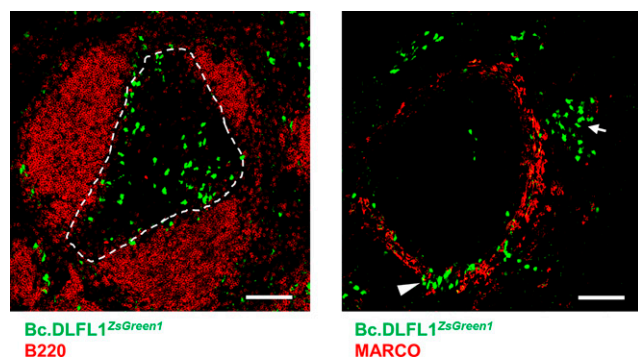
FIGURE 3. Bc.DLFL1 cells localize to extrafollicular locations after i.v. injection. Following i.v. injection of ZsGreen1-expressing Bc.DLFL1 cells (green), 12 h later the lymphoma cells within spleen are located in the T cell zone (outlined with dashed line) within the white pulp, excluded from the follicles (delineated by anti-B220 staining, red, left), and also accumulate in the red pulp (arrow) and in the marginal zone (arrowhead, identified by anti-MARCO [red] labeling, right). Representative confocal microscopic images are from a cohort of $n = 4$. Scale bars, 100 μm.

BAFF blockade elicits partial tumor growth blockade in Bc.DLFL1 lymphoma recipients

Similarly to TNF/lymphotoxins, CD40L, and several other cytokines provided by follicular stromal cells, macrophages, and follicular T helper cells, BAFF also promotes the survival of both normal centroblasts in the GC reaction and malignant B cells (41, 42). To investigate whether BAFF-R contributes to disease progression for Bc.DLFL1 lymphoma as an extrafollicular T-bet[+] DLBCL model of ABC origin, we first tested the expression of BAFF-R and its analogs BCMA and TACI on lymphoma cells by flow cytometry. Our results reveal that Bc.DLFL1 cells display both BAFF-R and TACI at a higher expression compared with normal B cells. According to our findings, BAFF-R is expressed at a higher level than TACI on Bc.DLFL1 cells; however, compared with normal follicular B cells, TACI showed a higher increase in the lymphoma cells, as defined by MFI. Thus, the MFI for normal B cell/lymphoma BAFF-R showed an ~2-fold increase, whereas for TACI we detected a 3-fold MFI increase, although from a lower normal level of expression. In contrast, BCMA was not detectable at a level exceeding normal B cell expression above background staining (Fig. 4A).

To study whether the use of soluble mBR3-Fc as a BAFF-R decoy receptor (43) would influence the disease progression, we next i.v. injected recipients with the soluble BAFF-R–Ig decoy receptor or control mouse IgG1 on days 1, 4, 6, and 8 after i.p. lymphoma administration and compared their survival to the control mouse IgG-treated group. We found that in the control group the mice started dying on day 13 (5 d after the last injection), followed by a rapid drop of survival during the next 4 d. In contrast, by the 18th day after lymphoma injection, in the mBR3-Fc–treated group only one mouse succumbed to lymphoma, whereas in the control group only three mice survived (Fig. 4B). The efficiency of BAFF-R antagonization to deplete normal B cells was confirmed by the flow cytometric evaluation of T cell/B cell distribution in unaffected axillary lymph nodes in moribund mice receiving either mBR3-Fc or control treatment at end-stage lymphoma. We found a significant reduction of B cell frequency in mBR3-Fc–treated samples, indicating the overall efficiency of BAFF blockade ($n = 3$ [mean ± SEM], $p < 0.001$) (Fig. 4C). In addition, the autopsy performed after the termination of the experiment in the surviving animals following mBR3-Fc treatment revealed various degrees of lymphoma propagation (Supplemental Table I). These findings demonstrate that mBR3-Fc treatment efficiently prolongs the survival in most treated animals, even though it cannot completely prevent the lymphoma progression,

in addition to reducing the frequency of normal B cells as well. Our attempt to define the BAFF or APRIL dependency using in vitro tissue culture of Bc.DLFL1 cells in the presence of a 1 μg/ml concentration alone or in combination did not appear to enhance their survival during a 4-d culture period (data not shown).

Extranodal microenvironment of Bc.DLFL1 lymphoma contains gp38^{+} reticular cells

In the autopsy of terminated animals after Bc.DLFL1 lymphoma injection, we found thickened and fragile mesenteric branches connecting the enlarged mLN and gut, indicating malignant infiltration of these serosal adipose compartments by the tumor (Fig. 5A). In untreated animals, the normal mesentery overwhelmingly consists of adipocytes (Fig. 5B). The displacement of adipose tissue with B cell lymphoma was verified using anti-B220 immunohistochemistry, revealing a massive tumor burden, where local proliferation of lymphoma cells within the mesentery occurred, as demonstrated by their intense staining for the Ki-67 proliferation marker (Fig. 5C, 5D).

As the lymphoma showed preferential accumulation and subsequent expansion at extrafollicular locations that contain gp38/podoplanin[+] FRCs in both lymph nodes and spleen (44), next we tested whether the lymphoma-infiltrated adipose tissue microenvironment harbors putative FRCs. To ensure that the gp38[+] elements are of host origin, we used cytoplasmic eGFP Tg BALB/c mice as recipients (26) and performed whole-mount immunofluorescence (35). In mice with an advanced stage of lymphoma (at least 10 d after the injection), we found an extensive meshwork of gp38[+]/eGFP[+] FRCs in the mesentery surrounding the Bc.DLFL1 cells labeled with anti-B220 mAb (Fig. 6A–C). Whereas the eGFP-producing connective tissue constituents with fibroblastic morphology appeared evenly distributed within the lymphoma foci, the intensity of gp38 labeling was more pronounced at the edge of the lymphoma-infiltrated region, showing variable expression of gp38 within the GFP[+] reticular compartment (Fig. 6C). Overlaying the two different markers demonstrated, however, that the compartment with weaker gp38 intensity was similarly restricted to the eGFP-expressing host FRCs, although some eGFP^{+} reticular cells lacking gp38 reactivity were also detectable (Fig. 6D, 6F). In contrast, the mesentery from uninjected BALB/c[eGFP] mice showed only perivascular accumulation of gp38^{+} fibroblastic cells surrounding the branches of mesenteric vessels, with only a few scattered gp38^{+} reticular cells among the eGFP[+]/gp38[−] adipocytes (Fig. 6E). This finding indicates that the extranodal expansion of lymphoma is coupled with the displacement of adipocytes in the mesenteric microenvironment containing an extensive meshwork of gp38/podoplanin[+] FRCs of host origin.

Altered cytokine microenvironment associated with nodal and extranodal lymphoma expansion

While the mLNs represent natural niches to support the expansion of Bc.DLFL1 lymphoma, the infiltration of lymphoma cells in adipose tissues may be linked to alteration of the accessible cytokine microenvironment coupled with the appearance of gp38[+] FRCs, in addition to their dependence on BAFF-R ligand binding. Our analysis of serum cytokine levels in lymphoma-bearing mice and normal BALB/c mice using an extended proteome profile dot blot assay did not reveal any difference (data not shown). Therefore, to compare the distribution pattern of local factors, we next tested the cytokine landscape by comparing lymphoma-infiltrated mLNs, omenta (whole organ), and mesentery (30–40 mg wet weight from jejunal random sampling) to normal tissue samples as reference from a cohort of mice ($n ≥ 3$ each) and compared different tissues in lymphoma-bearing mice to each other as well (Fig. 7A). The fold change was determined as described in *Materials and Methods*.

In mLNs from lymphoma-bearing mice, we found a significant increase of factors mainly associated with endothelial activation and
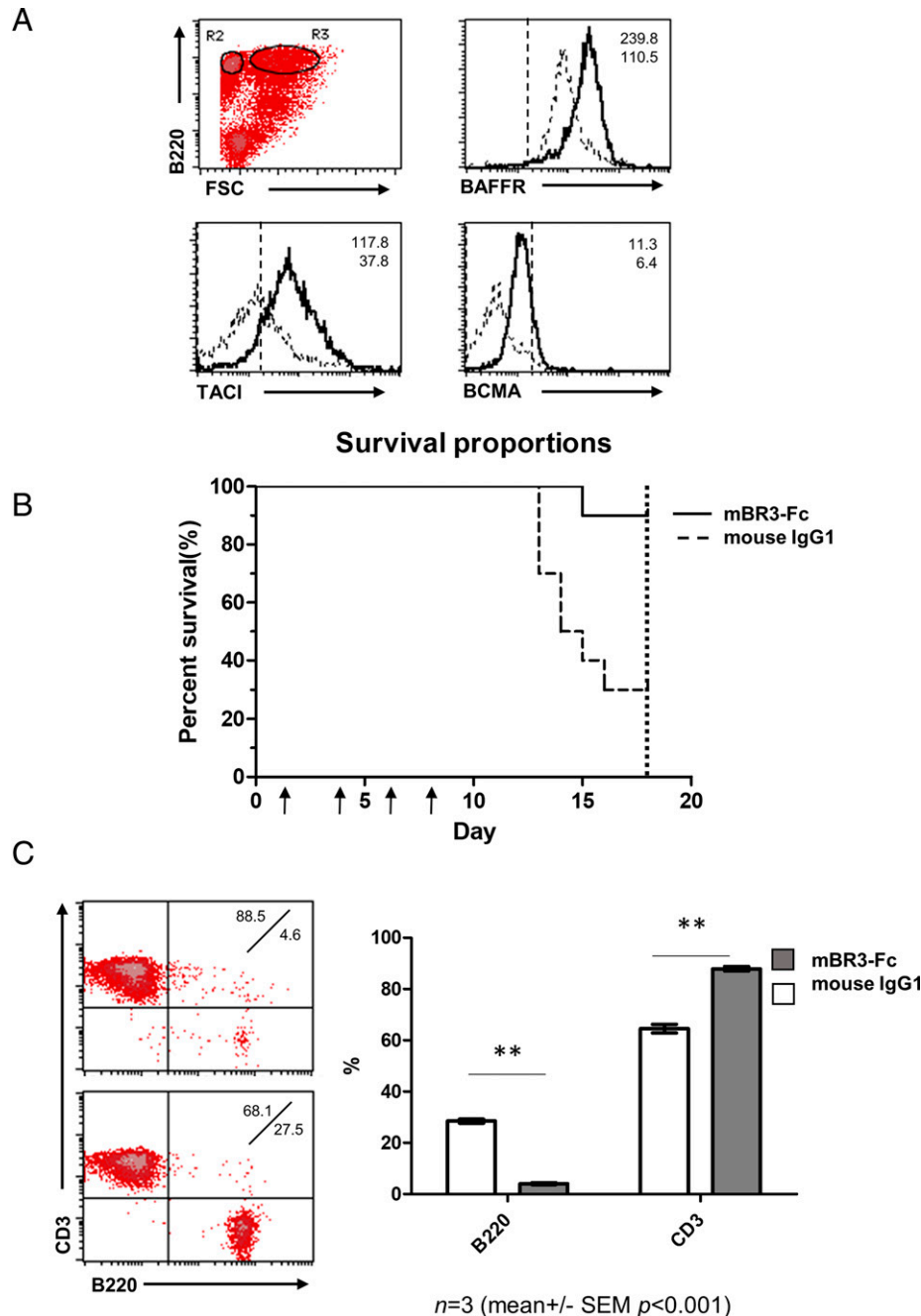
FIGURE 4. Expression of BAFF receptors by Bc.DLFL1 cells and the effect of BAFF-R antagonization by mBR3-Fc on the survival of lymphoma-injected mice. (**A**) mLN cells from lymphoma-injected mice that resolved into residual B cells (R2) and larger lymphoma cells (R3) were analyzed for the various analogs of BAFF-R by flow cytometry. Histogram overlays represent the expression of various receptors as indicated, with Bc.DLFL1 cells (thick lines) compared with residual B cells (dashed lines). Numbers indicate the mean fluorescence intensity (MFI) values for the markers by Bc.DLFL1 cells (upper values) or normal B cells (lower values). Vertical dashed lines correspond to the isotype-matched control with <1% of positive cell frequency. Representative images are from a cohort of $n = 3$ mice. (**B**) Kaplan–Meier curve of survival following BAFF-R antagonization showing the percentage of surviving animals (y-axis). Using a cohort of $n = 10$ mice, the mice received i.v. injections of 100 μg/mouse mBR3-Fc decoy receptor (continuous line) or mouse control IgG1 (dashed line) on four different days (D1, D4, D6, and D8, x-axis) after the i.p. injection of Bc.DLFL1 lymphoma on day 0, indicated by arrows. The vertical dotted line represents the termination of the experiment on day 18. The experiment was performed twice with similar results indicating significant differences in survival. (**C**) The in vivo mBR3-Fc treatment induces significant depletion of normal B cells in lymph nodes not affected by lymphoma expansion as revealed by flow cytometric analysis (representative image from a cohort of $n = 3$ mice). The upper density plot demonstrates T cell/B cell distribution in an mBR3-Fc–treated mouse, and the lower plot depicts a control IgG1-treated sample after anti-CD3/anti-B220 dual labeling. Upper/lower numbers correspond to the CD3^{+} T cells and B220^{+} B cell frequencies, respectively. The bar diagram illustrates the statistical analysis (mean ± SEM) of the alteration of T and B cell frequencies. **$p < 0.01$, by Student t test.

neoangiogenesis, such as E-selectin and various angiopoietins (Ang1 and Ang2), mesenchymal proliferation (platelet-derived growth factor [PDGF]) and matrix metalloproteases (MMP2, MMP3, and MMP9), and several chemokines (CXCL9, CXCL10, CXCL11, and CCL12).

In omenta, we found a significant increase of plasminogen activator inhibitor-1 (PAI-1/Serpin E1), possibly produced by adipocytes and endothelial cells, and lipocalin-2, in addition to a moderate increase for some chemokines (CXCL9, CXCL10, and CXCL11).
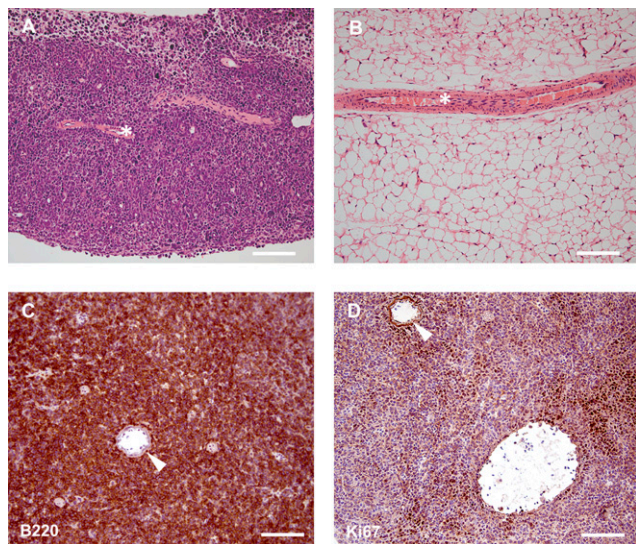
FIGURE 5. Extranodal growth of Bc.DLFL1 lymphoma cells in the mesentery. (**A**) H&E staining of mesentery section from dissected mesentery of an untreated lymphoma-bearing recipient shows large lymphoma infiltrate around the perivascular region (mesenteric artery is indicated with an asterisk; representative image from a cohort of $n = 4$ mice). Scale bar, 200 μm. (**B**) In normal mesentery (H&E staining) from an uninjected control, the perivascular adipose tissue is devoid of leukocytes (mesenteric artery is indicated with an asterisk; representative image from a cohort of $n = 4$). Scale bar, 100 μm. (**C**) Anti-B220 staining of cryostat section of mesentery from lymphoma-injected mouse demonstrates perivascular accumulation of B220$^+$ Bc.DLFL1 cells (brown precipitate, with hematoxylin [blue] counterstain). Arrowhead points to mesenteric artery cross-section. Scale bar, 100 μm. (**D**) Expression of Ki-67 proliferation-associated antigen (brown nuclear reactivity with blue hematoxylin counterstain) demonstrates extranodal division of Bc.DLFL1 lymphoma cells both at perivascular (arrowhead points to the mesenteric artery) and more distant regions within the mesentery. Representative image from a cohort of $n = 4$ mice. Scale bar, 100 μm.

In the mesenteric samples the strongest increase was found for IL-28, ICAM-1/CD54, and insulin-like growth factor binding protein-1 (IGFBP-1). In addition, other cytokines (largely similar to those in omenta) also showed some moderate increase (Fig. 7B).

The comparison of the pattern of differences of relative cytokine levels in various lymphoma-infiltrated tissues revealed that the largest degree of similarity was between the omenta and the mesentery, followed by the overlap between mLNs and omenta, and the least degree of similarity was apparent between mLNs and mesentery (Fig. 7C). In contrast, we could identify several cytokines that all increased in all three tissues upon lymphoma propagation (Table I). Taken together, these finding indicate that the relative abundance of soluble or extractable factors during the lymphoma propagation shows tissue-specific characteristics, with mLNs showing the most extensive alterations, primarily for mediators influencing vasculature, mesenchymal scaffolding; in contrast, the adipose alterations were more subtle, but generally they share similar features.

Discussion

In this study we provide evidence for the ABC derivation of a murine spontaneous DLBCL-type lymphoma Bc.DLFL1, including CD11c expression and T-bet production, the IgV$_H$ sequence revealing somatic hypermutations, and short-term homing characteristics. Collectively these features establish this lymphoma as a malignant representative of the activated ABC memory B cell subset, with
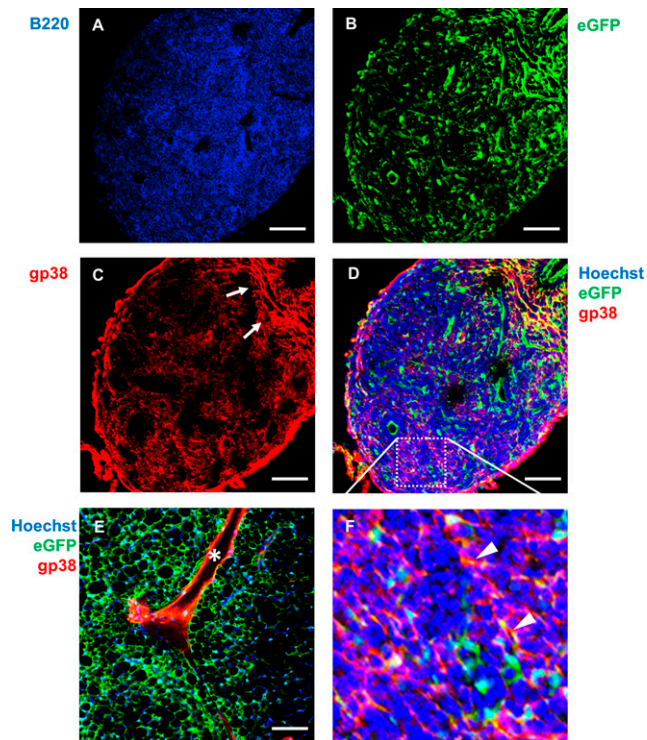

FIGURE 6. Expansion of gp38$^+$ fibroblastic cells associated with the extranodal metastasis of Bc.DLFL1 lymphoma in the mesentery. (**A**) Lymphoma cells (stained with anti-B220, blue) form large clusters in the mesentery at an advanced stage of lymphoma following i.p. injection in untreated lymphoma-bearing recipient. (**B**) In eGFP Tg BALB/c host mice the residual nonhematopoietic cells with fibroblastic appearance (green) extend throughout the lymphoma infiltrate in the mesentery at a similar intensity of eGFP expression. (**C**) Staining of sections with PE-conjugated anti-gp38 (red) reveals extensive fibroblastic reticular cell (FRC) labeling with various intensities, with a more pronounced labeling at the periphery of the infiltrate (arrows). (**D**) Merged image of the Hoechst-stained lymphoma cells, eGFP-expressing host nonhematopoietic cells, and gp38-stained FRCs. The rectangular field outlined with dotted line is shown in (**F**), demonstrating partial overlap between eGFP/gp38 as yellow color (arrowheads). (**E**) Whole-mount labeling for gp38 of normal mesentery from BALB/c^{eGFP} mice demonstrates only perivascular (asterisk indicates vessel lumen) clustering of gp38$^+$ FRCs surrounded by adipocytes. Note the distinctive confluent lattice-like appearance of adipocyte-associated green fluorescence compared with FRC-related meshwork pattern of eGFP signal (B), with Hoechst33342 nuclear counterstaining (blue). Scale bars, 100 μm. Representative images are from a cohort of $n = 4$ mice.

partial plasmablastic differentiation, as suggested by the expression of Blimp-1. In addition, Bc.DLFL1 cells can expand at extranodal locations, and this process results in an altered cytokine microenvironment. Although substantial knowledge has accumulated following its recent identification concerning the physiological as well as pathological roles in autoimmune conditions, the lymphoproliferative aspects of the ABC subset have remained uninvestigated.

Spontaneous or induced (also including transgenic-derived) mouse lymphomas have been important research tools for human B cell malignancies, including B cell chronic lymphocytic leukemia, DLBCL, and other lymphomas and multiple myeloma (45–47). BALB/c mice are particularly sensitive to mineral oil–induced plasmacytoma formation following i.p. injection of pristane oil, eliciting an inflammatory response and deregulation of ecotropic murine leukemia viruses (48, 49). The transformation occurs in the peritoneal cavity, and it can be facilitated by the deregulated expression of IL-6 in combination with IgH enhancer Eμ-translocated c-*myc*, resulting in plasma cell malignancies at 100%
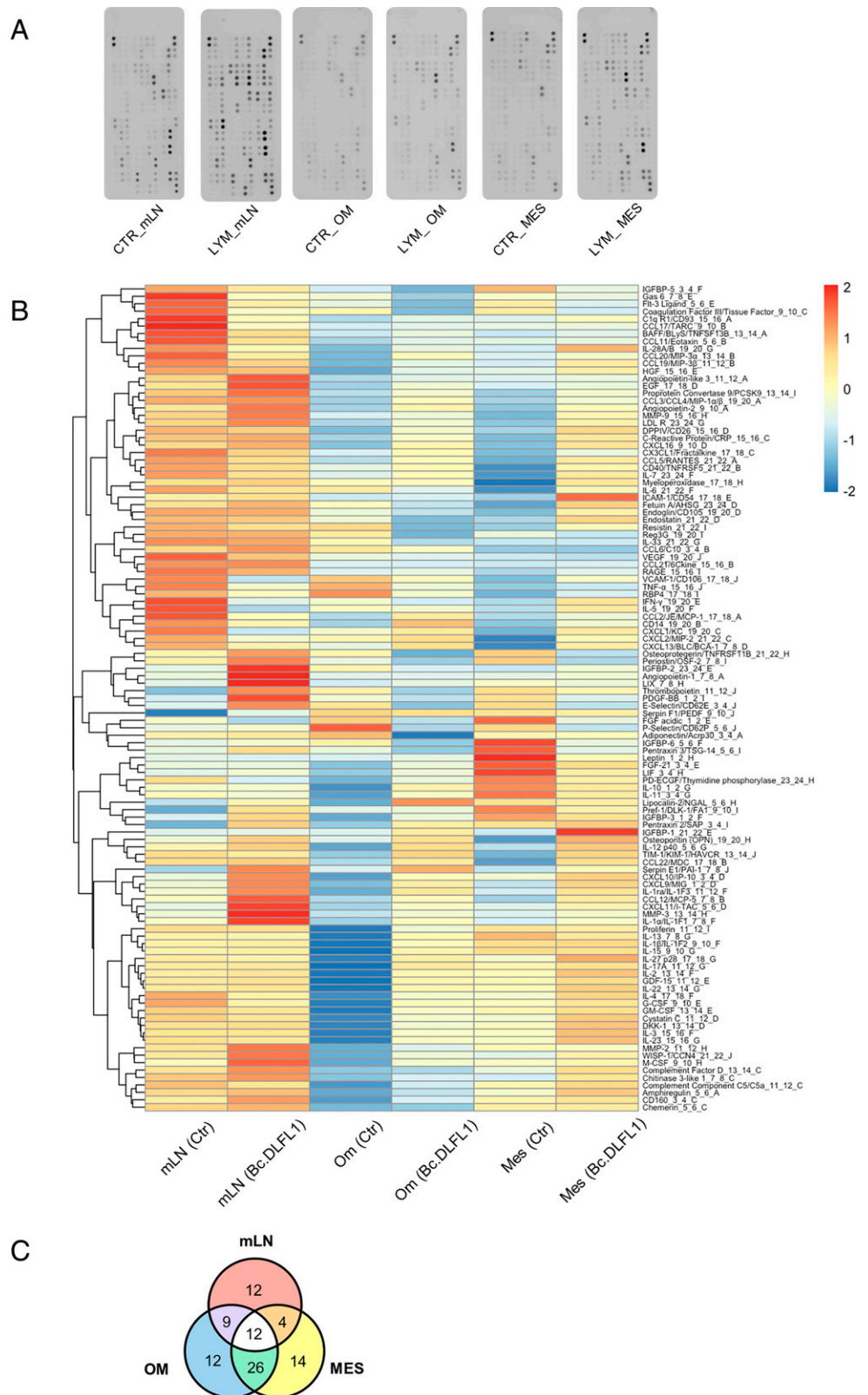
FIGURE 7. Alterations of cytokine profile associated with nodal and extranodal lymphoma expansion. (**A**) Multiplex cytokine array reveals distinct patterns of alteration between lymphoma-infiltrated (LYM) mLN, omentum (OM), and mesentery (MES) in a pairwise comparison with normal (CTR) tissue samples. (**B**) Quantitative densitometric analysis summarizes the relative expression levels of various cytokine clusters. (**C**) Venn diagram summarizes the degree of overlap of (at least 2-fold) of extractable cytokines and soluble factors between nodal and extranodal sites. Numbers correspond to the number of factors either shared or restricted to one indicated source of sample.

efficiency (50). These cells displayed either plasmablastic (high mitotic index) or plasmacytic (lower mitotic index) features, and they expressed the CD138 marker by both subtypes (50). In this model, the lymphoid tissues most heavily infiltrated include the mLNs and spleen, with frequent propagation in the gut mucosa, as well as the cervical and axillary lymph nodes, also involving parenchymal organs reached via the blood

vessels (50). In contrast, although Bc.DLFL1 cells primarily accumulated in the mLNs and spleen following i.p. injection (26), we found no indication for mucosal spreading or parenchymal (kidney, liver, lung) metastasis, thus excluding systemic hematogenic dissemination. In contrast, the mesentery and omental tissues were heavily infiltrated, most likely via migrating from preformed serosal foci including omental and

Table I. Summary of the cytokine alterations in mLNs and adipose tissues

Comparison	No.	Cytokines/Soluble Factors with 2-Fold Increase of Heatmap Intensity in Lymphoma Samples Compared with Normal Tissue Control
mLN versus Mes	4	IGFBP-2, MMP-9, myeloperoxidase, complement factor D
Mes versus Om	26	Amphiregulin, IL-2, IL-3, IL-4, IL-7, IL-12 p40, IL-22, IL-23, IL-27 p28, IL-28A/B, CCL2, CCL5, CCL19, CCL22, CX3CL1, CD14, complement C5/C5a, cystatin C, DKK-1, Dpp4, GDF-15, G-CSF, HGF, IGFBP-1, OPN, TIM-1
mLN versus Om	9	EGF, lipocalin-2, IGFBP-3, pentraxin 2, Serpin E1, MMP-3, Gas-6, M-CSF, CD160
All three	12	Angiopoietin-2, IL-1ra, CCL3/CCL4, CCL12, CXCL16, CXCL9, CXCL10, CXCL11, CRP, LDL R, PCSK9, WISP-1

Shown is a three-way comparison between mesenteric lymph nodes and mesentery (mLN versus Mes), mesentery and omentum (Mes versus Om), and mesenteric lymph nodes and omentum (mLN versus Om) indicates the number (No.) and type of overlapping cytokines, and those cytokines that increased in all three tissues compared with the relevant tumor-free sample (All three).

mesenteric fat-associated lymphoid clusters and foliate lymphoid aggregates, a more organized variant of serosal lymphoid structures as lymphoma-binding territories, through the mesenteric lymphatic capillaries (35). Furthermore, the course of the Bc.DLFL1 lymphoma propagation leading to death within 16–20 d was substantially faster, compared with the Il6-cMycEμ compound model, with 4–6 wk latency, also requiring pristane pretreatment. Although we found that in short-term homing investigations Bc.DLFL1 cells could reach the spleen following i.v. injection, the onset of lymphoma spreading in this setting has not yet been investigated, and therefore their eventual access to the bone marrow or mucosal sites as major destinations for plasmablasts (51) cannot be excluded.

The most frequently used cell line representing follicular DLBCL from BALB/c mice is the A20 cell line, with distinct phenotypic and karyotypic traits compared with Bc.DLFL1 lymphoma (35, 52). The differences between the two DLBCL variants include the differential expression pattern of CXCR5 and CCR7 chemokine receptors, which correlated with their preferential positioning within serosal lymphoid territories (35). To determine the location within organized secondary lymphoid tissues, we found that Bc.DLFL1 cells with a CXCR5−/CCR7+/CXCR4+/CXCR7− phenotype had dual accumulation preferences in the T cell zone within the white pulp, and marginal zone/red pulp outside the white pulp, respectively. This pattern mirrors the reported distribution of the T-bet+ and CD11c+ normal ABC subset (18); therefore, it is probable that these B cells retain their extrafollicular positioning within the lymphoid tissues during plasmablastic differentiation. Alternatively, other factors fine-tuning GC organization and centroblast confinement within GCs may be altered in Bc.DLFL1 cells, including expression and ligand binding by the P2RY8 receptor (53, 54). At this extrafollicular location the lymphoma cells may directly interact with both mobile CCR7-directed other cells (including DCs) and specialized stromal cells, receiving survival stimuli and exerting immunomodulatory activities (55). Our finding on the presence of DCs in lymphoma infiltrates supports this scenario, where local DCs via producing the BAFF ligand (or analogs) or IL-6 may facilitate the survival and expansion of Bc.DLFL1 cells (56, 57), as BAFF antagonization could significantly prolong the survival of lymphoma-bearing mice. More prolonged BAFF inhibition or combination with other blocking agents (including anti–IL-6 or anti-CD40) may prove more effective to improve survival, thus offering a more detailed analysis for the soluble factor survival requirements of Bc.DLFL1 cells in the lymph node environment. Further studies may also reveal the subtype of DCs and their spatial relationship to the

lymphoma cells during the course of the lymphoma expansion. In addition, DCs may also influence the fibroblastic architecture, contractility, and remodeling in lymphoma-harboring lymphoid tissues (58), and thus their experimental modulation may identify other critical cellular mediators of lymphoma survival.

Production of the T-bet transcription factor is a typical feature of the CD11c+ ABC subset (14–17). As Bc.DLFL1 cells also express CD11c, yet represent DLBCL-type malignancy, the expression of T-bet may be a consequence of genomic alteration leading to dysregulated T-bet production, irrespective of the origin (ABC or other B cell subset) of the lymphoma. As a potential candidate responsible for disturbed T-bet expression, the c-Myb transcription factor (encoded by chromosome 10) may play an important suppressive function, as its selective inactivation in B cells leads to upregulation of T-bet coupled with disturbed plasmacellular differentiation and GC formation (59). Indeed, Bc.DLFL1 cells have several chromosomal translocations involving chromosome 10, including t(6:10); t(10:6); t(10:11), that may perturb c-Myb activity (35). However, the cell surface phenotype defined by CD19, CD21, CD23, CD80, CD86, CD11c, CD11b, and CD5 markers and several chemokine receptors (27, 35) and the in vivo lymphoid tissue distribution of lymphoma cells are all consistent with the ABC characteristics, rather than the translocation-induced upregulation of T-bet alone.

A striking feature of the extranodal propagation of Bc.DLFL1 lymphoma cells is their expansion in abdominal serosal tissues, particularly in the mesentery and omentum, as evidenced by Ki-67 expression, raising the lymphoma-supporting role of the local microenvironment. As these adipose tissues harbor only rudimentarily organized lymphoid aggregates, we hypothesized that tissue components related to non-follicular lymphoid stromal cells may be present, including FRCs expressing gp38/podoplanin involved in T zone organization (44). In normal mesentery, the podoplanin-expressing perivascular fibroblasts formed a compact sheath, but upon the presence of lymphoma cells, an extensive podoplanin-positive reticulum formed, largely replacing the adipose tissue, indicating the capacity of these mesenchymal cells for either expansion or tissue repositioning. Alternatively, adipose-derived mesenchymal stem cells supporting B cell lymphoma growth can be induced to become podoplanin-positive stromal cells (60), and therefore in this scenario the presence of podoplanin-positive FRCs is more likely to indicate the tumor-supporting function of these cells, rather than evidence for T zone–specific FRC differentiation within lymphoid tissues (61).

Finally, we also investigated the impact of extranodal lymphoma growth on the cytokine landscape in omentum and mesentery, compared with the nodal expansion within the mLNs. Our findings reveal a rather complex pattern of differences, with several characteristic alterations, where the adipose tissue samples displayed a substantially higher level of similarity between omentum and mesentery, and also some similar features shared with the mLN alterations. The differences of cytokine pattern between the various tissue samples infiltrated by the same lymphoma are likely related to the distinct microenvironmental characteristics, although the exact tissue sources for these factors and their roles in lymphoma propagation need to be defined in further studies. Particularly, potential production of important immunoregulatory cytokines (e.g., IL-10 or TGF-β) or chemokines found to be increased in affected tissues (CCL3/CCL4, CCL12, CXCL16, CXCL9, CXCL10, and CXCL11; Table I) as well as their receptor expression by lymphoma cells need to be determined, which may now be accomplished by the analysis of the in vitro adopted variant of Bc.DLFL1 cells. These investigations may also shed light on the exact relationship between tumor localization and expansion with these tissue factors, also revealing potential target molecules for diagnostic or therapeutic use (55). As splenic marginal zone lymphomas and extranodal B-cell lymphomas are typically T-bet+ (62, 63), the availability of this spontaneous ABC-derived lymphoma may thus offer a valuable in vivo

model for future investigations in the course as well as therapeutic possibilities for T-bet$^+$ B cell lymphoproliferative conditions in humans.

Disclosures

The authors have no financial conflicts of interest.

References

1. Shi, W., Y. Liao, S. N. Willis, N. Taubenheim, M. Inouye, D. M. Tarlinton, G. K. Smyth, P. D. Hodgkin, S. L. Nutt, and L. M. Corcoran. 2015. Transcriptional profiling of mouse B cell terminal differentiation defines a signature for antibody-secreting plasma cells. *Nat. Immunol.* 16: 663–673.
2. Cyster, J. G., and C. D. C. Allen. 2019. B cell responses: cell interaction dynamics and decisions. *Cell* 177: 524–540.
3. Silva-Cayetano, A., and M. A. Linterman. 2020. Stromal cell control of conventional and ectopic germinal centre reactions. *Curr. Opin. Immunol.* 64: 26–33.
4. Shlomchik, M. J., W. Luo, and F. Weisel. 2019. Linking signaling and selection in the germinal center. *Immunol. Rev.* 288: 49–63.
5. Chaplin, D. D., and Y. Fu. 1998. Cytokine regulation of secondary lymphoid organ development. *Curr. Opin. Immunol.* 10: 289–297.
6. Endres, R., M. B. Alimzhanov, T. Plitz, A. Fütterer, M. H. Kosco-Vilbois, S. A. Nedospasov, K. Rajewsky, and K. Pfeffer. 1999. Mature follicular dendritic cell networks depend on expression of lymphotoxin β receptor by radioresistant stromal cells and of lymphotoxin β and tumor necrosis factor by B cells. *J. Exp. Med.* 189: 159–168.
7. Fillatreau, S., C. H. Sweenie, M. J. McGeachy, D. Gray, and S. M. Anderton. 2002. B cells regulate autoimmunity by provision of IL-10. *Nat. Immunol.* 3: 944–950.
8. Mauri, C., and A. Bosma. 2012. Immune regulatory function of B cells. *Annu. Rev. Immunol.* 30: 221–241.
9. Rosser, E. C., and C. Mauri. 2015. Regulatory B cells: origin, phenotype, and function. *Immunity* 42: 607–612.
10. Rauch, P. J., A. Chudnovskiy, C. S. Robbins, G. F. Weber, M. Etzrodt, I. Hilgendorf, E. Tiglao, J. L. Figueiredo, Y. Iwamoto, I. Theurl, et al. 2012. Innate response activator B cells protect against microbial sepsis. *Science* 335: 597–601.
11. Chin, S. S., L. Chorro, J. Chan, and G. Lauvau. 2019. Splenic innate B1 B cell plasmablasts produce sustained granulocyte-macrophage colony-stimulating factor and interleukin-3 cytokines during murine malaria infections. *Infect. Immun.* 87: e00482-19.
12. Kugler-Umana, O., P. Devarajan, and S. L. Swain. 2020. Understanding the heterogeneous population of age-associated B cells and their contributions to autoimmunity and immune response to pathogens. *Crit. Rev. Immunol.* 40: 297–309.
13. Baba, Y., Y. Saito, and Y. Kotetsu. 2020. Heterogeneous subsets of B-lineage regulatory cells (Breg cells). *Int. Immunol.* 32: 155–162.
14. Hao, Y., P. O'Neill, M. S. Naradikian, J. L. Scholz, and M. P. Cancro. 2011. A B-cell subset uniquely responsive to innate stimuli accumulates in aged mice. *Blood* 118: 1294–1304.
15. Rubtsov, A. V., K. Rubtsova, A. Fischer, R. T. Meehan, J. Z. Gillis, J. W. Kappler, and P. Marrack. 2011. Toll-like receptor 7 (TLR7)-driven accumulation of a novel CD11c$^+$ B-cell population is important for the development of autoimmunity. *Blood* 118: 1305–1315.
16. Cancro, M. P. 2020. Age-associated B cells. *Annu. Rev. Immunol.* 38: 315–340.
17. Rubtsova, K., A. V. Rubtsov, J. M. Thurman, J. M. Mennona, J. W. Kappler, and P. Marrack. 2017. B cells expressing the transcription factor T-bet drive lupus-like autoimmunity. *J. Clin. Invest.* 127: 1392–1404.
18. Rubtsov, A. V., K. Rubtsova, J. W. Kappler, J. Jacobelli, R. S. Friedman, and P. Marrack. 2015. CD11c-expressing B cells are located at the T cell/B cell border in spleen and are potent APCs. *J. Immunol.* 195: 71–79.
19. Johnson, J. L., R. L. Rosenthal, J. J. Knox, A. Myles, M. S. Naradikian, J. Madej, M. Kostiv, A. M. Rosenfeld, W. Meng, S. R. Christensen, et al. 2020. The transcription factor T-bet resolves memory B cell subsets with distinct tissue distributions and antibody specificities in mice and humans. *Immunity* 52: 842–855.e6.
20. Du, S. W., T. Arkatkar, H. M. Jacobs, D. J. Rawlings, and S. W. Jackson. 2019. Generation of functional murine CD11c$^+$ age-associated B cells in the absence of B cell T-bet expression. *Eur. J. Immunol.* 49: 170–178.
21. Manni, M., S. Gupta, E. Ricker, Y. Chinenov, S. H. Park, M. Shi, T. Pannellini, R. Jessberger, L. B. Ivashkiv, and A. B. Pernis. 2018. Regulation of age-associated B cells by IRF5 in systemic autoimmunity. *Nat. Immunol.* 19: 407–419.
22. Zhang, W., H. Zhang, S. Liu, F. Xia, Z. Kang, Y. Zhang, Y. Liu, H. Xiao, L. Chen, C. Huang, et al. 2019. Excessive CD11c$^+$Tbet$^+$ B cells promote aberrant T$_{FH}$ differentiation and affinity-based germinal center selection in lupus. *Proc. Natl. Acad. Sci. USA* 116: 18550–18560.
23. Goldin, L. R., and O. Landgren. 2009. Autoimmunity and lymphomagenesis. *Int. J. Cancer* 124: 1497–1502.
24. Hemminki, K., X. Liu, J. Ji, and A. Försti. 2016. Origin of B-cell neoplasms in autoimmune disease. *PLoS One* 11: e0158360.
25. Mörth, C., A. Valachis, A. Abu Sabaa, K. Marshall, G. Hedström, M. Flogegård, E. Baecklund, and G. Enblad. 2019. Autoimmune disease in patients with diffuse large B-cell lymphoma: occurrence and impact on outcome. *Acta Oncol.* 58: 1170–1177.
26. Vojkovics, D., Z. Kellermayer, D. Heidt, M. Mihalj, B. Kajtár, D. Ernszt, T. Kovács, P. Németh, and P. Balogh. 2016. Isolation and characterization of a murine spontaneous high-grade follicular lymphoma with restricted in vivo spreading—a model for lymphatic metastasis via the mesentery. *Pathol. Oncol. Res.* 22: 421–430.
27. Kvell, K., T. Czömpöly, L. Hiripi, P. Balogh, J. Kóbor, L. Bodrogi, J. E. Pongrácz, W. A. Ritchie, and Z. Bősze. 2010. Characterisation of eGFP-transgenic BALB/c mouse strain established by lentiviral transgenesis. *Transgenic Res.* 19: 105–112.
28. Balogh, P., G. Horváth, and A. K. Szakal. 2004. Immunoarchitecture of distinct reticular fibroblastic domains in the white pulp of mouse spleen. *J. Histochem. Cytochem.* 52: 1287–1298.
29. Strebe, N., F. Breitling, D. Moosmayer, B. Brocks, and S. Dübel. 2010. Cloning of variable domains from mouse hybridoma by PCR. In *Antibody Engineering. Springer Protocols Handbooks.* R. Kontermann and S. Dübel, eds. Springer, Berlin, p. 3–14.
30. Alamyar, E., P. Duroux, M. P. Lefranc, and V. Giudicelli. 2012. IMGT$^®$ tools for the nucleotide analysis of immunoglobulin (IG) and T cell receptor (TR) V-(D)-J repertoires, polymorphisms, and IG mutations: IMGT/V-QUEST and IMGT/HighV-QUEST for NGS. *Methods Mol. Biol.* 882: 569–604.
31. Balogh, P., G. Szekeres, and P. Németh. 1994. Hapten-mediated identification of cell membrane antigens using an anti-FITC monoclonal antibody. *J. Immunol. Methods* 169: 35–40.
32. Kvell, K., T. Czömpöly, T. Pikkarainen, and P. Balogh. 2006. Species-specific restriction of cell surface expression of mouse MARCO glycoprotein in murine cell lines. *Biochem. Biophys. Res. Commun.* 341: 1193–1202.
33. Kolde, R. 2019. pheatmap: pretty heatmaps. Available at: https://cran.r-project.org/web/packages/pheatmap/index.html.
34. R Core Team. 2017. *R: A Language and Environment for Statistical Computing.* R Foundation for Statistical Computing, Vienna, Austria.
35. Jia, X., F. Gábris, Ó. Jacobsen, G. Bedics, B. Botz, Z. Helyes, Z. Kellermayer, D. Vojkovics, G. Berta, N. Nagy, et al. 2020. Foliate lymphoid aggregates as novel forms of serous lymphocyte entry sites of peritoneal B cells and high-grade B cell lymphomas. *J. Immunol.* 204: 23–36.
36. Oberlin, E., A. Amara, F. Bachelerie, C. Bessia, J. L. Virelizier, F. Arenzana-Seisdedos, O. Schwartz, J. M. Heard, I. Clark-Lewis, D. F. Legler, et al. 1996. The CXC chemokine SDF-1 is the ligand for LESTR/fusin and prevents infection by T-cell-line-adapted HIV-1. [Published erratum appears in 1996 *Nature* 382: 833–835.] *Nature* 382: 833–835.
37. Burns, J. M., B. C. Summers, Y. Wang, A. Melikian, R. Berahovich, Z. Miao, M. E. T. Penfold, M. J. Sunshine, D. R. Littman, C. J. Kuo, et al. 2006. A novel chemokine receptor for SDF-1 and I-TAC involved in cell survival, cell adhesion, and tumor development. *J. Exp. Med.* 203: 2201–2213.
38. Merad, M., P. Sathe, J. Helft, J. Miller, and A. Mortha. 2013. The dendritic cell lineage: ontogeny and function of dendritic cells and their subsets in the steady state and the inflamed setting. *Annu. Rev. Immunol.* 31: 563–604.
39. Turner, C. A., Jr., D. H. Mack, and M. M. Davis. 1994. Blimp-1, a novel zinc finger-containing protein that can drive the maturation of B lymphocytes into immunoglobulin-secreting cells. *Cell* 77: 297–306.
40. Ricker, E., M. Manni, D. Flores-Castro, D. Jenkins, S. Gupta, J. Rivera-Correa, W. Meng, A. M. Rosenfeld, T. Pannellini, M. Bachu, et al. 2021. Altered function and differentiation of age-associated B cells contribute to the female bias in lupus mice. *Nat. Commun.* 12: 4813.
41. Haberman, A. M., D. G. Gonzalez, P. Wong, T. T. Zhang, and S. M. Kerfoot. 2019. Germinal center B cell initiation, GC maturation, and the coevolution of its stromal cell niches. *Immunol. Rev.* 288: 10–27.
42. Rodig, S. J., A. Shahsafaei, B. Li, C. R. Mackay, and D. M. Dorfman. 2005. BAFF-R, the major B cell-activating factor receptor, is expressed on most mature B cells and B-cell lymphoproliferative disorders. *Hum. Pathol.* 36: 1113–1119.
43. Pelletier, M., J. S. Thompson, F. Qian, S. A. Bixler, D. Gong, T. Cachero, K. Gilbride, E. Day, M. Zafari, C. Benjamin, et al. 2003. Comparison of soluble decoy IgG fusion proteins of BAFF-R and BCMA as antagonists for BAFF. *J. Biol. Chem.* 278: 33127–33133.
44. Farr, A. G., M. L. Berry, A. Kim, A. J. Nelson, M. P. Welch, and A. Aruffo. 1992. Characterization and cloning of a novel glycoprotein expressed by stromal cells in T-dependent areas of peripheral lymphoid tissues. *J. Exp. Med.* 176: 1477–1482.
45. Donnou, S., C. Galand, V. Touitou, C. Sautès-Fridman, Z. Fabry, and S. Fisson. 2012. Murine models of B-cell lymphomas: promising tools for designing cancer therapies. *Adv. Hematol.* 2012: 701704.
46. Vlummens, P., K. De Veirman, E. Menu, E. De Bruyne, F. Offner, K. Vanderkerken, and K. Maes. 2019. The use of murine models for studying mechanistic insights of genomic instability in multiple myeloma. *Front. Genet.* 10: 740.
47. Kohnken, R., P. Porcu, and A. Mishra. 2017. Overview of the use of murine models in leukemia and lymphoma research. *Front. Oncol.* 7: 22.
48. Potter, M., and F. Wiener. 1992. Plasmacytomagenesis in mice: model of neoplastic development dependent upon chromosomal translocations. *Carcinogenesis* 13: 1681–1697.
49. Knittel, G., M. Metzner, G. Beck-Engeser, A. Kan, T. Ahrends, K. Eilat, K. Huppi, and M. Wabl. 2014. Insertional hypermutation in mineral oil-induced plasmacytomas. *Eur. J. Immunol.* 44: 2785–2801.
50. Rutsch, S., V. T. Neppalli, D. M. Shin, W. DuBois, H. C. Morse III, H. Goldschmidt, and S. Janz. 2010. IL-6 and MYC collaborate in plasma cell tumor formation in mice. *Blood* 115: 1746–1754.
51. Lightman, S. M., A. Utley, and K. P. Lee. 2019. Survival of long-lived plasma cells (LLPC): piecing together the puzzle. *Front. Immunol.* 10: 965.

52. Guja, K., T. Liehr, M. Rincic, N. Kosyakova, and S. S. Hussein Azawi. 2017. Molecular cytogenetic characterization identified the murine B-cell lymphoma cell line A-20 as a model for sporadic Burkitt's lymphoma. *J. Histochem. Cytochem.* 65: 669–677.

53. Muppidi, J. R., R. Schmitz, J. A. Green, W. Xiao, A. B. Larsen, S. E. Braun, J. An, Y. Xu, A. Rosenwald, G. Ott, et al. 2014. Loss of signalling via Gα13 in germinal centre B-cell-derived lymphoma. *Nature* 516: 254–258.

54. Lu, E., F. D. Wolfreys, J. R. Muppidi, Y. Xu, and J. G. Cyster. 2019. *S*-geranylgeranyl-L-glutathione is a ligand for human B cell-confinement receptor P2RY8. *Nature* 567: 244–248.

55. Apollonio, B., N. Ioannou, D. Papazoglou, and A. G. Ramsay. 2021. Understanding the immune-stroma microenvironment in B cell malignancies for effective immunotherapy. *Front. Oncol.* 11: 626818.

56. Balázs, M., F. Martin, T. Zhou, and J. Kearney. 2002. Blood dendritic cells interact with splenic marginal zone B cells to initiate T-independent immune responses. *Immunity* 17: 341–352.

57. Huang, H. Y., A. Rivas-Caicedo, F. Renevey, H. Cannelle, E. Peranzoni, L. Scarpellino, D. L. Hardie, A. Pommier, K. Schaeuble, S. Favre, et al. 2018. Identification of a new subset of lymph node stromal cells involved in regulating plasma cell homeostasis. *Proc. Natl. Acad. Sci. USA* 115: E6826–E6835.

58. Acton, S. E., A. J. Farrugia, J. L. Astarita, D. Mourão-Sá, R. P. Jenkins, E. Nye, S. Hooper, J. van Blijswijk, N. C. Rogers, K. J. Snelgrove, et al. 2014. Dendritic cells control fibroblastic reticular network tension and lymph node expansion. *Nature* 514: 498–502.

59. Piovesan, D., J. Tempany, A. Di Pietro, I. Baas, C. Yiannis, K. O'Donnell, Y. Chen, V. Peperzak, G. T. Belz, C. R. Mackay, et al. 2017. c-Myb regulates the T-bet-dependent differentiation program in B cells to coordinate antibody responses. *Cell Rep.* 19: 461–470.

60. Foxall, R., P. Narang, B. Glaysher, E. Hub, E. Teal, M. C. Coles, M. Ashton-Key, S. A. Beers, and M. S. Cragg. 2021. Developing a 3D B cell lymphoma culture system to model antibody therapy. *Front. Immunol.* 11: 605231.

61. Takemoto, A., M. Okitaka, S. Takagi, M. Takami, S. Sato, M. Nishio, S. Okumura, and N. Fujita. 2017. A critical role of platelet TGF-β release in podoplanin-mediated tumour invasion and metastasis. *Sci. Rep.* 7: 42186.

62. Dorfman, D. M., E. S. Hwang, A. Shahsafaei, and L. H. Glimcher. 2004. T-bet, a T-cell-associated transcription factor, is expressed in a subset of B-cell lymphoproliferative disorders. *Am. J. Clin. Pathol.* 122: 292–297.

63. Bende, R. J., F. van Maldegem, and C. J. M. van Noesel. 2009. Chronic inflammatory disease, lymphoid tissue neogenesis and extranodal marginal zone B-cell lymphomas. *Haematologica* 94: 1109–1123.